A novel high-throughput irradiator for in vitro radiation sensitivity bioassays

by

Tyler L. Fowler

A dissertation submitted in partial fulfillment of
the requirements for the degree of

Doctor of Philosophy
(Medical Physics)

At the
UNIVERSITY OF WISCONSIN - MADISON
2015

Date of final oral examination: 05/05/1015

The dissertation is approved by the following members of the Final Oral Committee:

Bryan P. Bednarz, Ph.D., Assistant Professor, Medical Physics
Randall J. Kimple, M.D., Ph.D., Assistant Professor, Human Oncology
Larry A. DeWerd, Ph.D, FAAPM, Professor, Medical Physics
Edward T. Bender, Ph.D., DABR, Assistant Professor, Medical Physics
Michael W. Kissick, Ph.D., Assistant Professor, Medical Physics

A novel high-throughput irradiator for in vitro radiation sensitivity bioassays

Tyler L. Fowler

Under the supervision of Assistant Professor Bryan P. Bednarz
and Assistant Professor Randall J. Kimple
at the UNIVERSITY OF WISCONSIN - MADISON

Given the emphasis on more personalized radiation therapy there is an ongoing and compelling need to develop high-throughput screening tools to further examine the biological effects of ionizing radiation on cells, tissues and organ systems in either the research or clinical setting. Conventional x-ray irradiators are designed to provide maximum versatility to radiobiology researchers, typically accommodating small animals, tissue or blood samples, and cellular applications. This added versatility often impedes the overall sensitivity and specificity of an experiment resulting in a trade-off between the number of absorbed doses (or dose rates) and biological endpoints that can be investigated *in vitro* in a reasonable amount of time. Therefore, modern irradiator designs are incompatible with current high-throughput bioassay technologies. Furthermore, important dosimetry and calibration characteristics (i.e. dose build-up region, beam attenuation, and beam scatter) of these irradiators are typically unknown to the end user, which can lead to significant deviation between delivered dose and intended dose to cells that adversely impact experimental results. Therefore, the overarching goal of this research is to design and develop a robust and fully automated high-throughput irradiator for in vitro radiation sensitivity investigations. Additionally, *in vitro* biological validation of this system was performed by assessing intracellular reactive oxygen species production, physical DNA double strand breaks, and activation of cellular DNA repair mechanisms. Finally, the high-throughput irradiator was

used to investigate autophagic flux, a cellular adaptive response, as a potential biomarker of radiation sensitivity.

To Lia, Quinn, and Maxwell,
for being by my side every step
of this long journey.

To my fallen brothers.

Abstract

Given the emphasis on more personalized radiation therapy there is an ongoing and compelling need to develop high-throughput screening tools to further examine the biological effects of ionizing radiation on cells, tissues and organ systems in either the research or clinical setting. Conventional x-ray irradiators are designed to provide maximum versatility to radiobiology researchers, typically accommodating small animals, tissue or blood samples, and cellular applications. This added versatility often impedes the overall sensitivity and specificity of an experiment resulting in a trade-off between the number of absorbed doses (or dose rates) and biological endpoints that can be investigated *in vitro* in a reasonable amount of time. Therefore, modern irradiator designs are incompatible with current high-throughput bioassay technologies. Furthermore, important dosimetry and calibration characteristics (i.e. dose build-up region, beam attenuation, and beam scatter) of these irradiators are typically unknown to the end user, which can lead to significant deviation between delivered dose and intended dose to cells that adversely impact experimental results. Therefore, the overarching goal of this research is to design and develop a robust and fully automated high-throughput irradiator for in vitro radiation sensitivity investigations. Additionally, *in vitro* biological validation of this system was performed by assessing intracellular reactive oxygen species production, physical DNA double strand breaks, and activation of cellular DNA repair mechanisms. Finally, the high-throughput irradiator was used to investigate autophagic flux, a cellular adaptive response, as a potential biomarker of radiation sensitivity.

Acknowledgments

I am so grateful to everybody that has helped me during my graduate studies. First and foremost I need to thank Bryan Bednarz for seeing potential in me and welcoming me into the lab, it was a big risk taking me on in a predominately Monte Carlo driven group. Bryan has always been supportive in letting me explore my own research interests, even if they were a bit out of our comfort zone. I'll never forget the day Bryan asked: "Hey, you were a medic, you know a bit of biology right?". That single question let down a path neither of us could have predicted. Luckily, we managed to be quite fruitful producing quality research along the way. I took great pride in skirting the boundaries of medical physics and cancer biology. During the course of this project I was also mentored by Randy Kimple. Randy takes great pride in mentoring growing scientists and I feel very fortunate to have worked with him. Randy also took a rather big risk letting a physicist, with no formal biology education, perform radiobiology research in his lab. We could not have picked a more difficult cellular process to study during the course of this research. Performing biology research has certainly taught me to shrug off failure and keep moving forward. I really can't wait to see what you gentlemen produce over the next decade.

I have been remarkably blessed to have such amazing lab mates as well. Abbey and Ming always managed to make me laugh no matter how bad my day had been, and feel thankful I wasn't programming. Kwang was definitely my "lab mother", even going so far as to bake me

birthday cakes every year, Kwang you are such a sweetheart. Adam, thank you for talking me back from the ledge more than once and all the help you have given me during your time in the lab. I have had an amazing group of undergraduates help me with my project through the years: Kai Ludwig, Andrew Shephard, Ali Bailey, and Mac Fisher. Thank you all so much for all of your assistance and hard work. I take mentoring and teaching very seriously and I hope during your time with me I have been able instill a few gems of wisdom.

The students and staff of the UW-MRRC have been tremendously helpful during my research and have all accepted me as one of their own. Specifically I would like to thank Larry DeWerd, John Micka, Ben Palmer, Cliff Hammer, Regina Fulkerson, Samantha Simiele, and Dwayne Riley. Larry, thank you for taking me under your wing and allowing our collaboration. John, your expert guidance was very helpful. Ben, had the patience to teach me precision fabrication and mechanical aspects I needed to consider. Cliff, thank you for all your help in performing my TLD experiments. Regina produced an amazing body of work that I was able to build upon. Samantha was instrumental in helping me through all of the hurdles I encountered with the x-ray source as well as fixing the source model as new information became available from the manufacturer. Dwayne and I served in combat together during the same period and was always there to support me during my time in graduate school when times became difficult, Dwayne you are a true friend.

I have had many individuals foster my growth in clinical care over the years. Ed Bender mentored me during all of my clinical experiences at UW. Ed is single handedly responsible for teaching me everything I know about the practical application of medical physics in patient care. Ed was amazingly patient, always willing to teach me, and trust me to do the job right. During my time in the military I have worked with some truly inspirational care providers. Maj. Zack Rinderer taught me compassion in patient care and fostered my growth in trauma management.

Lt. Col. Mark Foreman and Lt. Col Dan Hamre taught me to do the job with what I have and not with what I wanted and provided an endless source of laughs and comradery. Medicine has always been a large influence in my life, my great-grandfather Carol Elgin taught me to suture with forceps at age five, and my education continued with my grandmother Fay teaching me anatomy as a child.

I owe my devotion to science to my grandfather Jim. I distinctly remember many times during my childhood of him telling me his stories of performing crystallography research at Stanford, his face would always light up and his enthusiasm was infectious. He always would say, "research is just organized play, but with cool toys", I definitely would not be here today without him. He also taught me that anything worth doing is worth over-doing. My childhood was not ideal, but my mother always fostered my curiosity and wonder. She made great sacrifices to ensure I had a roof over my head, food on the table, and shoes on my feet. Words cannot express how much I owe you and how much I love you mom, you are a remarkable woman.

To my wife Lia; you truly are my "other-half", for I would not be whole without you, I love you baby. You absolutely did not know what you were getting into marrying me, I have definitely tested that "for better or worse" vow. Through everything you have always been my biggest supporter and my rock. I don't worry where the road of life takes us, for I know you will always be there by my side along the journey.

To my children Quinn and Max, I hope I can serve not only as your father but as your inspiration. I hope you can see that with hard work you can do whatever you set your mind to and be successful at it. I love you boys so much, you fill my heart with so much pride and love.

Lastly, to all the patients I have treated over the last 15 years I have been a medical care provider, I do it for you. To all the boys I couldn't bring back to their mothers from the sandbox, I will carry your memory always.

List of Figures

List of Tables

Contents

Chapter 1

Introduction

1.1 Overview

The study of the radiosensitivity of cells in culture has been an important component of radiobiology research for nearly a century [1]. Many investigators continue to utilize self-shielded radioactive sources such as ^{137}Cs that currently require background checks and security clearance to access in addition to significant overhead to maintain [2]. These irradiators often require careful placement of the sample within the housing to avoid inhomogeneous dosing and depending on the design can suffer from dose gradients due to shutter lag. Due to increasing concerns about the management and security of radioactive materials in research environments, there has been a gradual and likely permanent shift to machine-based x-ray irradiators [2]. Other factors such as lower cost, smaller physical footprint and easier maintenance add to the appeal of these systems.

Conventional x-ray irradiators used to investigate biological responses are built to provide maximum versatility to radiobiology researchers by accommodating small animals, tissue samples, and cellular applications. Modern cancer biology research often utilizes high-throughput assays performed in multi-well plates (e.g. 96- or 384-wells per plate) that can be rapidly

analyzed using high sensitivity endpoint assays. Current x-ray or radioactive source-based irradiators are incapable of varying the dose and/or dose-rate across the multiple wells in an individual microplate. This necessitates the comparison across multiple plates for investigators interested in either dose or dose/rate effects. Given the small volume of the wells in multi-well plates, small differences in the volume of media overlying adherent cells can also result in important differences in the dose received for "top-down" irradiators. The location of a plate within the radiation field can also influence dose homogeneity across the plate due to the "heel effect" leading to subtle biases in assay interpretation. Important dosimetry and calibration characteristics (i.e. dose build-up region, beam attenuation, and beam scatter) of these irradiators may be unknown to the end user. This gap in irradiator specificity and user knowledge can result in significant deviation between delivered dose and intended dose that ultimately adversely impacts experimental results and reproducibility.

Therefore, it is the aim of this research to 1) design, develop, and characterize a fully automated high-throughput micro-irradiator to aid in radiation sensitivity investigations, 2) validate the dosimetry of the irradiator system using known linear biological responses to ionizing radiation, and 3) use the irradiator system to investigate autophagy as an adaptive response to ionizing radiation in a head and neck cell line. In designing this irradiator the following critical design goals were identified: 1) high-throughput, 2) variable dose/dose-rate, 3) high radiation field uniformity, 4) full automation, 5) National Institute of Standards and Technology (NIST) traceable dosimetry. The production of this irradiator system leverages the increased productivity and capability offered by the newest generation of instrumentation used in the radiobiology laboratory. The proposed system provides an initial framework for the rapid analysis of *in vitro* cellular radiation sensitivity. Ultimately, better understanding of the biological

mechanisms that influence radiation sensitivities will pave the way towards delivering personalized medicine in the radiation oncology clinic.

While several novel irradiation devices have been developed in the last decade these mainly focus on producing thin micro-beams of several hundred microns in width and may require custom fabricated cellular growth plates that are incompatible with standard bioassay instrumentation [3,4]. Our system was designed from the beginning with the radiobiology researcher in mind to deliver highly uniform, full-well dose to standard cell culture plates. Furthermore, our system incorporates an on-board ionization chamber for full NIST traceable verification of dosimetry prior to an irradiation cycle capable of both delivering multiple doses and dose-rates within the same cell culture plate while traditional Cs-137 and cabinet x-ray irradiators are only capable of delivering single dose and dose-rates to an entire plate [5].

1.2 Description of upcoming chapters

The upcoming chapters present the necessary background information followed by specific discussions of the development, characterization, and application of the irradiator system.

Chapter 2 will provide background information about conventional irradiators, and will highlight their strengths and weaknesses. The characteristics of the Xoft Axxent electronic brachytherapy micro-source that is utilized in our system will be discussed. Background information about relevant and well-known radiation response mechanisms that were used to biologically validate the irradiator system will be presented. Finally, the cellular process of autophagy will be discussed including general information about the process and its importance to both carcinogenesis and cancer treatment response.

Chapter 3 will discuss the conception, development, and characterization of the irradiator system. The design process and fabrication of the system will be explored. Monte Carlo methods for dosimetry will be discussed. Additionally, characteristics and methods for film and thermoluminescent dosimeter use in this project will be examined along with dosimetric uncertainties.

Chapter 4 presents the biological validation of this system *in vitro*. Three cellular events that are induced by exposure to ionizing radiation will be examined to show mechanical and environmental stress during the irradiation cycle does not introduce significant perturbation to cellular signaling pathways.

Chapter 5 will present the application of this irradiator system in radiobiological research. The temporal dynamics of autophagy induced by ionizing radiation will be examined along with how both total delivered dose and dose-rate during irradiation can modulate this cellular response.

Chapter 6 will present a final summary of the goals and achievements of this investigation. Finally, future work to be continued for this project will be discussed.

Chapter 2

Background

Conventional x-ray irradiators used to investigate biological responses are built to provide maximum versatility to radiobiology researchers by accommodating small animals, tissue samples, and cellular applications. However, the versatility of these irradiator systems coupled with the lack of understanding dosimetric principles by the end-user often leads to large uncertainties in the dose delivered to study the biological response to ionizing radiation. Historically this dosimetric uncertainty was overlooked because the radiobiological responses studied were great enough in magnitude to produce satisfactory results. However, as bioassay instrumentation has evolved, and as the biological responses being studied are more subtle, the dosimetric uncertainty in these investigations has begun to perturb experimental results, often without the researcher's knowledge. In this chapter the strengths and weaknesses of current irradiator technology will be discussed along with the characteristics of the source used in this work. The relevant radiobiology in early ionizing radiation cellular exposure used to assess the irradiator system will be introduced. Finally, the subtle cellular adaptive response of autophagy will be discussed in the framework of head and neck cancer as an application of the irradiator system to a translational cancer radiobiology research topic.

2.1 Conventional irradiator technology

2.1.1 Radionuclide irradiators

To date, the most common type of irradiator used in radiation biology research has been self-shielded radioactive sources and in particular ^{137}Cs [2]. These irradiators often feature a moveable pneumatic column where cell culture plates or animal vessels are positioned. When the irradiator is activated, the column lowers into a heavily shielded compartment to be exposed to radionuclide source rods before a timer system returns the column for sample retrieval (**Figures 2.1-2**). These irradiators may also feature adjustable collimation/apertures and/or scattering plates and turntables to increase the homogeneity of the dose distribution. Due to the discrete size of the sources, achieving dose homogeneity can be difficult and these devices require extensive evaluation prior to use [6,7]. Additionally, owing to a common design of these irradiators, a dose gradient is introduced from the moving column, and for stacked cell culture dishes the bottom cell culture dish will be the first to enter and last to exit the vessel resulting in higher doses than the top cell culture plate.

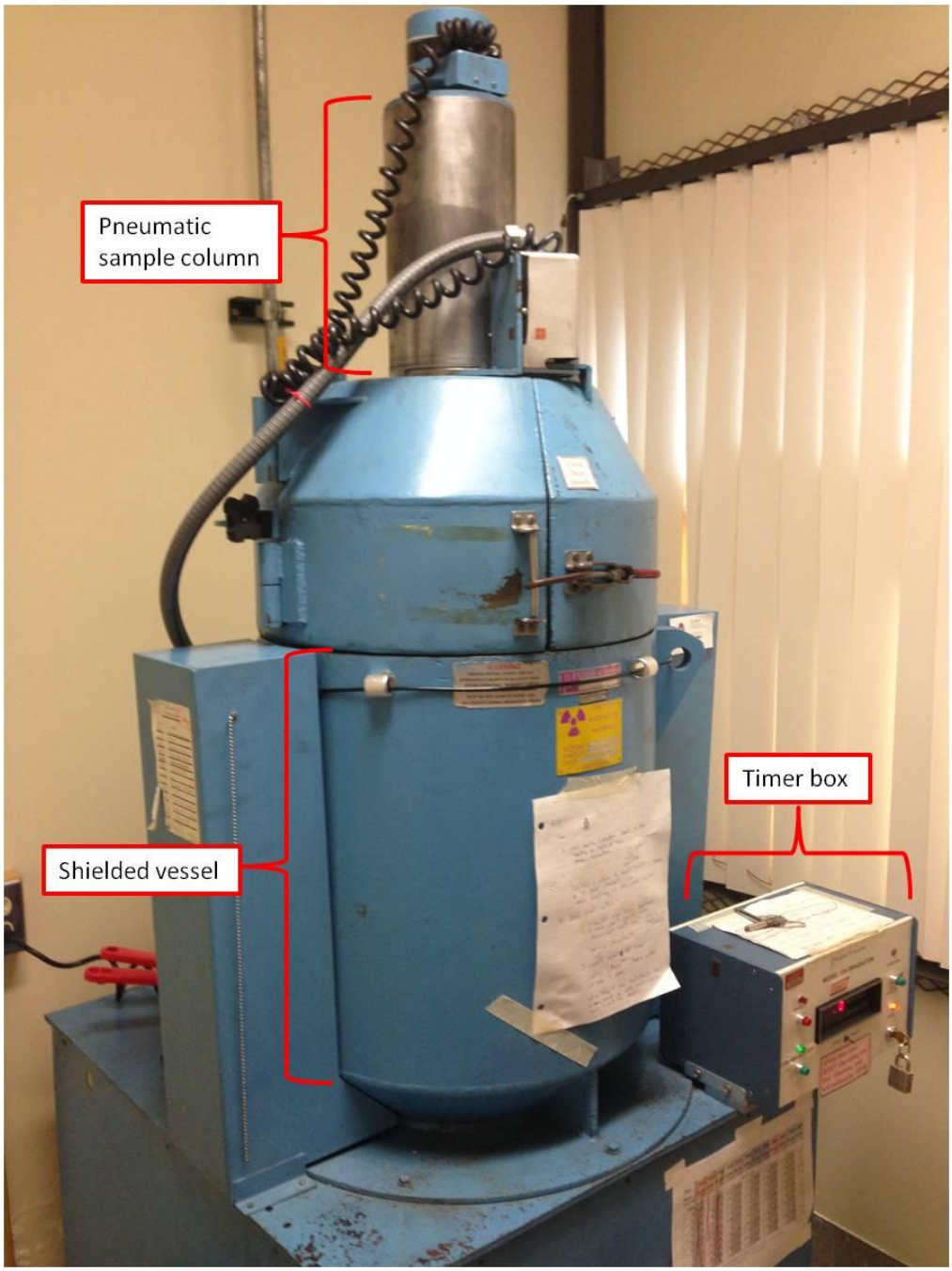

Figure 2.1: JL Shepherd Cs-137 irradiator.

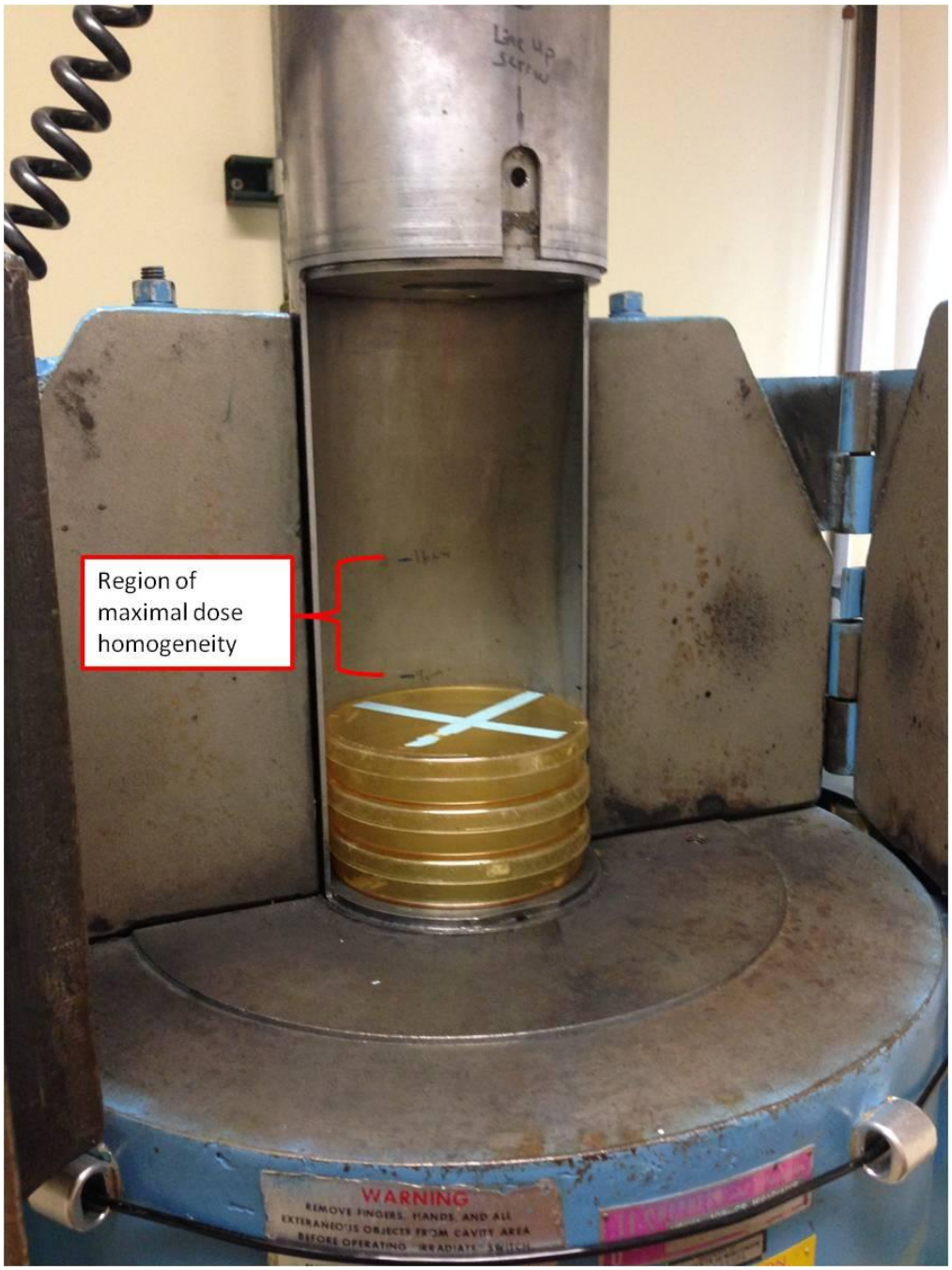

Figure 2.2: Cs-137 pneumatic sample column.

In addition to experimental uncertainties associated with radionuclide irradiators, there is an increasing concern about the management and security of radioactive materials in research environments, which has led to a gradual and likely permanent shift to machine-based x-ray irradiators [2]. The issue has been appropriately summarized in the 2010 US Interagency Task Force on Radiation Source Protection and Security report to the President and Congress that:

"Although alternative forms and radionuclides were assessed [for irradiators], further risk reduction might be achieved through alternative technology research and development that focuses on non-radioactive replacement (e.g., x-ray). X-ray technologies were found to be cost competitive with radionuclide technologies on an annualized cost basis. Recent developments in x-ray technology may lead to mature and desirable alternatives in the near future. A gradual stepwise phase-out could be feasible as alternatives become technologically and economically viable" [8].

2.1.2 X-ray cabinet irradiators

Due to factors such as greatly reduced governmental and security regulation, lower lifetime costs, smaller physical footprint and easier maintenance the appeal of cabinet x-ray irradiators has significantly increased. These irradiator systems feature a x-ray tube positioned above a moveable table within a shielded cabinet, as seen in **Figure 2.3**, with beam spectrums between 160-450 kVp [9]. However, conventional x-ray irradiators used to investigate biological responses are built to provide maximum versatility to radiobiology researchers, but current designs are only capable of providing single dose and/or dose rate irradiations for individual cell culture plates. Additionally, the dose could potentially vary between different wells in the cell culture plate depending on a variety of different factors including location on the plate within the radiation field and volume of media overlying the cells. These constraints are exemplified in

Figure 2.4 where radiochromic film measurements revealed a 20% absorbed dose variation across multiple wells when a 96-well cell culture plate was uniformly irradiated with an X-RAD 320 (Precision x-ray, North Branford, CT) conventional cabinet irradiator, additionally this dose inhomogeneity was witnessed in the DNA double strand break cellular repair response to ionizing radiation. This large variation in delivered dose is primarily due to the anode heel effect, where photons are differentially self-attenuated by the anode resulting in up to 45% variation in photon fluence across a radiation field as seen in **Figure 2.5** [10]. Conventional x-ray irradiators are also more susceptible to output fluctuation impeding the ability to deliver consistent doses/dose-rates over multiple days and conditions.

In addition to standard x-ray cabinet irradiators, several novel micro-beam x-ray irradiation devices have been developed in the last decade. These irradiators produce thin beams that are several hundred microns in width and aim to target single cells or a small population of cells within a cell culture plate. However, these irradiators require custom fabricated cellular growth plates that are incompatible with standard bioassay instrumentation [3,4]. Therefore, there is an unmet need for an irradiator that can deliver small fields to cell culture plates, yet is compatible with of standard bioassay equipment and instrumentation.

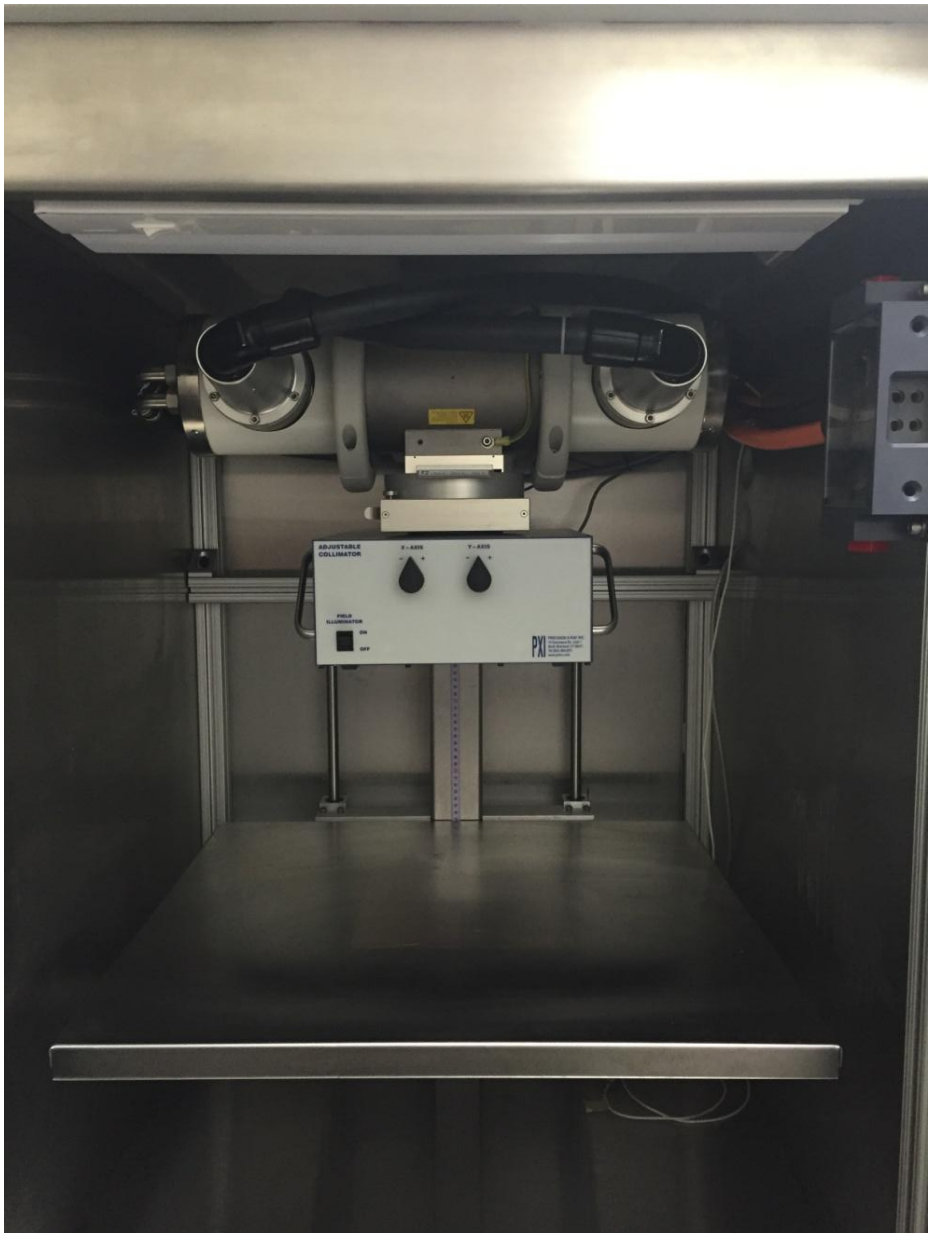

Figure 2.3: Interior of x-ray cabinet irradiator.

(a)

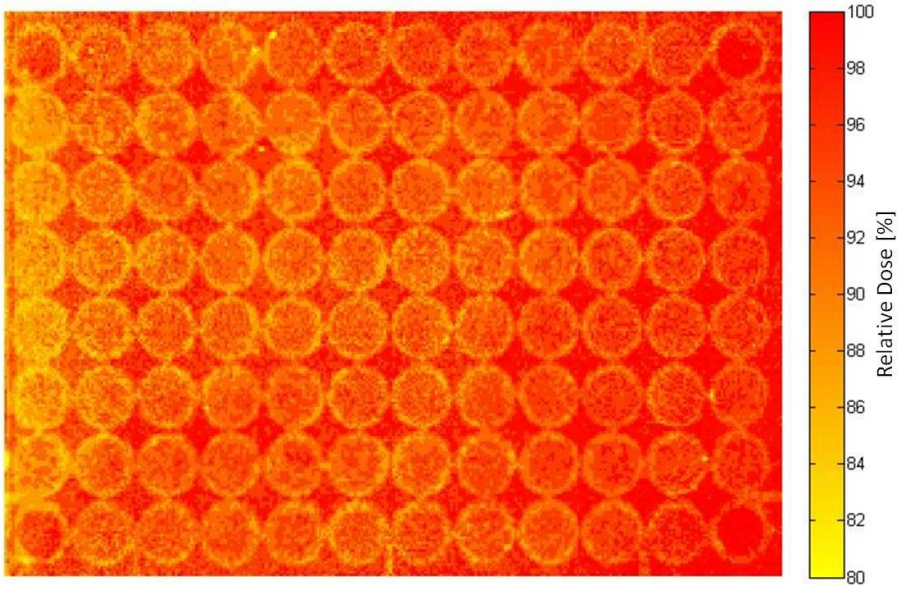

(b)

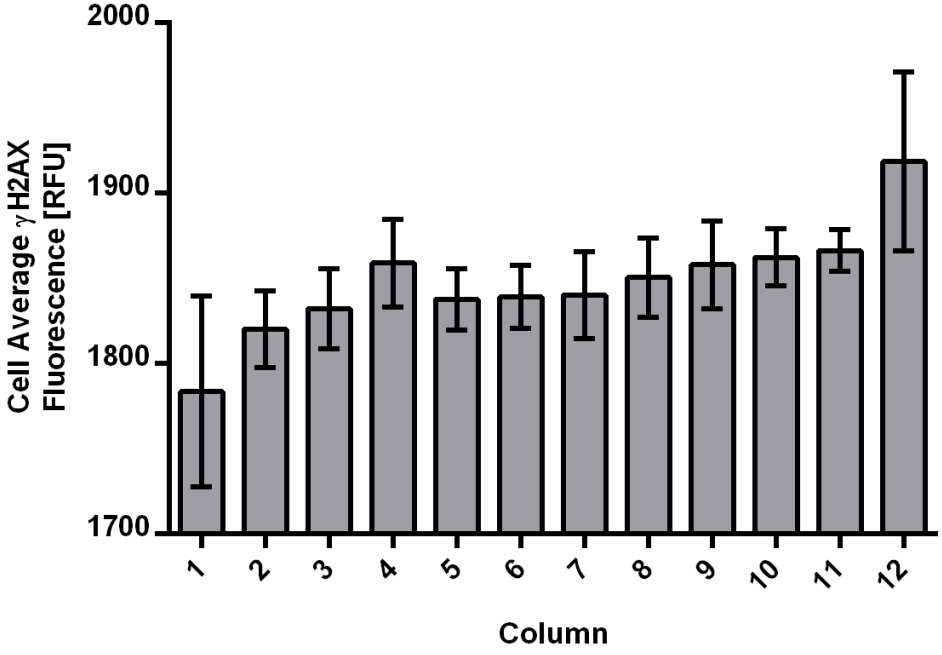

Figure 2.4: a) Relative absorbed dose colorwash measured using GafChromic EBT3 (International Specialty Products, Wayne, NJ) film for a 96-well plate irradiated in a cabinet irradiator indicating unacceptable dose inhomogeneity, wells were filled with cell culture media to provide proper backscatter to film plane. Note that the corner wells were not filled with cell culture media, and are labeled with an asterisk (*) [5], b) cell average γH2AX after a 4 Gy dose is delivered to cell culture plate showing x-ray heel effect significantly impacting cellular biological function.

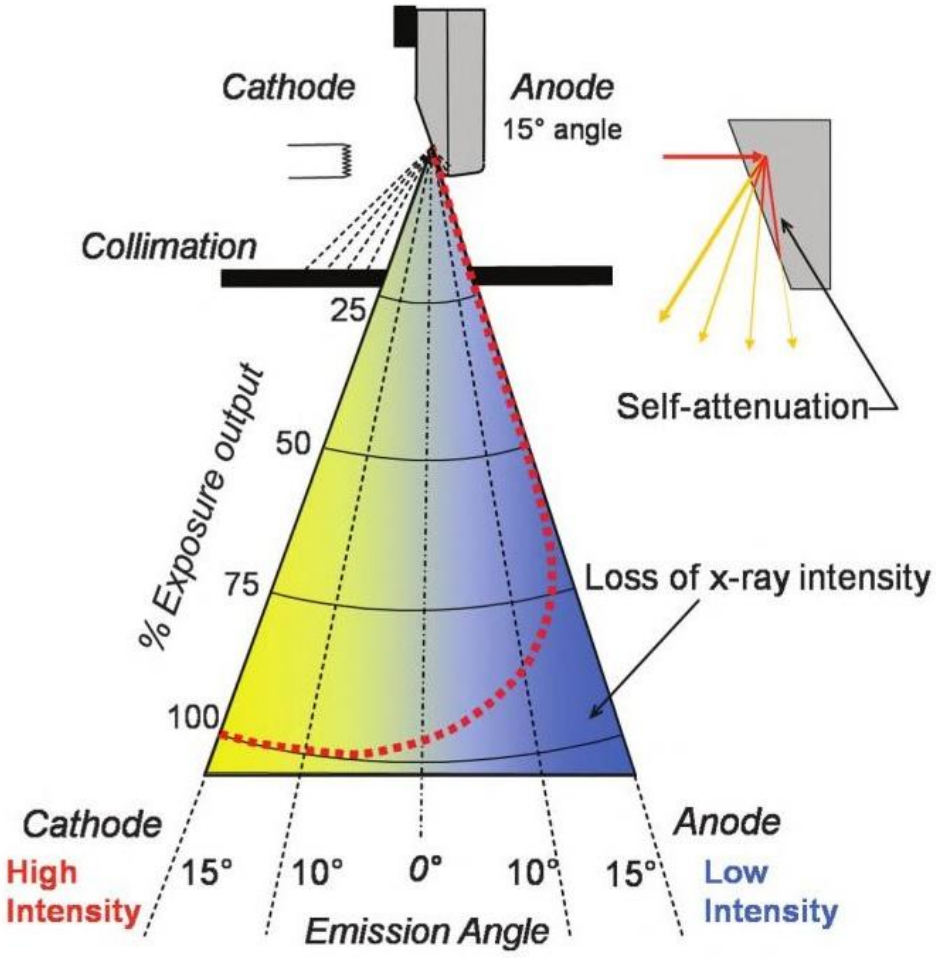

Figure 2.5: Anode heel effect in x-ray cabinet irradiator [11].

2.2 Miniature x-ray sources

Recently miniature x-ray sources have been developed as an alternative to radionuclide based (^{192}Ir & ^{103}Pd) high dose-rate (HDR) brachytherapy. These systems have the advantage of providing local radiation treatment without the need for increased security mandated by federal regulations. Additionally, these x-ray sources operate below 50 kVp limiting the penetration of dose to organs at risk (OAR) thereby reducing normal tissue toxicity. Currently two of these sources are commercially available for use, the INTRABEAM™ system developed by Photoelectron Corp. and the Axxent eBx® system developed by Xoft Inc. (a subsidiary of iCad Inc.) [12]. In this work the Axxent eBx® system was utilized as the source for our novel high-throughput irradiator.

The Axxent eBx® electronic brachytherapy source (Xoft Inc., San Jose, CA) is a disposable miniature x-ray source (**Figure 2.6**) that FDA approved for post-lumpectomy breast treatments in December 2005. The source is housed in the distal end of a water cooling catheter that may be inserted into site specific applicators and features a minimally filtered 50 kVp bremsstrahlung spectrum with a maximum operating current of 300 μA [12]. A series of four stainless steel surface applicators (10, 20, 35, and 50 mm in diameter, **Figure 2.7**) are available that feature an aluminum flattening filter to deliver a uniform dose distribution at the polycarbonate exit window. A dosimetry formalism was developed in 2014 by Fulkerson et al. for this series of surface applicators using an end-window ionization chamber with future recommendations to come from the American Association of Physicists in Medicine (AAPM) Task Group No. 253 on surface brachytherapy [13].

(a)

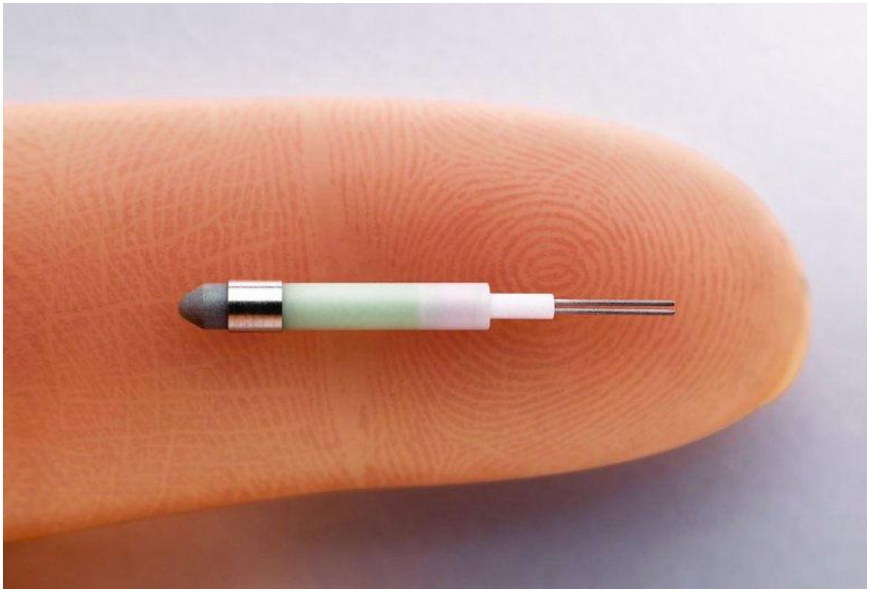

(b)

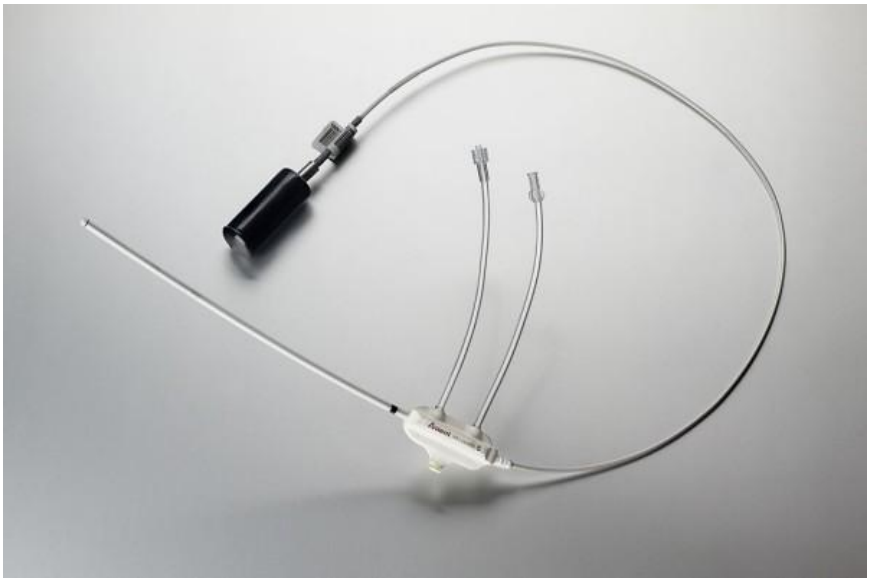

Figure 2.6: (a) Xoft Axxent eBx® bare source and (b) source inside cooling catheter. Images courtesy of Xoft Inc. (a subsidiary of iCad Inc.).

Figure 2.7: Stainless steel surface applicators manufactured for the Axxent eBx system by Xoft Inc. (a subsidiary of iCad Inc.).

2.3 Cascade of cellular events to ionizing radiation

Radiation therapy is an effective modality for the treatment of many different cancers. More than half of all cancer patients will receive radiation therapy during the course of their treatment [14]. Despite its longstanding and widespread use, radiation therapy lacks a high degree of personalization for the management of cancers in individual patients. Historically, improvements in treatment outcomes from radiation therapy have resulted from optimization of physical and technical aspects of the modality including precise dose delivery, optimization of treatment plans and robust quality assurance metrics. However, it is generally accepted that improved outcomes could be achieved by identifying the sizable variation of radiation sensitivities among individual patients or patient sub-populations in a given patient cohort. When exposed to ionizing radiation cells exhibit many functional and phenotypic changes. Generally these effects increase in frequency as the absorbed dose to the cells increases, yet the rate of change of the dose-effect relationship depends on a variety of radiation biology parameters and can vary among patients. If mechanistic pathways responsible for the variation of radiation sensitivity of either cancer cells or healthy cells are identified then it may be possible to use predictive biomarkers to identify which patients are likely to benefit or not benefit from the treatment. This information could enhance the treatment process and improve the overall treatment outcome.

The general goal of radiation therapy is to permanently control a primary tumor and lymph node metastasis without producing toxicity in normal tissue. To achieve this goal high absorbed doses need to be delivered to the target volume in order to induce cell death in cancerous cells while limiting the absorbed dose to healthy organs at risk to prevent cell death in healthy cells. As a result the most common dose-effect relationship studied in radiation biology is the cell survival curve. The colony formation assay is used to construct this curve with the end-

point being the surviving fraction of cells at a certain absorbed dose as seen in the linear-quadratic model shown in **Figure 2.8**. The linear-quadratic model makes the assumption that two distinct components act in cell killing, one of these is proportional to the dose while the other is proportional to the square of the dose:

$$S = e^{-\alpha D - \beta D^2} \quad (2.1)$$

where S is the fraction of cells surviving an absorbed dose D, and α and β are constants [1]. The overall shape of dose-effect relationships (i.e. slope) can be changed by cellular repair, repopulation, and recovery. Cellular repair following irradiation acts to bypass, compensate, and/or cause specific biochemical reversal of induced damage and restore functional integrity. Repopulation is simply the proliferation of cells to replace damaged cells. Finally, recovery is the change in response of a cell after irradiation that tends to restore functional integrity [15]. Another important factor that impacts cell survival is reoxygenation, which is a phenomenon where hypoxic tumor cells gain access to oxygen and become more radiosensitive as a result of coming in closer proximity to capillaries. An overwhelming body of evidence has shown that radiation induced cell lethality is primarily from chromosomal deoxyribonucleic acid (DNA) damage, which triggers cell death directly though mitotic catastrophe through cellular catabolism by apoptosis, autophagy, or necrosis (i.e. Type I, Type II, or Type III cell death) [16].

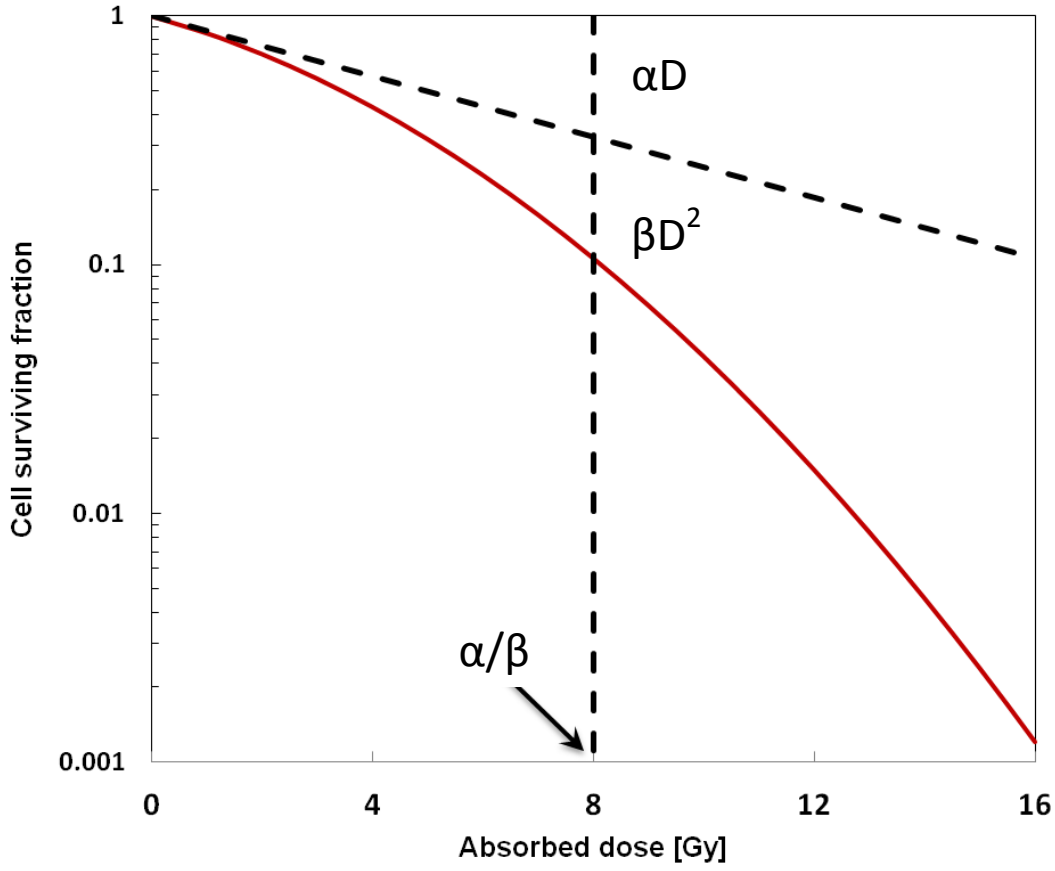

Figure 2.8: Cell survival curve as a function of absorbed dose [1].

The damage delivered to the DNA of a cell and subsequent repair or death follows a predicable cascade of events following exposure to ionizing radiation. Human tissue is comprised of approximately 80% water. When a high-energy photon interacts with one of these water molecules it liberates an electron and produces free ion radicals. These ion radicals quickly react with nearby water molecules to form reactive oxygen species (ROS), and most commonly a highly reactive hydroxyl radical, as shown below [1]:

$$H_2O \rightarrow H_2O^+ + e^- \tag{2.2}$$

$$H_2O^+ + H_2O \rightarrow H_3O^+ + OH\cdot \tag{2.3}$$

This indirect action from ionizing radiation through intermediary hydroxyl radicals are responsible for an estimated 60-90% of DNA damage and cell lethality from low linear energy transfer (LET) ionizing radiation, such as x-rays or γ-rays, the remaining damage is caused by direct action of photons interacting directly with DNA [17-19].

ROS may diffuse about 4 nm from the sight of the interaction where it can come in contact with the phosphate groups forming the DNA "backbone" causing a DNA strand break. Single strand breaks (SSB) are quickly repaired by the cell using the opposite strand as a "blueprint", however double strand breaks (DSB) completely sever the DNA and require complex repair mechanisms [20]. DSBs scale linearly with ionizing radiation dose, with an incidence of approximately 20-40 DSBs per Gy of absorbed dose per nucleus from x-rays [21,22]. If DNA DSBs are not adequately repaired the result may be cell death, mutation, or carcinogenesis. The creation of a DSB promptly initiates the phosphorylation (molecular biological "on switch" that activates proteins) of histone H2AX at Serine 139 (γH2AX) as a first responder in the cellular DNA DSB repair pathway, while the resolution of DSBs correlates with dephosphorylation of γH2AX [22-24]. Repair of the DNA DSB is performed through either homologous recombination

repair (HRR) or nonhomologous end-joining (NHEJ) pathways. This multi-step process is illustrated in **Figure 2.9**.

2.4 Autophagy

Meaning "self eating", autophagy is a genetically programmed, evolutionarily conserved process whereby cellular proteins, organelles, and cytoplasm are engulfed, digested, and recycled in response to cellular stress to aid in cell survival [25]. However, autophagy can also promote cell death through excessive self-digestion and degradation of cellular contents [26]. Although autophagy was discovered more than four decades ago, this process remains elusive and has only become intensely studied in the past 15 years.

The current belief is that autophagy acts as a pro-survival mechanism in normal functioning cells that can aid the cell in fighting carcinogenesis. However, in cells with defective apoptosis, commonly called programmed cell death, necrotic tissue begins to accumulate leading to local chronic inflammation and eventually carcinogenesis [27]. Once transformed these cancer cells begin to hijack the autophagic process, like many other normal cellular functions. Autophagy acts to protect cancer cells from metabolic stress within the tumor microenvironment under conditions of hypoxia and deficient nutrient supply [25]. Additionally, autophagy deficient cancer cells begin to accumulate p62, protein aggregates, damaged mitochondria, and ROS that contribute to further oncogenesis [28,29]. Suppression of autophagy in tumors has shown to enhance the cytotoxicity of chemotherapeutic agents and reduce tumor mass. Autophagy is a highly dynamic multi-step process. The initiation of autophagy begins with the formation of the phagophore, a double walled lipid membrane that sequesters and engulfs cargo to be degraded.

The phagophore expands and closes to form the autophagosome. The completion of the autophagosome is followed by the docking and fusion with a lysosome to form the autolysosome.

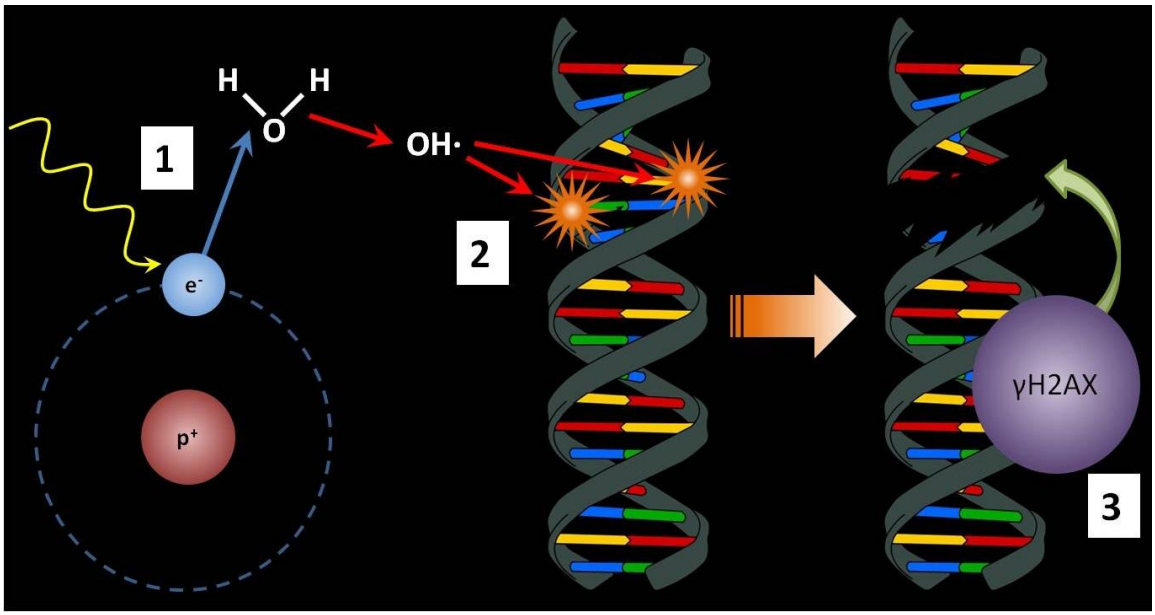

Figure 2.9: Cascade of cellular events induced by ionizing radiation. Step 1 - production of ROS by high energy photons, step 2 - induction of DNA DSB, and step 3 - activation of repair pathway promoter γH2AX.

The lysosome begins to pump lysosomal hydrolase, an enzyme that breaks down biomolecules, into the vacuole to degrade the cargo into its constituent amino acids to be recycled by the cell [30]. Due to the complexity of the dynamics of this process it is insufficient to examine autophagy at a single time-point, rather the total flux of the process must be examined for proper interpretation of the autophagic process. In order to assess the autophagic flux an inhibitor may be used to prevent turnover of the autophagosomes and measure their time-dependant accumulation.

Many of the genes involved in the regulation of autophagy, often called autophagy-related genes (ATG), are not entirely specific to just autophagy and are involved in other signaling pathways as well. However, one ATG protein, ATG8 (commonly called LC3B, microtubule-associated protein 1 light chain 3), is used exclusively in the formation of the phagophore and autophagosome. LC3B has two isoforms within the cell, LC3B-I and LC3B-II. When autophagy is induced LC3B-I, found in the cytoplasm of the cell, is lipidated by phosphatidylethanolamine (PE) to become LC3B-II. Because of the exclusivity of this protein in the formation of the autophagic bodies it is the most common target for assessing autophagic flux [30]. **Figure 2.10** illustrates the mechanics of the autophagy-lysosomal pathway

Several groups have shown that autophagic acidic compartments are formed in response to damage initiated by ionizing radiation in a variety of cancer cell types ranging from breast, pharyngeal, cervical, lung, to brain cancers [31-35]. Muñoz-Gámez, et al. and Huang et al. have shown that cells deficient in producing the enzyme poly [ADP-ribose] polymerase 1 (PARP-1), involved in homologous recombination DNA DSB repair, were unable to induce autophagy when exposed to doxorubicin and ROS that induces autophagy through DNA damage [36,37]. However, the exact mechanism by which ionizing radiation induces autophagy remains unclear.

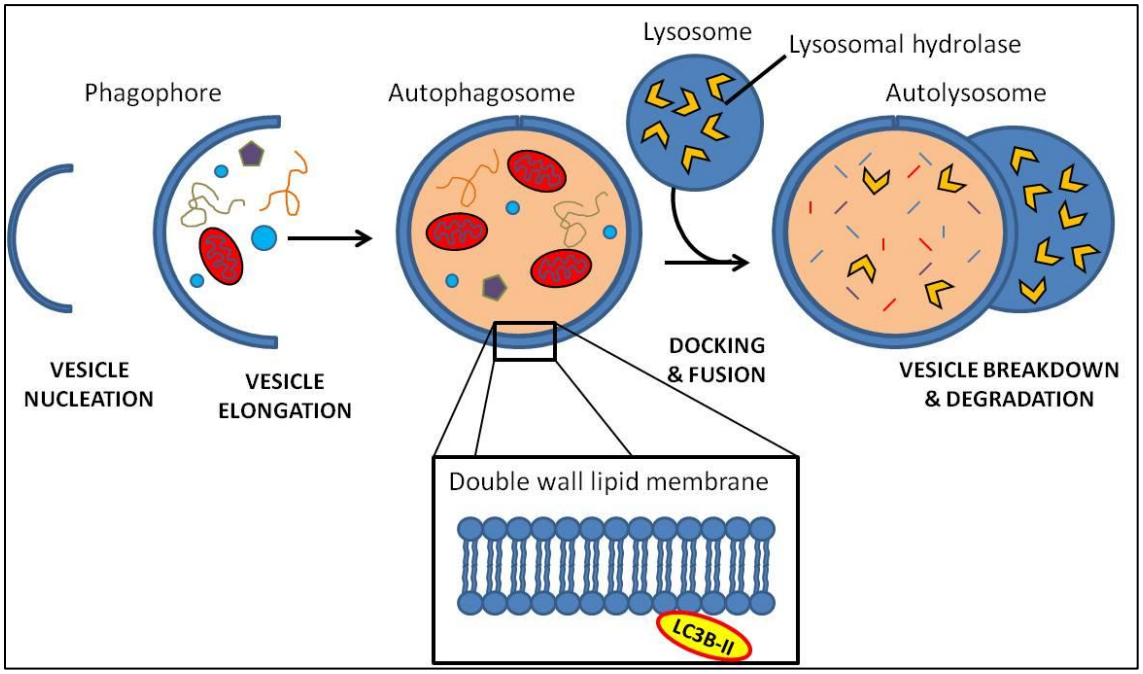

Figure 2.10: Autophagic process showing degradation of long lived and damaged organelles.

2.5 Human papillomavirus in head & neck cancer

Head and neck cancer (HNC) is the sixth most common cancer worldwide, with about 620,000 new diagnoses annually [38]. The traditional view of HNC as solely a tobacco/alcohol-associated disease has been dichotomized by the recognition that Human Papillomavirus (HPV) causes HNC in a growing subset of patients, many of whom have no traditional risk factors [39,40]. HPV-positive cancers are now thought to account for 30-65% of all HNC and 50-80% of cancers arising in the oropharynx [40,41]. HPV positive (HPV+) HNC represents a growing public health concern, and is likely to become the predominant cause of HNC over the coming decade [42].

Human papillomavirus is a double stranded, non-enveloped, circular DNA virus with over 1000 subtypes. Approximately 20 strains pose a high risk of cancer formation in the cervix, vagina, vulva, uterus, penis, and head and neck [43]. Strains HPV-16 and HPV-18 pose the greatest risk of carcinogenesis [43]. In the oropharynx, HPV-16 accounts for over 90% of all HPV-associated cancers [39,44]. A total of eight viral proteins are encoded by the virus with three being identified as oncogenes: E5, E6, and E7 (**Figure 2.11**) [45-47]. However, E5 does not play a large role in carcinogenesis [48]. The most important role of these oncogenes is E6 degrades p53 while E7 degrades Rb, both critically important cellular cancer suppressor proteins.

Improved outcomes in patients with HPV+, compared with HPV-negative (HPV-), HNC have been consistently reported [49-57]. Several prospective trials and retrospective reviews utilizing radiation alone have reported outcomes based on HPV status. Each of these studies support the hypothesis that patients with HPV-positive HNC have significantly better overall survival and local/regional control than those with HPV-negative disease [58]. Across multiple clinical trials patients with HPV-positive disease have a 60-80% overall reduction in mortality.

Consistent with these findings, retrospective analysis of the Radiation Therapy Oncology Group (RTOG) 0129 trial, the 3 year progression free survival for HPV-positive patients was better than those who were HPV-negative (74% vs. 43%, **Figure 2.12**) [41]. Similarly, in the TAX 324 study, the proportion of HPV-positive patients free of progression was improved compared to HPV-negative patients (73% vs. 29%) [57].

Although the biologic basis for this improvement remains unclear, it has been postulated that the improved outcomes are due to increased radiation sensitivity [53], which is a finding that has been recently confirmed using both existing cell lines and patient derived xenografts [59]. Given the predilection of these patients to present with locally advanced disease, radiation therapy plays a critical role in the multidisciplinary management of modern HNC patients. A clear understanding of the biological mechanisms responsible for this sensitivity could help improve clinical outcomes in these patients.

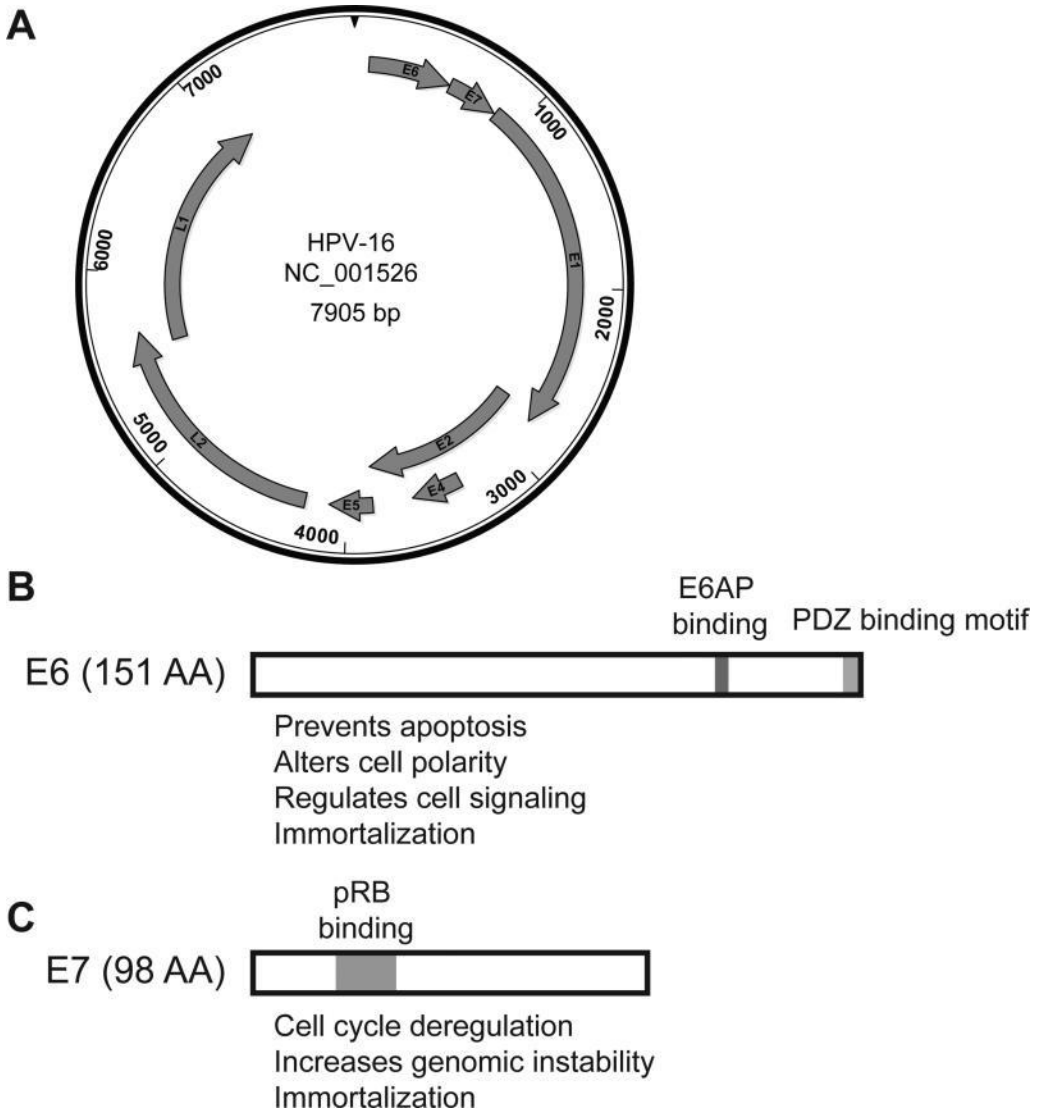

Figure 2.11: The HPV genome is a double-stranded circular DNA containing approximately 8000 base pairs and encoding eight proteins (A). E6 (B) and E7 (C) are the predominant HPV oncogenes and target a variety of diverse cellular processes [58].

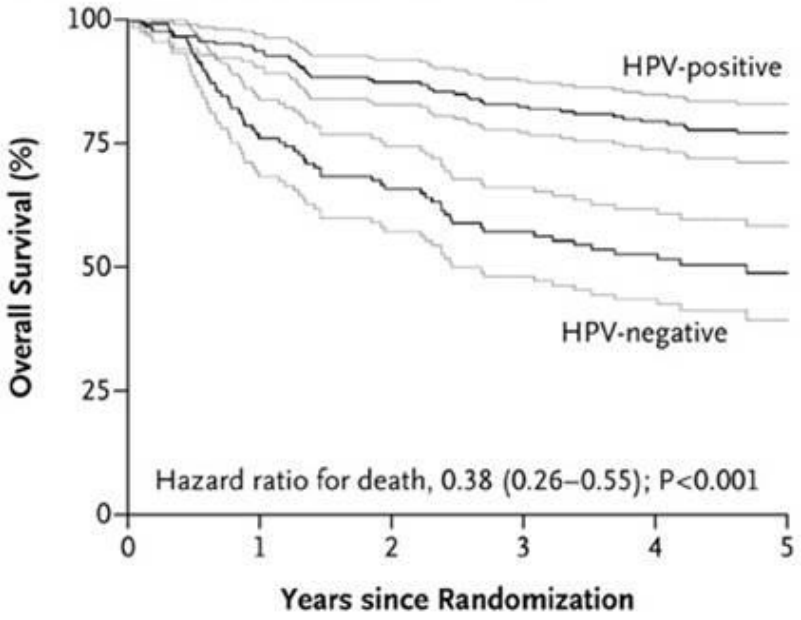

Figure 2.12: Five year overall survival of patients with oropharyngeal cancer stratified by HPV status [41].

Chapter 3

Irradiator System Development

The loss of dosimetric resolution in dose-response experiments is detrimental because new radiation therapy technology and treatment methods generate non-uniform dose distributions that vary widely from patient to patient. Furthermore, important dosimetry and calibration characteristics (i.e. dose build-up region, beam attenuation, and beam scatter) of these irradiators are typically unknown to the end user. This gap in irradiator specificity and user knowledge can result in significant deviation between delivered dose and intended dose that ultimately adversely impacts experimental results.

Therefore, it is the aim of this research to design and develop a fully automated high-throughput micro-irradiator to aid in radiation sensitivity investigations. In designing this irradiator the following critical design goals were identified: 1) high-throughput, 2) variable dose/dose-rate, 3) high radiation field uniformity, 4) full automation, 5) National Institute of Standards and Technology (NIST) traceable dosimetry.

3.1 Irradiator design

To achieve precise automation, the 96-well cell culture plate is translated via a 3-axis, motor-driven translation stage above the fixed x-ray source. A critical design element of this irradiator system is the use of an inverted geometry, the source is positioned below the plate and irradiates the cells through the bottom of the cell culture plate. This inverted geometry was used to minimize dosimetric uncertainty, when radiation biologists use these plates no standardized volume of media is used. By irradiating from the bottom the radiological path-length between the source and cellular plane is consistent by passing through the 1.27 mm polystyrene well bottom, which is the industry standardized thickness of cell culture plate. The source is also fixed to minimize disruption of the coolant and high-voltage supply lines.

The translation stage is positioned 0.2 mm above the surface applicator to ensure smooth translation of the stage without collisions with the source and provides a framework to support the cell culture plate without interfering with the x-ray beam. Given the complexity of the translation stage, it was originally designed using the CAD software SolidWorks® (Dassault Systemes SolidWorks Corp., Waltham, MA) and then fabricated using a 3D acrylic printer.

The translation stage is operated using precision Velmex™ motors (Bloomfield, NY) located on each independent axis. The motors are controlled by LabVIEW (National Instruments Corp., Austin, TX), a program which permits automated control of the stage position and irradiation dwell time. The source to cellular plane distance is maintained within 0.038 mm, as measured with a precision dial indicator, during translation across the plate.

The irradiator translation stage also includes an Exradin A20 (Standard Imaging, Madison, WI) end-window ionization chamber to provide periodic NIST traceable air-kerma rate

verification. A digital video camera is mounted underneath the translation stage to allow real-time visual tracking of the irradiation process. The full irradiator system in shown in **Figure 3.1-2**, while the user interface controlled outside of the x-ray vault is shown in **Figure 3.3**.

3.2 Source characterization

To take advantage of emerging high-throughput robotic bioassay equipment, a system was developed that would accommodate assays performed in a 96-well cell culture plate, shown in **Figure 3.4**. The 96-well cell culture plates feature 96 wells with an area of 0.32 cm^2 and an average yield of $3.2x10^4$ cells that are ideal for bioassay experiments where large amounts of data are to be collected or multiple variables manipulated. A mock-up of the proposed design is illustrated in **Figure 3.5**. In this system, a fixed miniature x-ray source with adequate collimation irradiates single-wells of a cell culture plate. It was decided that the Xoft Axxent eBx® electronic brachytherapy system (iCAD, Inc, Nashua, NH) with clinical surface applicators best matched our source criteria because it features a 50 kVp spectrum, as provided in Rivard et al. [12], that is easily collimated and reduces well-to-well scatter. Using the Manufacturing Test Fixture (MTF) controller, the x ray tube current can be adjusted up to 300 μA allowing dose-rate modulation without effecting beam spectrum. The surface applicators developed for this system feature a beam profile flattening filter for each of four size applicators: 10, 20, 35, and 50 mm. During this project the 10 and 20 mm surface applicators were used.

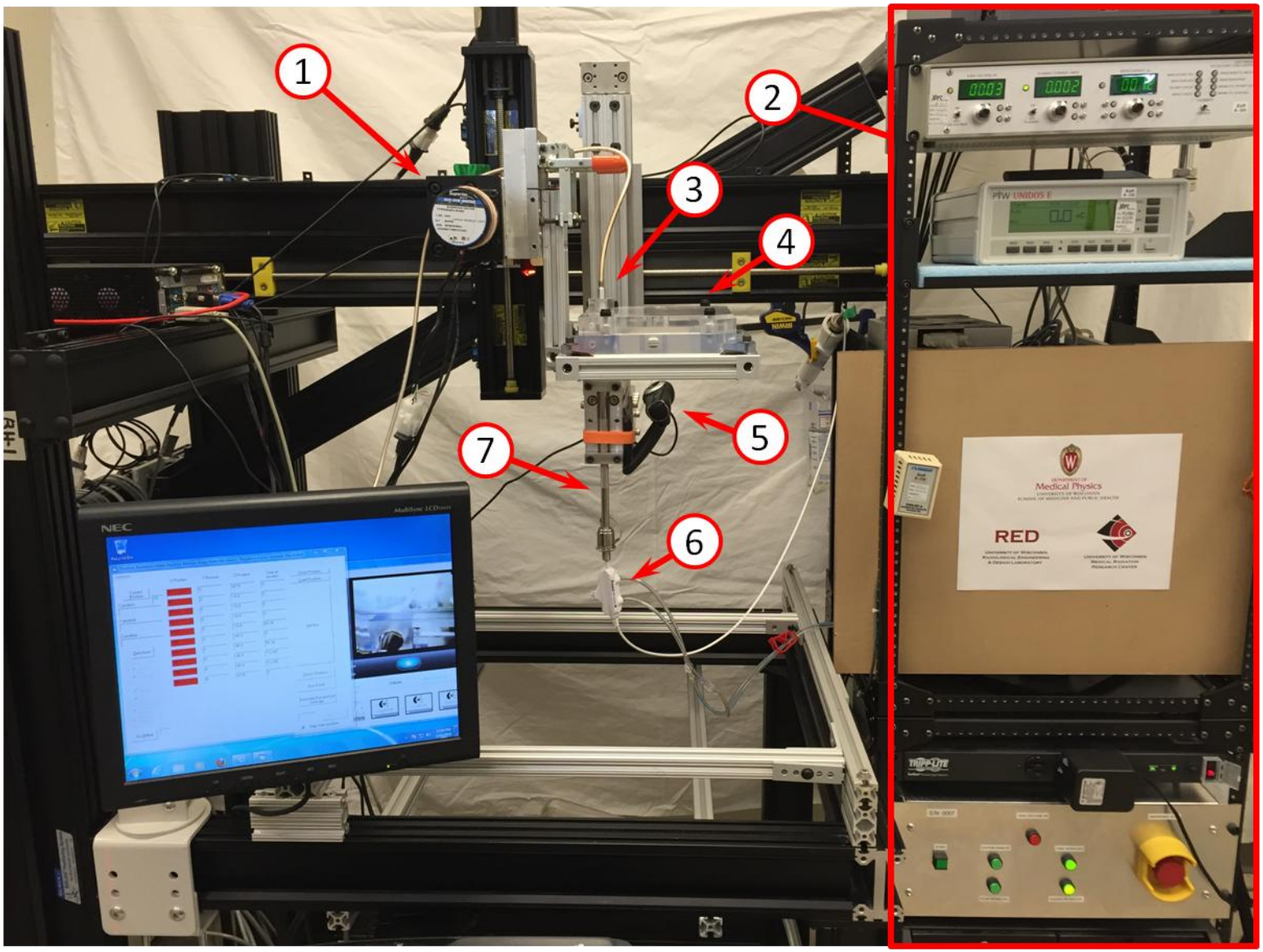

Figure 3.1: Irradiator system showing the 1) 3-axis precision positioning system, 2) source control rack, 3) on-board ionization chamber, 4) irradiator translation sample stage, 5) "beam-eye" video camera, 6) miniature x-ray source, and 7) source surface applicator.

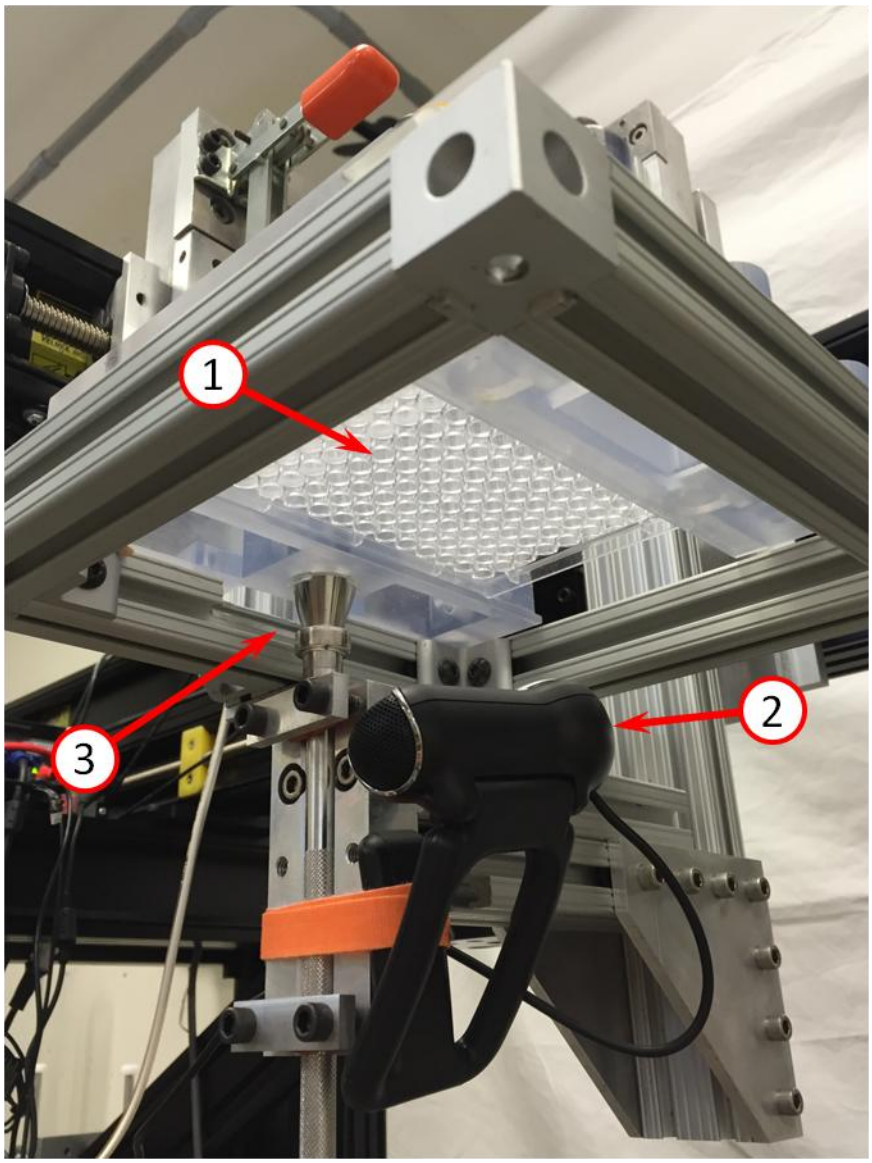

Figure 3.2: Bottom of irradiator system tray showing the 1) 96-well cell culture plate, 2) on-board realtime "beam-eye" camera, and 3) 20 mm irradiator surface applicator.

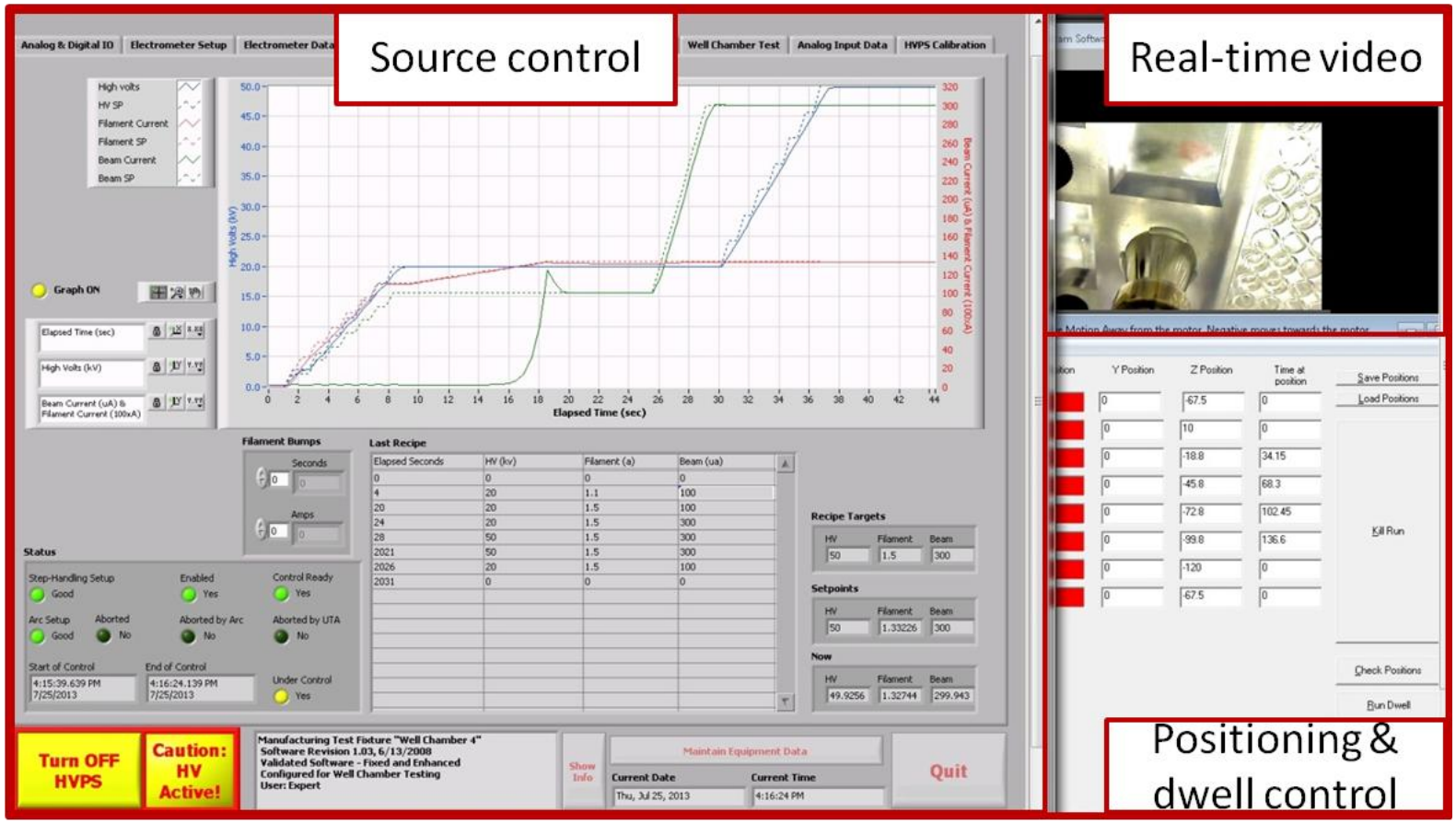

Figure 3.3: Irradiator control user interface.

Figure 3.4: 96-Well cell culture plate. Image courtesy of Corning Inc.

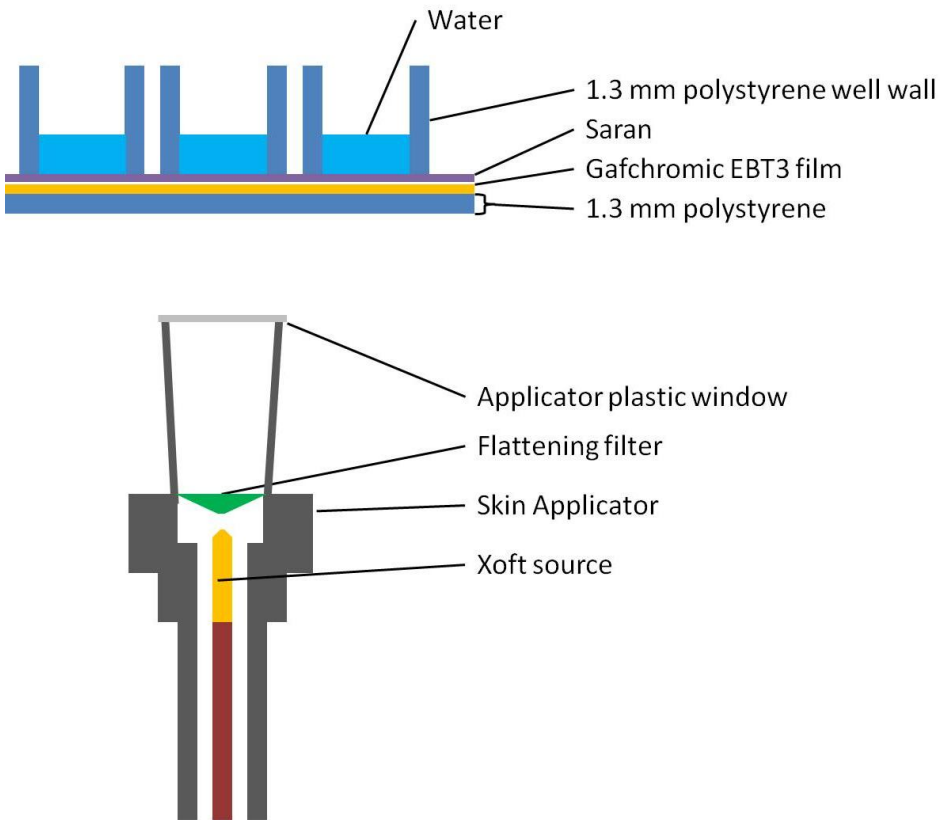

Figure 3.5: Source characterization geometry.

All US Food and Drug Administration (FDA) approved medical electrical equipment must comply with operation requirements and safety standards recommended by the International Electrotechnical Commission (IEC). Currently, there are no IEC guidelines for other devices that utilize x-ray tubes (e.g. radiography and mammography equipment), three important performance characteristics of the system including radiation output stability, radiation field flatness and symmetry, and focal spot resolution at the cellular plane were investigated.

3.2.1 Ionization chamber measurements

Ionization chamber measurements were performed using an on-board Exradin A20 ionization chamber (S/N XR022483) and SuperMAX electrometer (S/N P111024) (Standard Imaging, Middleton, WI). The Exradin A20 is a parallel plate ionization chamber with a total collecting volume of 0.0074 cm^3 and an 7.72 mg/cm^2 Kapton end-window. Negligible stem effect is seen with this chamber due to the end-window geometry. The A20 chamber was calibrated at the University of Wisconsin Accredited Dosimetry Calibration Laboratory (UW-ADCL) using a UW50-M beam quality suitable for work with the Axxent source, the calibration coefficient was N_k=3.854 x 10^8 Gy/C. All measurements were performed with a +300 V chamber bias to collect negative charge, after the chamber and electrometer were allowed to warm up, using five replicate 15 second charge collection measurements.

3.2.2 96-Well cell culture plate film phantom

To evaluate the suitability of the source measurements of field flatness and symmetry were performed using a phantom of a 96-well cell culture plate. The phantom was designed to place radiochromic film at the cellular plane and mimic the cell growth media conditions under which living cells would be irradiated. To accomplish this the bottom of a normal polystyrene 96-well cell culture plate was removed down to the cellular plane using a precise vertical mill

machine. A thin 25 μm layer of polyvinylidene chloride (PVDC, "saran") was glued to the bottom of the wells using ethylene dichloride to ensure the wells would remain water tight. A sheet of polystyrene 1.27 mm thick was cut to replicate the bottom of the wells and aluminum spacers added to position the cellular plane the correct height from the bottom of the plate, as seen in **Figure 3.6**. During measurements the radiochromic film was inserted between the PVDC layer and the polystyrene bottom and the wells were filled with water to provide proper backscatter to the cellular layer (i.e. the film) that would be present during cellular irradiations from the cell culture media shown in **Figure 3.5**.

3.2.3 Radiochromic film

Relative dose distributions were measured using GafChromic® EBT3 film (International Specialty Products, Wayne, NJ). EBT3 film consists of three layers: and active layer between two matte polyester layers as seen in **Figure 3.7**. The active layer in EBT3 film is the same composition of EBT2 film, which has been studied extensively and shown to demonstrate moderate energy dependence at the Axxent source energy [60]. To minimize this effect all film measurements were performed with a dose of 2 Gy to enter the more linear region of dose response for EBT3 film.

Films were scanned on an Epson® Expression® 10000 XL flatbed scanner (Epson America, Long Beach, CA) prior to irradiation so that background subtraction could be performed post-irradiation. Following irradiation, films were allowed 24 hours to fully develop before scanning [60,61]. Images were analyzed using FIJI/ImageJ (National Institutes of Health, Bethesda, MD) and MATLAB® (MathWorks, Natick, MA) [62]. Pre and post-irradiated images were registered using ImageJ plugin StackReg[63].

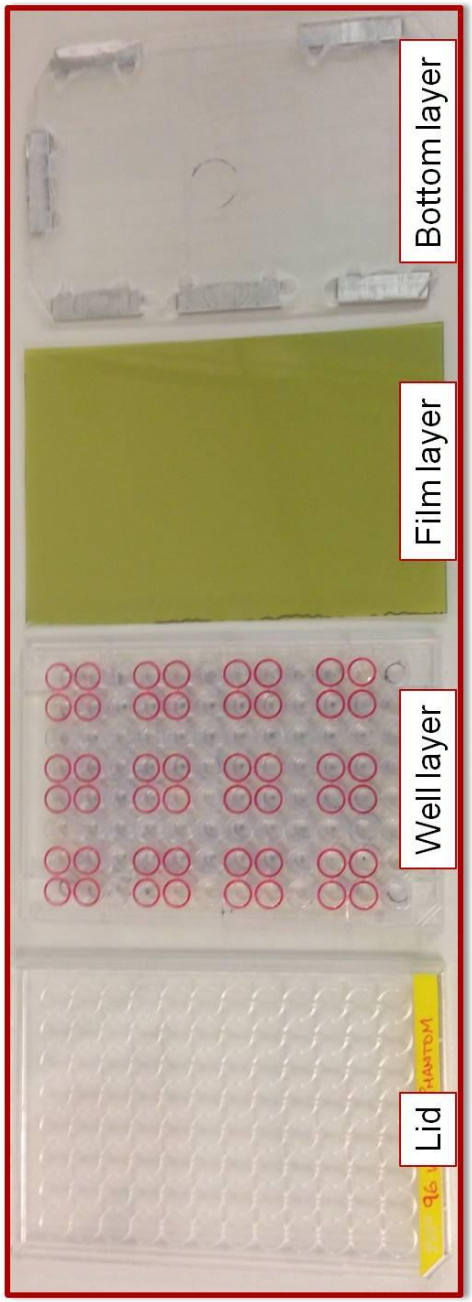

Figure 3.6: 96-Well cell culture plate phantom.

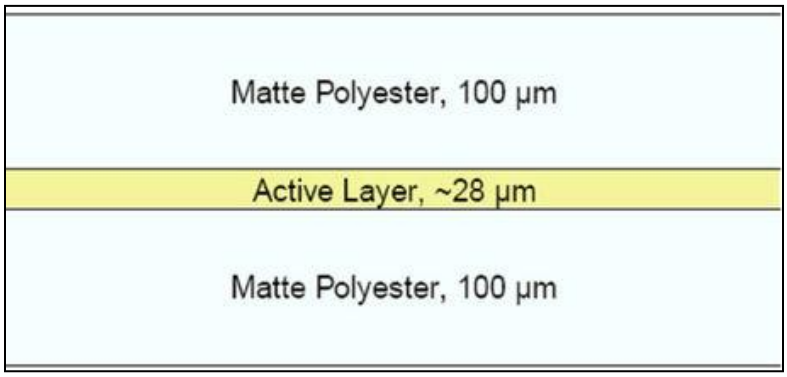

Figure 3.7: GafChromic® EBT3 film layered construction [60].

3.3 Source performance

3.3.1 Output stability

Using the Exradin A20 ionization chamber, set flush to the surface applicator end-window, measurements were taken with the source beam current between 10 - 300 μA to assess the stability of the source at different operating currents. **Figure 3.8** plots the radiation output [mGy/s/μA] as a function of beam current [μA] and shows that the source operated stably between 40 - 300 μA. It is important to note that the stability of the radiation output as a function of beam current is source specific and needs to be performed for each source used during irradiations.

3.3.2 Field flatness & symmetry

Three separate profile measurements were taken using the 96-well cell culture phantom to determine the statistical variation of these values. For each profile, both in-plane (i.e. x-axis) and cross-plane (i.e. y-axis) flatness and symmetry were calculated. The measured relative dose was normalized to the maximum dose delivered within the region of the beam incident on the targeted cell culture well.

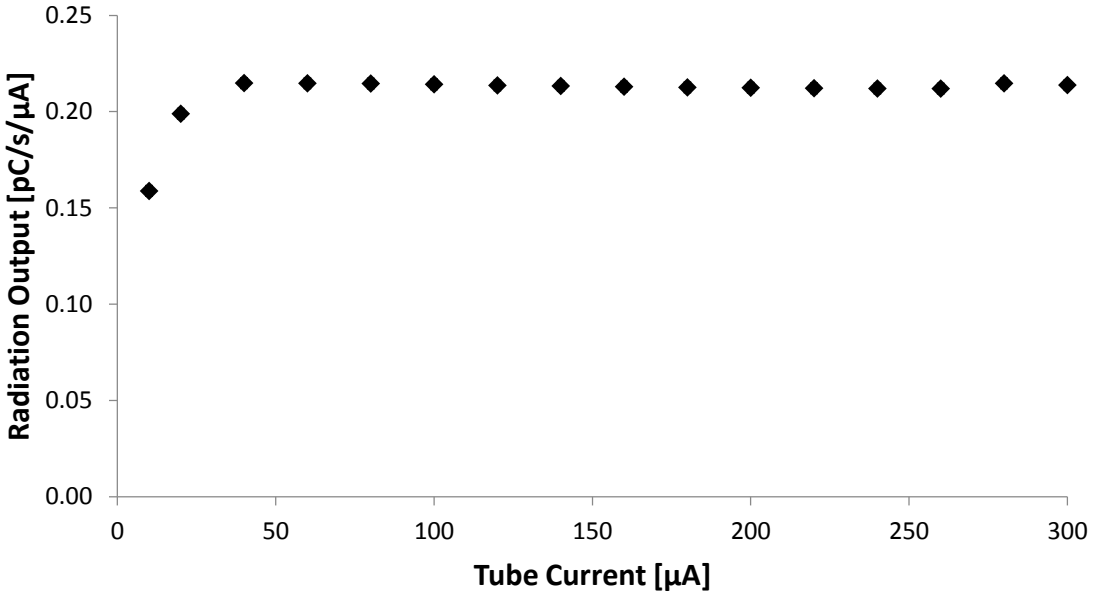

Figure 3.8: Radiation output stability over a range of beam operating current. Note: the error bars are obscured by the data points.

The flatness and symmetry of the beam was calculated only for the region of the beam incident on the targeted cell culture well [64,65]. The flatness is given by:

$$Flatness\ [\%] = \frac{D_{max} - D_{min}}{D_{max} + D_{min}} \times 100 \qquad (3.1)$$

D_{max} and D_{min} are the maximum and minimum dose values within region of the beam incident on the targeted cell culture well. The symmetry is also defined in the region of the beam incident on the targeted cell culture well and is given by the average ratio of doses at symmetric points from the central beam axis. The symmetry is given by,

$$Symmetry\ [\%] = \frac{1}{N} \sum_{n=1}^{N} \frac{D_{left,i}}{D_{right,i}} \times 100 \qquad (3.2)$$

In order to investigate the focal spot resolution at the cellular plane, a set of sequential irradiations were performed. Using the same modified cell culture plate as described in Section 3.2.2, **Table 3.1** shows the flatness and symmetry of the 10 and 20 mm applicator, while **Figure 3.9** shows a representative beam profile from the 10 mm applicator. All flatness values were $\leq 4.0\%$ and all symmetry values were $\leq 1.8\%$.

Table 3.1: Flatness and symmetry of 10 and 20 mm surface applicators.

Applicator	**Flatness (%)**		**Symmetry (%)**	
	In-plane (x-axis)	Cross-plane (y-axis)	In-plane (x-axis)	Cross-plane (y-axis)
10 mm	2.9 ± 1.0	4.0 ± 1.7	1.8 ± 0.9	1.6 ± 0.5
20 mm	2.4 ± 0.2	2.8 ± 1.0	1.1 ± 1.2	0.6 ± 1.0

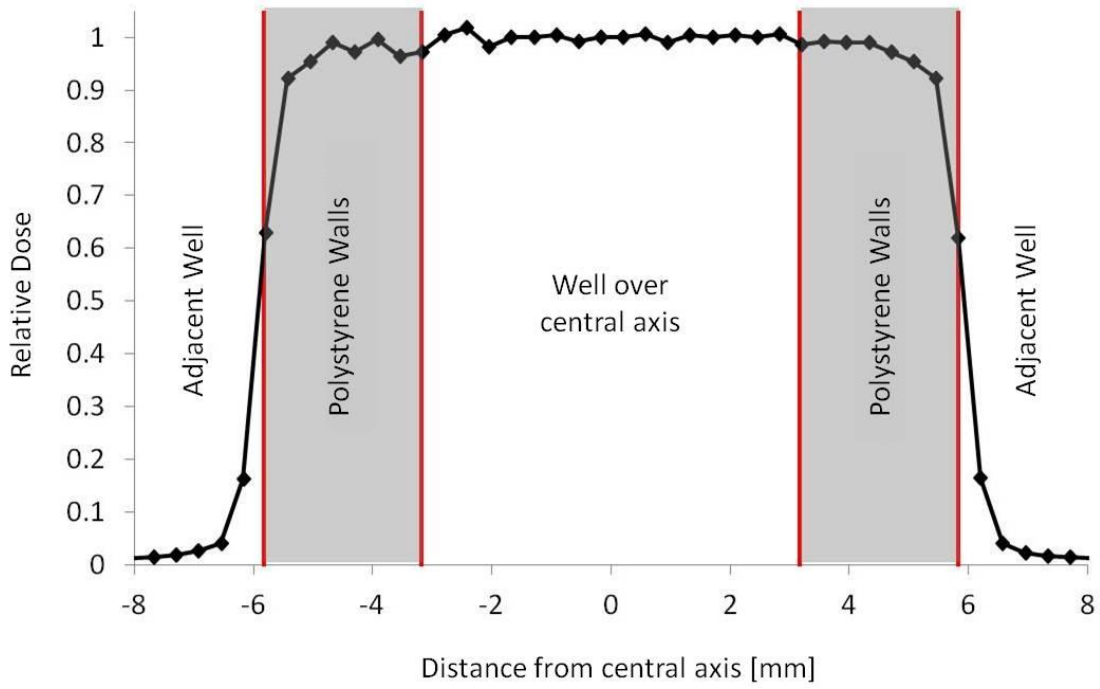

Figure 3.9: Representative beam profile targeting a single well on film phantom. Non-target regions are shaded.

3.3.3 Focal spot resolution and accuracy

In order to investigate the focal spot resolution at the cellular plane, a set of sequential irradiations using the 10 mm applicator was performed using three irradiation methods (**Figure 3.10)**, the focal spot resolution helped determine the best method for use in a 96-well plate format. Using the same modified cell culture plate as described in Section 3.2.2, EBT-3 film was irradiated with three different focal spot arrangements: every well, every-other well, and every-two wells. A total of 2 Gy was delivered to each spot.

In addition, the full-width at half-max (FWHM) was calculated by linear interpolation of the 50% relative dose points in the profile penumbra region to determine the center of the dose profile. Peak-to-peak translation distances were calculated from these values to assess the accuracy of the precision positioning system. The translation of the plate over the fixed source can be performed with negligible relative error: 0.3 ± 0.1 %.

As seen in **Figure 3.11** irradiating each well leads to unacceptable overlapping of radiation fields. By leaving the adjacent wells next to the targeted well blank a homogeneous dose can be delivered, this is further reinforced when two wells are left blank. For the final irradiation method used in this project a 20 mm surface applicator was used to irradiate groups of four wells leaving adjacent wells blank for field overlap as seen in **Figure 3.12**. This method has the advantages of reducing the overall irradiation time per plate and giving experimental replicates to increase the statistical power of bioassay results.

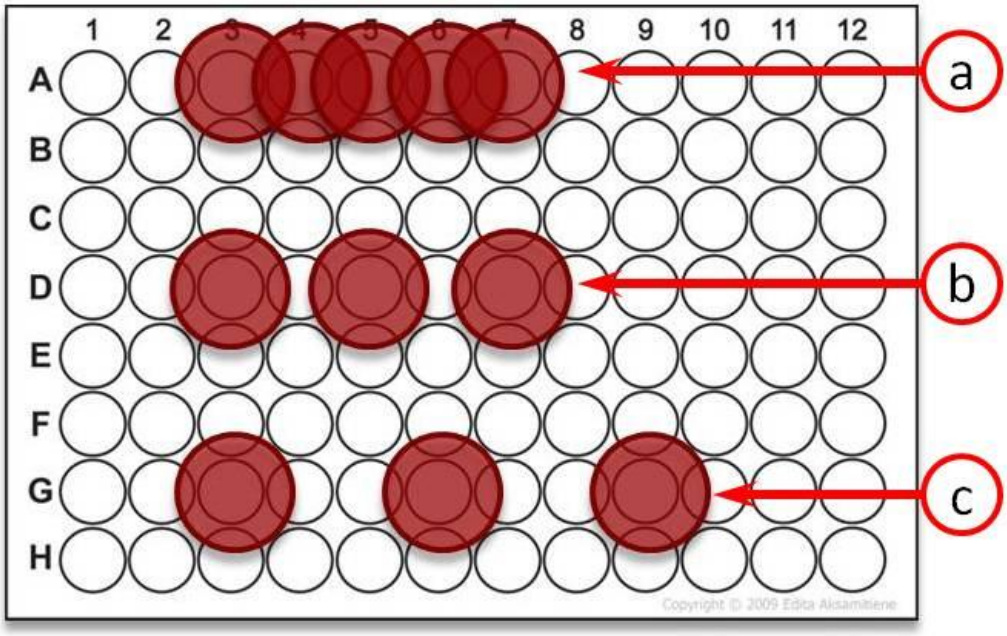

Figure 3.10: Beam irradiation methods, a) irradiating every well, b) skipping a single adjacent well, c) skipping two wells.

(a)

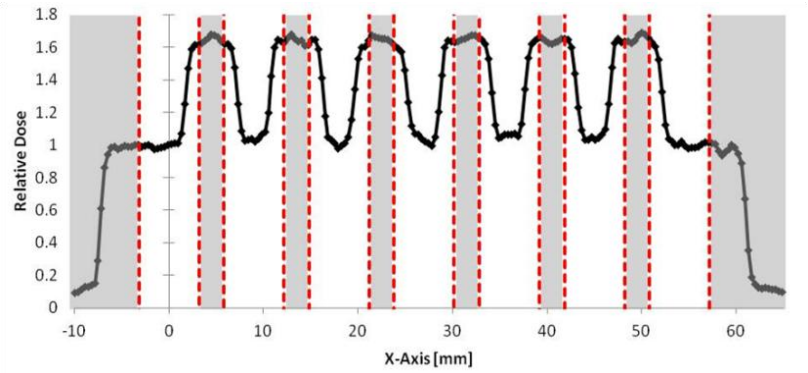

(b)

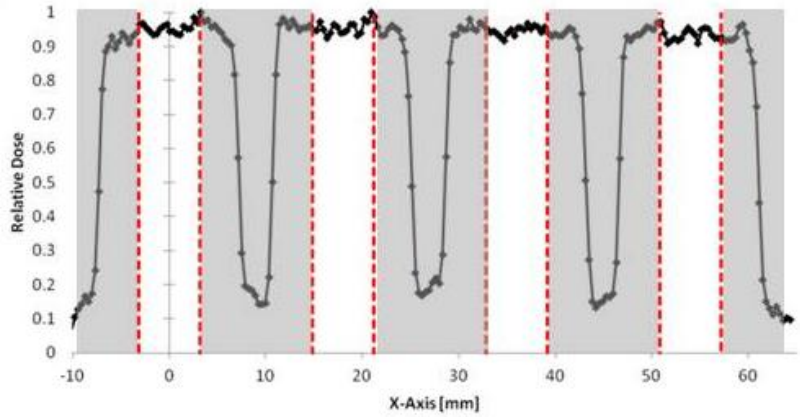

(c)

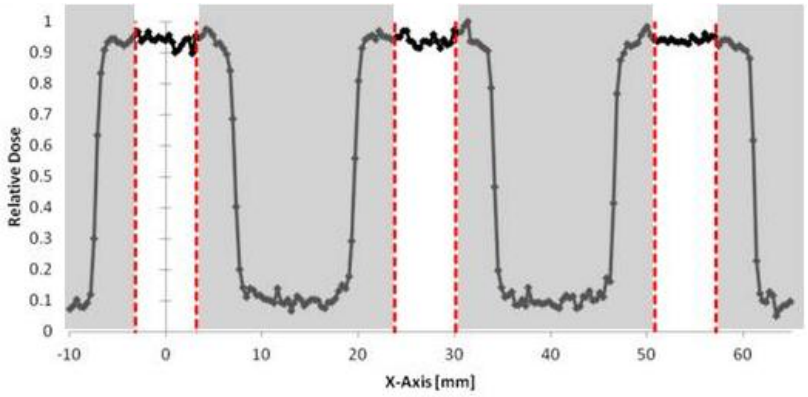

Figure 3.11: Beam irradiation method profiles, a) irradiating every well, b) skipping a single adjacent well, c) skipping two wells. Non-target regions are shaded.

(a)

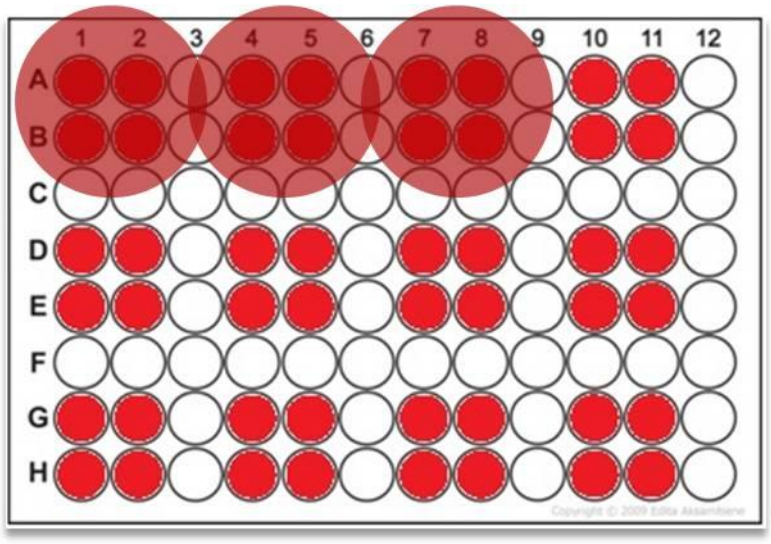

(b)

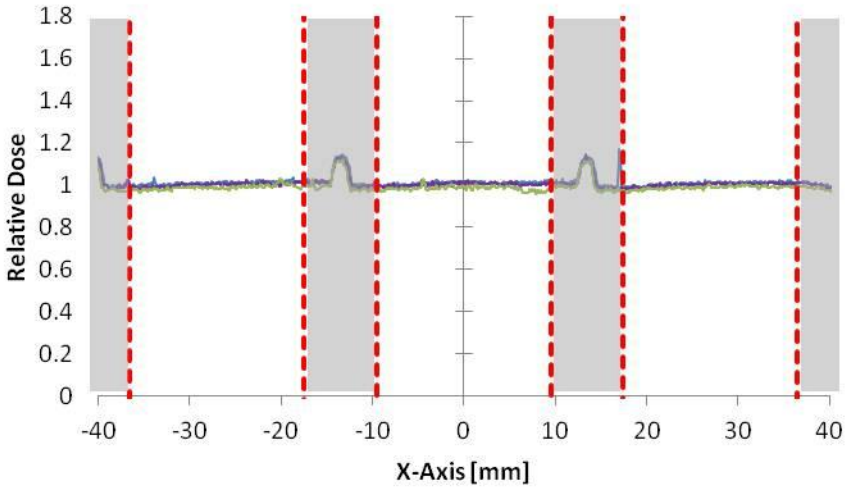

Figure 3.12: a) Four well irradiation method and b) field profiles with non-target regions shaded.

3.4 Irradiator dose formalism

Precise dose delivery is based on an air-kerma rate measurements using the on-board Exradin A20 ionization chamber. A series of correction factors are applied to determine the dose to water at the cellular plane. The dose to the cellular plane is determined using the formalism described in Equations 3.3 and 3.4 based on the formalism derived by Fulkerson et. al. [13]:

$$\dot{K}_{air} = \dot{M} \cdot N_k \cdot P_{elec} \cdot P_{TP} \cdot P_{cham} \cdot P_{POM} \tag{3.3}$$

$$\dot{D}_{cells} = \dot{K}_{air} \cdot P_{GEO} \tag{3.4}$$

Where the dose-rate to the cells, $\dot{D}_{cells}$, is determined by multiplying the air-kerma rate, $\dot{K}_{air}$. with a dose to water at the cellular plane conversion factor, P_{GEO}, that was determined by Monte Carlo methods as described in section 3.4.1. The air-kerma rate is calculated using $\dot{M}$, the measured charge reading over a 15 second period [A], N_k, the ionization chamber calibration coefficient [Gy/C] for the Exradin A20 ionization chamber using a UW60-M beam quality, and P_{elec}, the electrometer calibration coefficient. P_{TP}, is the correction factor for air density in the ionization chamber collection volume as given by:

$$P_{TP} = \frac{(273.15+T)}{(273.15+22.0)} \cdot \frac{(101.33)}{(P)} \tag{3.5}$$

where T is the ambient air temperature [°C] and P is the ambient air pressure [kPa]. P_{cham} is a chamber replacement factor as given by:

$$P_{cham} = \frac{D_a^2}{D_{cham}^2 \cdot D_{irr}} \tag{3.6}$$

where D_a is the dose to the air volume at the ionization chamber point of measurement, D_{cham}, is the dose to the chamber volume at the point of measurement as determined by EGSnrc Monte Carlo [13], and D_{irr} is the relative dose measured by the ionization chamber in the irradiator geometry to account for additional scattering into the ionization chamber collection volume.

P_{POM} is a correction factor for the point-of-measurement within the ionization chamber and is given by:

$$P_{POM} = \left(\frac{SSD+d}{SSD}\right)^2 \tag{3.7}$$

where the SSD is the source to ionization chamber entrance window distance and d is the distance from the ionization chamber entrance window and the effective point-of-measurement within the chamber volume. Finally the corrected air-kerma rate , K_{air} is convolved with a Monte Carlo determined dose to water at the cellular plane correction factor, P_{GEO}.

3.4.1 Monte Carlo

To determine the dose to water at the cellular plane correction factor, P_{GEO}, Monte Carlo was performed using MCNP5. This model accounts for the attenuation of the primary beam by air and the cell culture plate bottom as well as backscatter introduced by the media overlying the cells. At the photon energies generated by the source the range of secondary electrons in water is negligible allowing the approximation of the collision kerma with an F6 "heating" tally [13]. A full source, applicator, and cell culture plate model was used in MCNP5 with tally regions at the surface of the applicator and at varying depths in the cell culture well seen in **Figure 3.13**, the tally region used in this model are cylinders of radius 2.616 mm with a height of 0.1 mm. Water was included within the wells to simulate cell culture media and provide full backscatter conditions to the cellular plane. The MCNP5 model accounts for all of the materials chemical

composition and densities. A total of 2 X 10^8 source particles were used in all Monte Carlo simulations to ensure that the relative error within each tally was less than 0.5%. The dose to water at the cellular plane was extrapolated back to the well bottom/water interface and corrected for the finite thickness of the tally regions as shown in **Figure 3.14**. The dose to water at the cellular plane for the 10 and 20 mm surface applicators is presented in **Table 3.2**.

Table 3.2: Dose to water at the cellular plane, P_{GEO}, for the 10 and 20 mm surface applicators.

Applicator	**P_{GEO}**
10 mm	0.5643
20 mm	0.5744

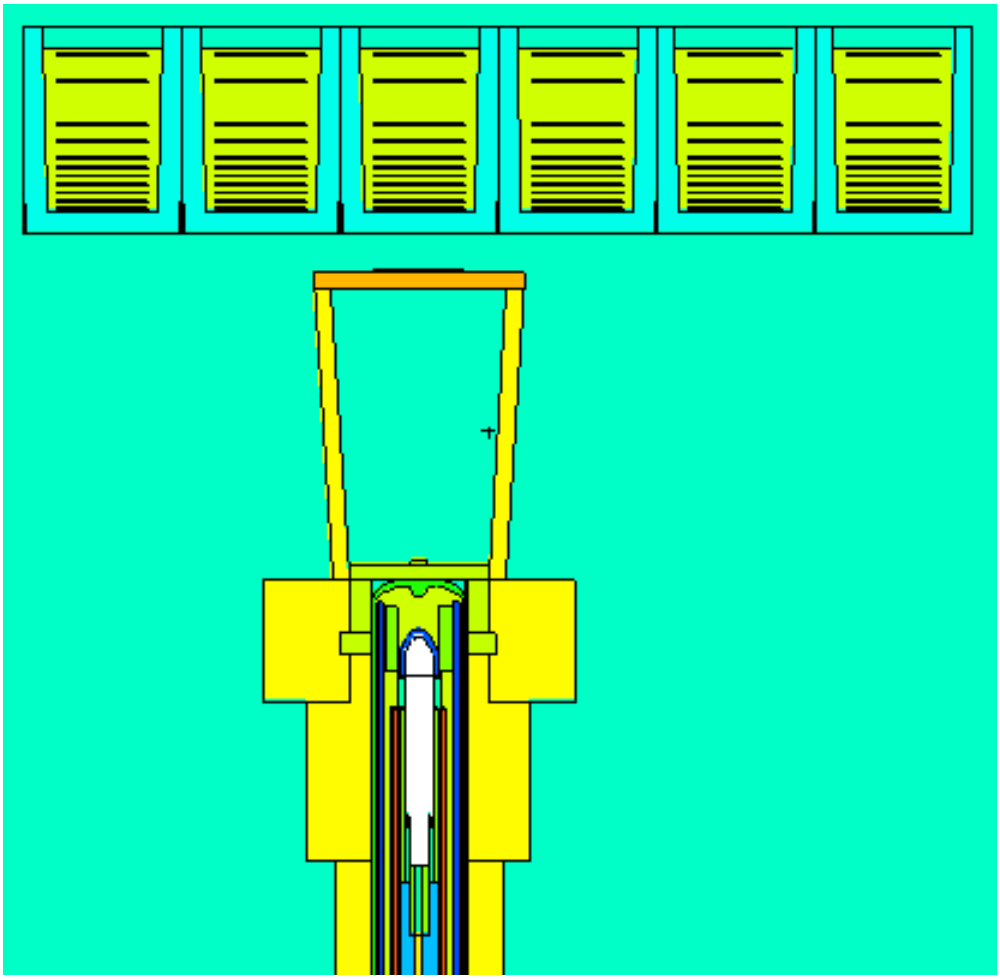

Figure 3.13: MCNP5 model of source, applicator, and 96-well cell culture plate.

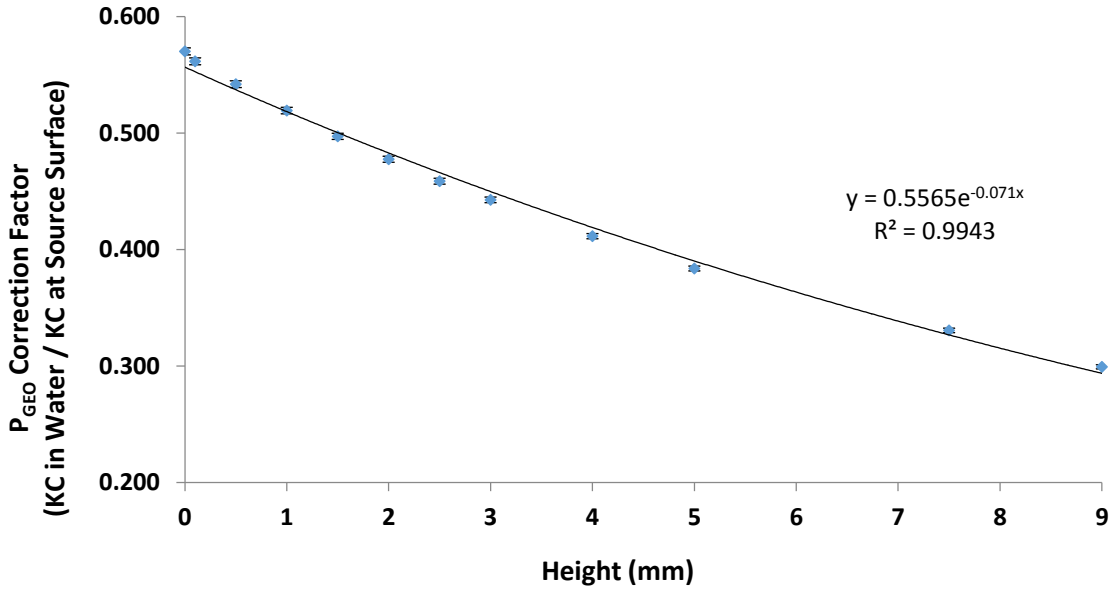

Figure 3.14: Dose to water at the cellular plane, P_{GEO}.

3.4.2 Air-kerma rate & P_{GEO} uncertainty

The estimated combined uncertainty for air-kerma rate measurements using the Exradin A20 ionization chamber are shown in **Table 3.3**. The uncertainty of this measurement includes the UW-ADCL reported chamber calibration and electrometer uncertainties, air density correction, chamber position with respect to the surface applicator window, source positioning within the surface applicator, uncertainty of the effective point of measurement within the ionization chamber collection volume, scatter correction for irradiator geometry, and measurement reproducibility.

The source positioning uncertainty was determined through Monte Carlo simulations by observing a 0.5 mm shift, based on manufacturer tolerances, in source positioning within the surface applicator. The largest contributor to uncertainty in the air-kerma rate measurement is the uncertainty in the effective point of measurement in the Exradin A20 ionization chamber, this value is based on the result of a 0.7 mm shift in the effective point of measurement. Both the source positioning and effective point of measurement uncertainties were applied as reported by Fulkerson et al. [13]. The uncertainty associated with the additional scatter correction introduced by the irradiator geometry was based on the standard deviation of difference in measurements taken with the ionization chamber alone and in the translation stage. Finally, measurement reproducibility was calculated as the percent standard deviation of the mean of repeated measurements. The total expanded uncertainty in the air-kerma rate measurements is 3.84% as seen in **Table 3.3**.

Table 3.3: Uncertainty budget for the Exradin A20 measurements of air-kerma rate [13].

Component	Type A %	Type B %
Chamber calibration		0.50
Electrometer calibration		0.10
Air Density	0.10	0.10
Chamber positioning		0.50
Source positioning		0.08
Effective point-of-measurement correction		1.70
Scatter correction	0.52	
Measurement reproducibility	0.05	
Combined uncertainty	0.53	1.85
Total uncertainty (k=1)	**1.92**	
Expanded uncertainty (k=2)	**3.84**	

The estimated uncertainty in the Monte Carlo derived dose to water at the cellular plane, P_{GEO}, is shown in **Table 3.4**. The uncertainty of this correction factor includes the geometry of the tally regions, geometry of the cell culture plate, energy spectrum, atomic cross sections, and reported simulation tally statistics. The uncertainty in the geometry of the tally region, energy spectrum, and atomic cross sections was previously determined for this Monte Carlo model by Fulkerson et al. [13]. The uncertainty associated with the cell culture plate was determined through Monte Carlo simulation where independently the thickness of the polystyrene well bottom was changed ± 0.05 mm while the air gap between the applicator and the cell culture plate was changed ± 0.005 mm based on the uncertainty in a precision gap gauge used to position the applicator. The total expanded uncertainty in dose to water at the cellular plane is 4.13 %.

Table 3.4: Estimated uncertainty in the dose to water at the cellular plane, P_{GEO}, correction factor for the irradiator system.

Component	Type A %	Type B %
Monte Carlo uncertainties		
Geometry of tally region		0.65
Geometry of culture plate		0.23
Energy Spectrum		0.25
Atomic cross-sections		0.13
Tally Statistics	0.11	
Combined uncertainty	0.11	0.75
Type A and Type B combined	0.75	
Uncertainty in air-kerma rate	**1.92**	
Total uncertainty (k=1)	**2.06**	
Expanded uncertainty (k=2)	**4.13**	

3.5 Thermoluminescent dosimeter dosimetry verification

To verify the dosimetric formalism for the irradiator system thermoluminescent dosimeters (TLD-100) were irradiated to a nominal 100 cGy dose and compared to a three dose-point ^{60}Co calibration curve. All dosimeters were handled with vacuum tweezers and fully annealed at 400 °C for 1 h, cooled on aluminum plates, and finally annealed for 24 h at 80 °C. The TLDs were read at least 24 h after irradiation using a Harshaw 5500 TLD reader (Thermo Fisher Scientific Inc., Waltham, MA) that uses hot nitrogen gas to heat the TLDs for readout [66,67]. The time temperature profile used to read TLDs includes an initial heating to 50 °C then followed by a data collection region that heats the TLD at 13 °C/s to a maximum temperature of 350 °C. Each TLD was exposed to 100 cGy using a Theratronics T1000 ^{60}Co (Best Theratronics Ltd., Ottawa, Ontario, Canada) teletharapy unit to determine individual TLD chip factors.

A total of 30 TLDs were used to construct a ^{60}Co calibration curve of 50 cGy, 100 cGy, and 200 cGy. Ten TLDs irradiated using the irradiator system were exposed to a 100 cGy dose to increase the signal-to-noise ratio of the results while also avoiding the TLD-100 supralinearity

response found at higher doses [68]. The following equation was used to determine the dose delivered to individual TLDs:

$$D(r,\theta) = \frac{R \cdot N \cdot \left(\frac{k_{bq}(Axxent)}{k_{bq}(^{60}Co)}\right)}{C(r,\theta)} \quad (3.8)$$

where R is the TLD reading [nC], N is the calibration coefficient derived from the ^{60}Co calibration curve [cGy/nC], $\frac{k_{bq}(Axxent)}{k_{bq}(^{60}Co)}$ is the intrinsic energy dependance correction factor for the TLDs at the source energies, and C(r,θ) is the Monte Carlo correction factor for material differences of the irradiation geometry.

It has been demonstrated that TLD-100s are highly energy dependant and at the energy of the source used in this irradiator this can be as high as 13% [69]. Previous work by Pike determined that the intrinsic energy dependence correction factor, $\frac{k_{bq}(Axxent)}{k_{bq}(^{60}Co)}$, for the Axxent source to be 0.910 [70]. Recent work by Poudel et al. produced a similar result with the intrinsic energy dependence correction factor at 50 kVp of 0.914, for this investigation Pike's value was used [71]. The material correction factor, C(r,θ), was calculated using Monte Carlo using the following equation:

$$C(r,\theta) = \left[\frac{D_{TLD,Axxent}(r,\theta)}{D_{water,Axxent}(r,\theta)}\right] \cdot \left[\frac{D_{water,^{60}Co}(r,\theta)}{D_{TLD,^{60}Co}(r,\theta)}\right] \quad (3.9)$$

where $\frac{D_{TLD,Axxent}(r,\theta)}{D_{water,Axxent}(r,\theta)}$ is the Monte Carlo derived ratio of the dose to the TLD using the source in a normal geometry and the dose to the TLD with all simulation geometries set to water. The last ratio, $\frac{D_{water,^{60}Co}(r,\theta)}{D_{TLD,^{60}Co}(r,\theta)}$, is similarly the ratio of the dose to water to the dose to TLD using a ^{60}Co point-source model developed by Mora, et al. [72]. Applying these correction factors to TLD

output using Equation 3.8 the mean dose delivered to the TLDs using the irradiator system was 99.74 ± 3.97 cGy.

3.5.1 Absolute dose verification uncertainty

The estimated uncertainty in TLD measurements used to verify the absolute dosimetry of the irradiator system in shown in **Table 3.5**. In this calculation uncertainty arising from the TLD reproducibility, measurement reproducibility, TLD positioning, TLD reader photomultiplier tube linearity, and TLD reader stability were applied to the TLD measurements. For the development of the ^{60}Co calibration curve the uncertainty associated with the TLD reproducibility, determination of the air-kerma rate, TLD positioning, irradiation time, ^{60}Co field uniformity, TLD reader photomultiplier tube linearity, and TLD reader stability were applied to the TLD calibration curve measurements. In the determination of the material difference correction factor the reported Monte Carlo uncertainty, photon spectrum, atomic cross section, tally region geometry, and cell culture plate uncertainties were considered. Finally, the uncertainty in the ^{60}Co Monte Carlo simulation includes the reported Monte Carlo uncertainty, photon spectrum, atomic cross section, tally region geometry, and energy dependence correction factor as previously discussed in section 3.3.2 [70]. These factors contribute to an overall expanded uncertainty of 3.98%.

Table 3.5: Estimated uncertainty for the TLD verification of measured absolute dose to water at the cellular plane [13].

Component	Type A %	Type B %
R-corrected TLD reading		
TLD reproducibility	0.75	
Measurement reproducibility	0.12	
TLD positioning		0.02
PMT linearity		0.1
Reader Stability		0.2
N-calibration coefficient (measured)		
TLD reproducibility	0.31	
Air-kerma rate determination		0.8
TLD positioning		0.01
TLD irradiation time		0.01
Field uniformity		0.1
PMT linearity		0.1
Reader Stability		0.2
Phantom correction (Xoft source)		
MC tally statistics	0.25	
Photon spectrum		0.25
Atomic cross-sections		0.13
Geometry of tally region		0.65
Geometry of culture plate		0.23
Phantom correction (^{60}Co source)		
MC tally statistics	0.07	
Photon spectrum		0.03
Atomic cross-sections		0.01
Energy dependence correction	0.99	0.97
Combined uncertainty	1.31	1.50
Total uncertainty (k=1)	**1.96**	
Expanded uncertainty (k=2)	**3.98**	

3.6 Summary

Modern cancer biology research often utilizes high-throughput assays performed in multi-well plates (e.g. 96- or 384-wells per plate) that can be rapidly analyzed using high sensitivity endpoint assays. Current x-ray or radioactive source-based irradiators are incapable of varying the dose and/or dose-rate across the multiple wells in an individual microplate. This necessitates the comparison across multiple plates for investigators interested in either dose or dose/rate effects. Given the small volume of the wells in multi-well plates, even small differences in the volume of media overlying the cells can result in important differences in the dose received for "top-down" irradiators. The location of a plate within the radiation field can also influence homogeneity across a plate due to the "heel effect" leading to subtle biases in assay interpretation. Important dosimetry and calibration characteristics (i.e. dose build-up region, beam attenuation, and beam scatter) of these irradiators may be unknown to the end user. This gap in irradiator specificity and user knowledge can result in significant deviation between delivered dose and intended dose that ultimately adversely impacts experimental results and reproducibility.

The production of this irradiator system leverages the increased productivity and capability offered by the newest generation of instrumentation used in the radiobiology laboratory. The proposed system provides an initial framework for the rapid analysis of *in vitro* cellular radiation sensitivity. Better understanding of the biological mechanisms that influence radiation sensitivities will pave the way towards truly delivering personalized medicine in the radiation oncology clinic.

While several novel irradiation devices have been developed in the last decade these mainly focus on producing thin micro-beams of several hundred microns in width and may require custom fabricated cellular growth plates that are incompatible with standard bioassay

instrumentation [3,4]. Our system was designed from the beginning with the radiobiology researcher in mind to deliver highly uniform, full-well dose to standard cell culture plates. Furthermore, our system incorporates an on-board ionization chamber for full NIST traceable verification of dosimetry prior to an irradiation cycle capable of both delivering multiple doses and dose-rates within the same cell culture plate while traditional Cs-137 and cabinet x-ray irradiators are only capable of delivering single dose and dose-rates to an entire plate [5].

Chapter 4

Biovalidation of Irradiator System

The study of the radiosensitivity of cells in culture has been an important component of radiobiology research for nearly a century [1]. Many investigators continue to utilize self-shielded radioactive sources utilizing ^{137}Cs that currently require background checks and security clearance to access in addition to significant overhead to maintain [2]. These irradiators often require careful placement of samples within the housing to avoid inhomogeneous dosing and, depending on the design, can suffer from dose gradients due to shutter lag. Due to increasing concerns about the management and security of radioactive materials in research environments, there has been a gradual and likely permanent shift to machine-based x-ray irradiators [2]. Other factors such as lower cost, smaller physical footprint and easier maintenance add to the appeal of these systems. Conventional x-ray irradiators used to investigate biological responses are built to provide maximum versatility to radiobiology researchers by accommodating small animals, tissue samples, and cellular applications.

In this investigation a high-throughput micro-irradiator was developed that is capable of delivering multiple dose and dose-rates within a single cell culture microplate. We have previously described the physical characteristics of this system [5]. The design of any high

throughput technology for *in vitro* biology research must limit the impact of mechanical and environmental stresses on the cells being tested. Therefore, in order to evaluate the overall robustness of an irradiator, biological validation using assays with well-characterized linear dose-response relationships were performed. To biologically validate this system several assays were used that focused on the early biologic events seen following a dose of ionizing radiation including: (1) the production of inter-cellular reactive oxygen species, (2) the production of physical DNA double strand breaks, and (3) early signals of the DNA double-strand break repair pathway.

4.1 Biological validation methodology

All assay reagents, antibodies, and protocol recipes are listed in **Table 4.1**. All experiments in the biological validation were performed using TERT immortalized human tonsillar epithelial (HTE) cells. Cells were cultured in serum free media at 37°C with 5% CO_2 as we have previously described (Kimple et al. [59]).

4.1.1 Intracellular reactive oxygen species assay

HTE cells were seeded ($2.0x10^4$ cells/well) to achieve >90% confluence the following day in a flat-bottom 96-well plate. The next day, immediately before use, the ROS reactive dye, chloromethyl-H_2DCFDA was dissolved in dimethyl sulfoxide (DMSO) to a 1 mM stock concentration. The dye was further diluted in phosphate buffered saline (PBS) to yield a final cell loading concentration of 5 μM. Cell culture media was removed from the 96-well plate and the cells were washed with PBS prior to loading. Chloromethyl-H_2DCFDA dye was then loaded (5 μM final concentration in PBS) at 100 μL per well and incubated at 37° C for 5 minutes. After the

dye was loaded the cells were then washed in PBS and maintained in 100 μL of phenol-red free complete media during treatment [73]. The 96-well plate was then differentially irradiated in groups of 4 wells between 0-8 Gy. After radiation exposure, the cells were immediately placed on a fluorescent plate reader (SpectraMax i3, Molecular Devices, CA, USA) and total well fluorescence determined using excitation 510 nm (bandwidth 9 nM) and emission 550 nm (bandwidth 15 nM). Data analysis was performed using GraphPad Prism (GraphPad Software, Inc., La Jolla, CA, USA). The average per well signal (relative fluorescence units) was graphed with the 95% confidence interval shown.

4.1.2 Single cell gel electrophoresis DNA DSB assay

HTE cells were seeded ($2.0x10^3$ cells/well) and differentially irradiated 2 days later at approximately 40% confluence. Media was aspirated and 50 μL of trypsin was added, and then cells were incubated at 37° C for 5 minutes. The 8 wells per dose point were amalgamated in PBS with 2% FBS to achieve high cell counts with >80% live cells. Cells were centrifuged at 4° C at 1600 RPM for 6 minutes and then suspended in 50 μL PBS for cell counting with trypan blue. Samples were then diluted in PBS to achieve $1.0x10^5$ cells/mL. The sample was then mixed with 37° C LM Agarose at a 1:10 ratio, and 50 μL of the mixed sample was pipetted onto CometSlides, and the agrose was allowed to solidify at 4° C for ten minutes and immersed in Lysis solution overnight. The following day the slides were removed and placed in 4° C neutral electrophoresis buffer for 30 minutes. Electrophoresis was then performed at a voltage of 1 V/cm for 45 minutes at 4° C. Slides were then immersed in DNA precipitation solution for 30 minutes at room temperature. Following DNA precipitation the slides were immersed in 70% ethanol for 30 minutes at room temperature before drying for 15 minutes at 37° C.To stain the samples

100 μL of diluted SYBR Green Staining Solution for 30 minutes at room temperature, the excess dye was removed and slides washed in dH_2O before final drying for 30 minutes at 37° C. Imaging was performed using a Olympus BX41 fluorescent microscope with a FITC filter at 10X magnification, The Olive tail moment of the comets was calculated by CaspLab (www.casplab.com) [74]. Data analysis was performed using GraphPad Prism (GraphPad Software, Inc., La Jolla, CA, USA). The mean Olive tail moment per dose point is graphed with the 95% confidence interval of these samples utilized [75].

4.1.3 Cellular DNA DSB repair pathway activation

A novel high-throughput approach was developed during this investigation to assess the cellular repair activation following DNA DSB [76]. Cells are first cultured in flat-bottom 96-well plates and differentially irradiated in groups of 4 wells. Following radiation, cells are either immediately assayed to assess maximal γH2AX response or assayed at later time-points to assess DNA repair kinetics. At the desired time-point, media is aspirated from each well and cells are fixed in a volume of 50 μL/well of 4% formaldehyde (methanol free) in phosphate buffered saline (PBS), pH 7.4, for 10 minutes at 37°C and then chilled on ice for one minute. Fixative is aspirated from each well and cells are washed three times with PBS (100 μL/well). Cells are then permeabilized using 90% methanol (in PBS, 50 μL/well) for 30 minutes on ice. Cells are again washed three times with PBS (100 μL/well). Non-specific antibody binding is blocked by incubating cells in incubation buffer (100 μL/well, 0.5 g bovine serum albumen (BSA) in 100 mL PBS) for 10 minutes at room temperature. Buffer is aspirated and cells are incubated with primary antibody (50 μL/well) at a 1:400 concentration, Phospho-Histone H2A.X (Ser 139) (20E3) Rabbit mAb (#9718, Cell Signaling Technology, Danvers, MA, USA) diluted in incubation buffer at room temperature for one hour.

Table 4.1: Biological validation assay reagents, antibodies, and recipes.

Tissue Culture		
Reagent	**Manufacturer**	**Product #**
Kerotinocyte Serum Free Media Kit	Life Technologies, Grand Island, NY, USA	17005-042
Pen-Strep		
Reactive Oxygen Species Assay		
Reagent	**Manufacturer**	**Product #**
Chloromethyl-H_2DCFDA	Molecular Probes, Eugene, OR, USA	C6827
Comet Assay		
Reagent	**Manufacturer**	**Product #**
LM Agarose	Trevigen Inc., Gaithersburg, MD, USA	4250-050-02
Lysis Solution	Trevigen Inc., Gaithersburg, MD, USA	4250-050-01
CometSlides	Trevigen Inc., Gaithersburg, MD, USA	4250-200-03
SYBR Green (10,000X)	Life Technologies, Grand Island, NY, USA	S-7563
Reagent	**Recipe**	
TE Buffer	Tris-HCl (pH=7.5)	10 mM
	EDTA	1 mM
SYBR Green Staining Solution	SYBR Green (10,000X)	0.25 µL
	TE Buffer	7.5 mL
Neutral Electrophoresis Buffer (10X, 500 mL)	Tris Base	60.57 g
	Sodium acetate	204.12 g
	dH_2O	450 mL
	pH=9.0 (adjust pH with glacial acetic acid), adjust volume to 500 mL, filter sterilize, store at room temperature	
DNA Precipitation Solution (1X, 50 mL)	7.5M NH_4Ac	6.7 mL
	95% ETOH	43.3 mL
γH2AX Assay		
Antibody	**Manufacturer**	**Product #**
Phospho-Histone H2A.X (Ser 139) (20E3) Rabbit mAb	Cell Signaling Technology, Danvers, MA, USA	9718
Alexa Fluor® 488 secondary anti-rabbit IgG	Cell Signaling Technology, Danvers, MA, USA	4412
Reagent	**Recipe**	
Incubation Buffer	BSA	1 g
	PBS (pH=7.4)	200 mL

Cells are washed three times (100 μL/well) with antibody-free incubation buffer. Cells are next incubated with 50 μL/well of a fluorescently conjugated (Alexa Fluor® 488) secondary anti-rabbit IgG (#4412, Cell Signaling Technology, Danvers, MA, USA) diluted 1:1000 with incubation buffer for 30 minutes at room temperature. During this incubation, cells are protected from light by wrapping in aluminum foil. Secondary antibody buffer is aspirated prior to a final 3 wash series with 100 μL/well incubation buffer. Cells are maintained in PBS (100 μL/well) for γH2AX foci detection. The plate is then read on a SpectraMax i3 Multi-Mode Microplate Reader Platform with MiniMax 300 Imaging Cytometer (Molecular Devices, Sunnyvale, CA, USA) using the included SoftMax Pro software (v6.3). The software is set to utilize *imaging* read mode and *end-point* read type, see **Figures 4.1-4.3** for a detailed workflow for the SoftMax Pro software.

The proper fluorescence wavelengths are selected based on the specific secondary antibody used. Both plate type and sample wells utilized are selected to identify the wells to be imaged. Four imaging sites per well are utilized to ensure near-total well coverage during analysis. To optimize exposure duration, the *Image Acquisition* settings tab is used to select wells containing the hypothesized minimum and maximum fluorescent signal and acquire images from both of these wells to adjust the fine focus and exposure of the instrument. This process can be repeated as needed to achieve image clarity. Under *Image Analysis* settings, a *cell count* analysis is selected and the sample image is analyzed to confirm that the instrument is properly detecting individual cells. The object size parameters may be adjusted and the image reanalyzed as necessary to ensure distinct nuclei are properly identified. Using the output parameter of *average integrated intensity*, the cell average γH2AX fluorescence is measured. This results in γH2AX fluorescence per cell as this data is normalized by cell count. The selected wells from the plate are then read and the data exported for analysis. We have utilized eight wells (of a 96 well plate) per

condition, which results in the analysis of over $1.6x10^5$ individual cells. Data analysis was performed using GraphPad Prism (GraphPad Software, Inc., La Jolla, CA, USA). The mean per well signal (relative fluorescence units) is graphed with the 95% confidence interval of these samples utilized.

To validate this novel approach HeLa cells were irradiated diferentially, 0-8 Gy, and cell average γH2AX measured. Using this method, a linear response of average per cell fluorescence with increasing dose is seen in HeLa cells (**Figure 4.4**) with histograms (**Figure 4.5**). This approach is able to account for differences in the number of cells per well by providing a per cell intensity rather than a per well intensity. Note that this approach is also amenable to identifying foci formed in response to chemotherapy-induced strand breaks. A dose dependent response of γH2AX foci is seen over a range of etoposide (a known inducer of DNA strand breaks) doses is seen in **Figure 4.6**. As seen in **Figure 4.7**, plating a different number of cells per well results in stable values for the per cell γH2AX intensity across a wide range of cells plated (10^1 - 10^4 cells). The proposed method may also be employed to study detailed DNA repair kinetics following DNA DSB induction as seen in **Figure 4.8**. The entire procedure from start of assay to data analysis takes approximately 3 hours and provides a powerful platform for analysis of γH2AX foci in a high-throughput and reproducible manner.

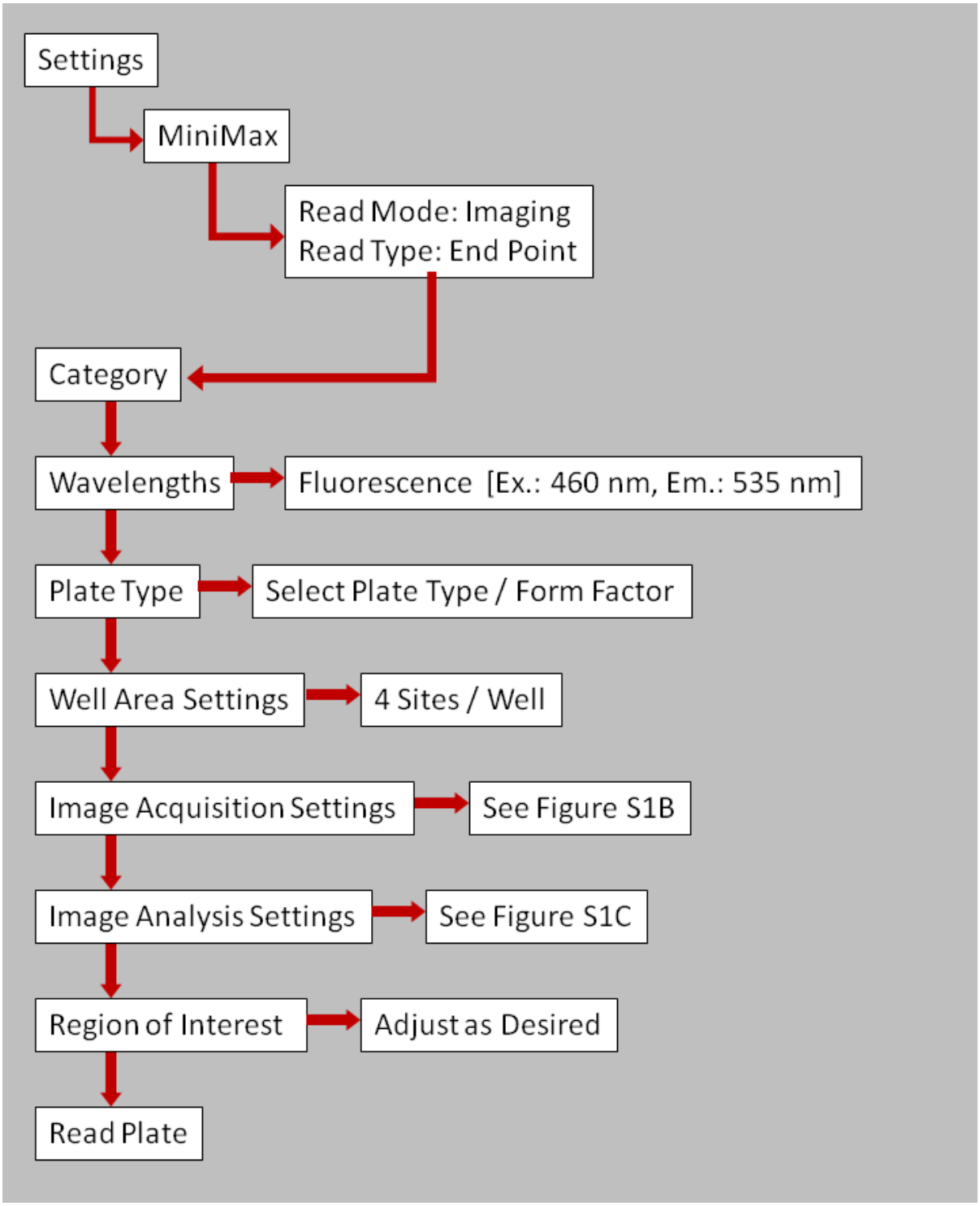

Figure 4.1: Softmax Pro v6.3 analysis workflow.

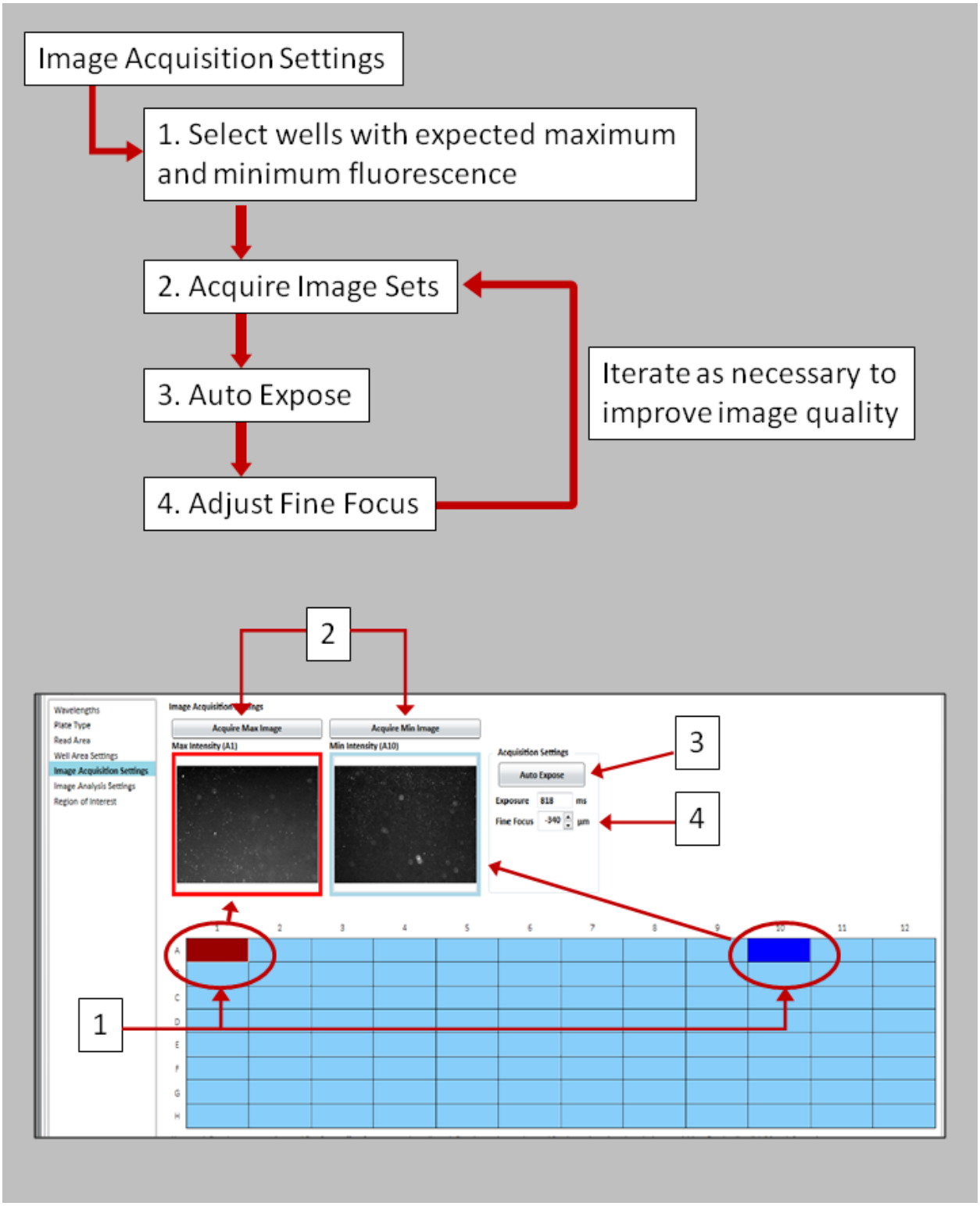

Figure 4.2: Softmax Pro v6.3 image acquisition settings.

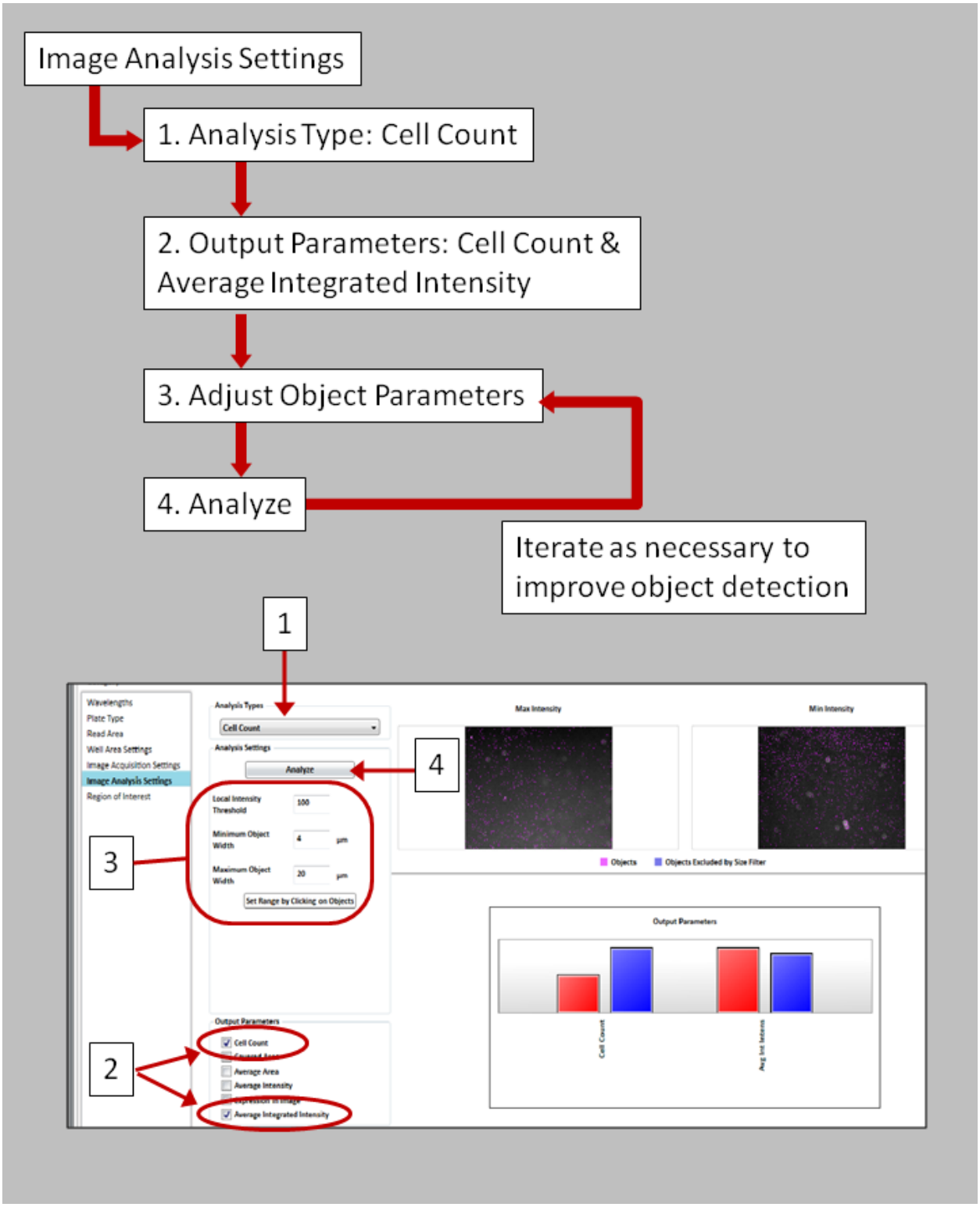

Figure 4.3: Softmax Pro v6.3 image analysis settings.

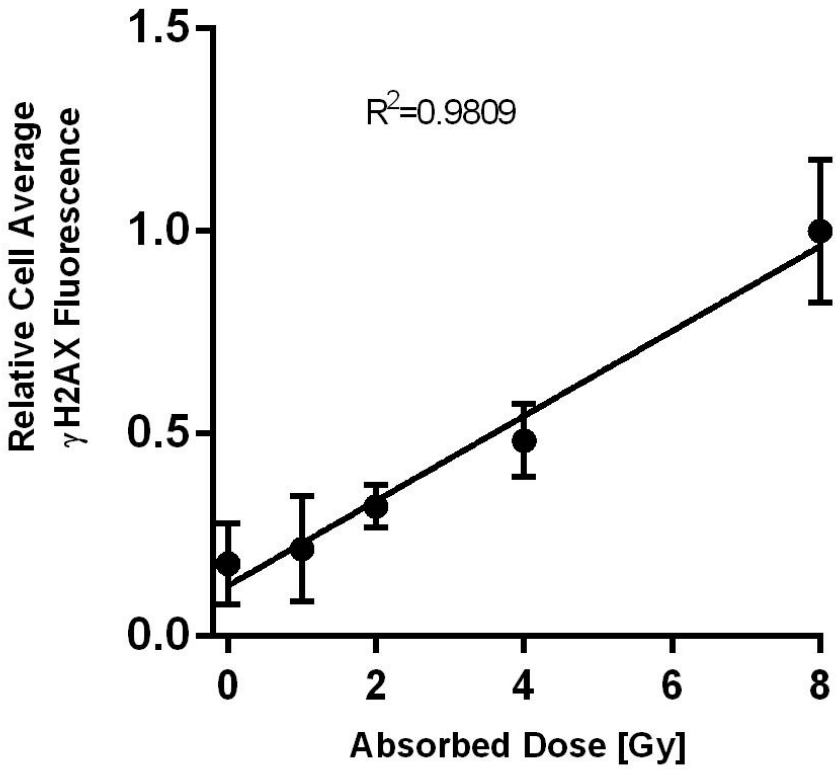

Figure 4.4: Relative cell average γH2AX fluorescence of HeLa cells irradiated with increasing absorbed dose (+/- 95% CI).

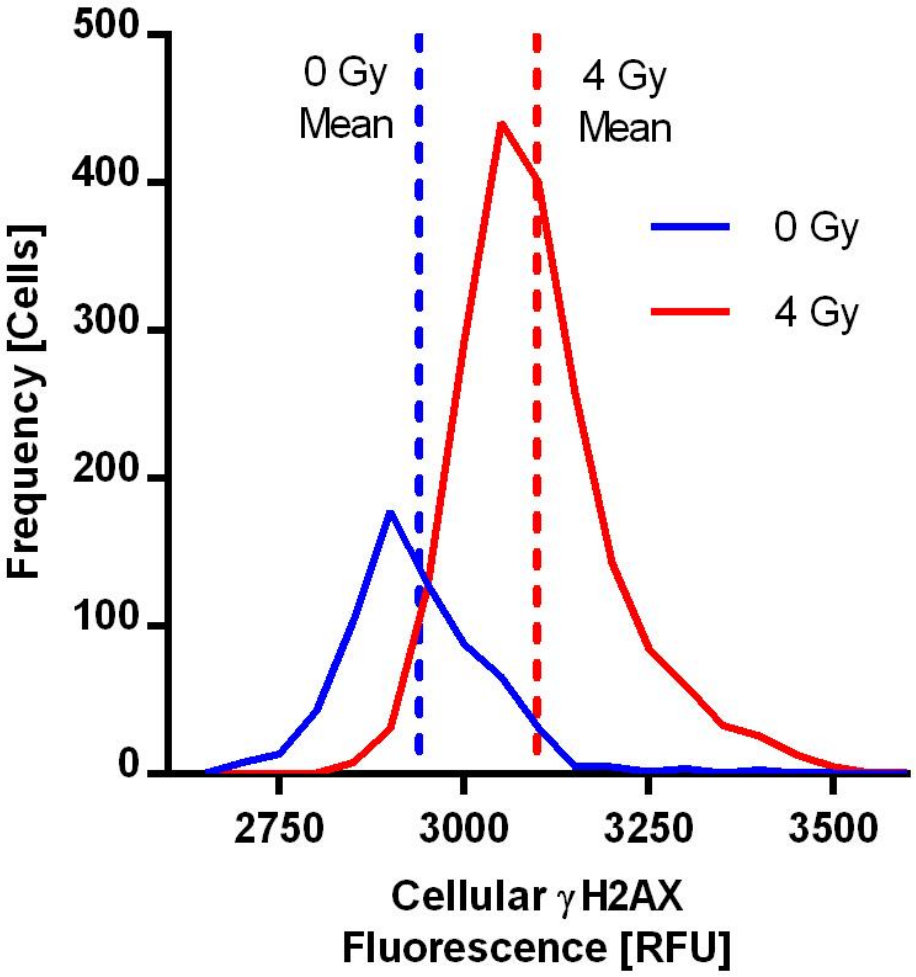

Figure 4.5: Representative histograms showing increased γH2AX fluorescence immediately following a 4 Gy irradiation of HeLa cells (n=8 wells for each dose point).

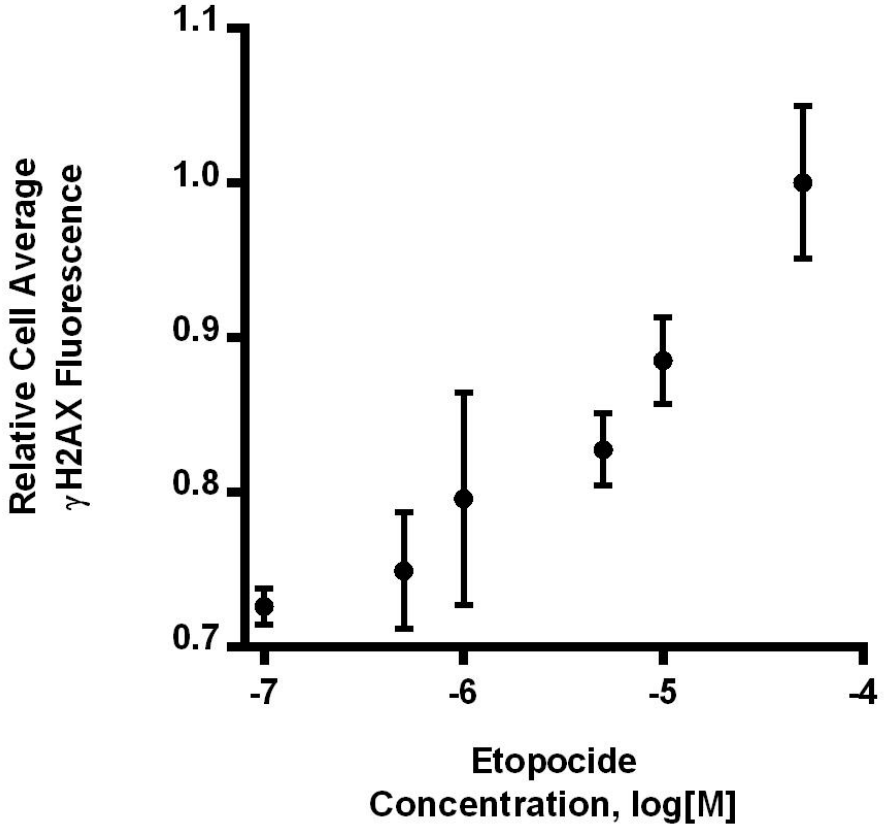

Figure 4.6: HeLa cells treated with various concentrations of etopocide, inducing DNA DSBs, showing excellent sensitivity over a range of drug concentrations.

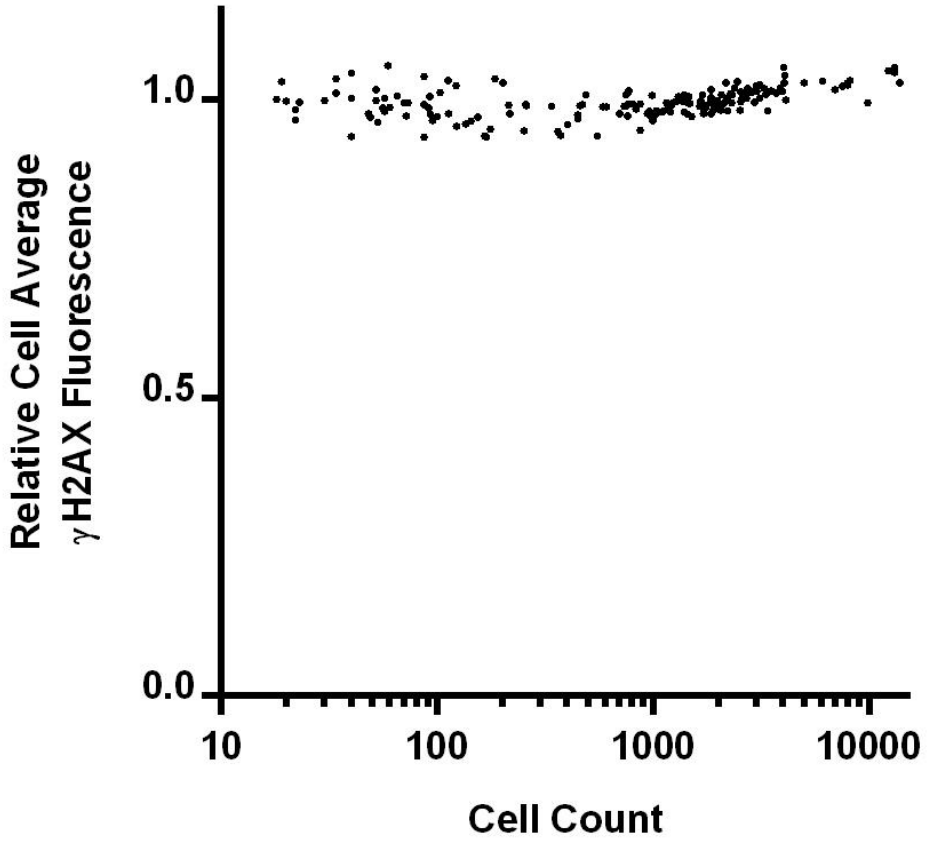

Figure 4.7: Wells containing varied confluency (10^1 - 10^4 cells) of HeLa cells irradiated uniformly to 2 Gy showing γH2AX fluorescence is independent of cell number assayed.

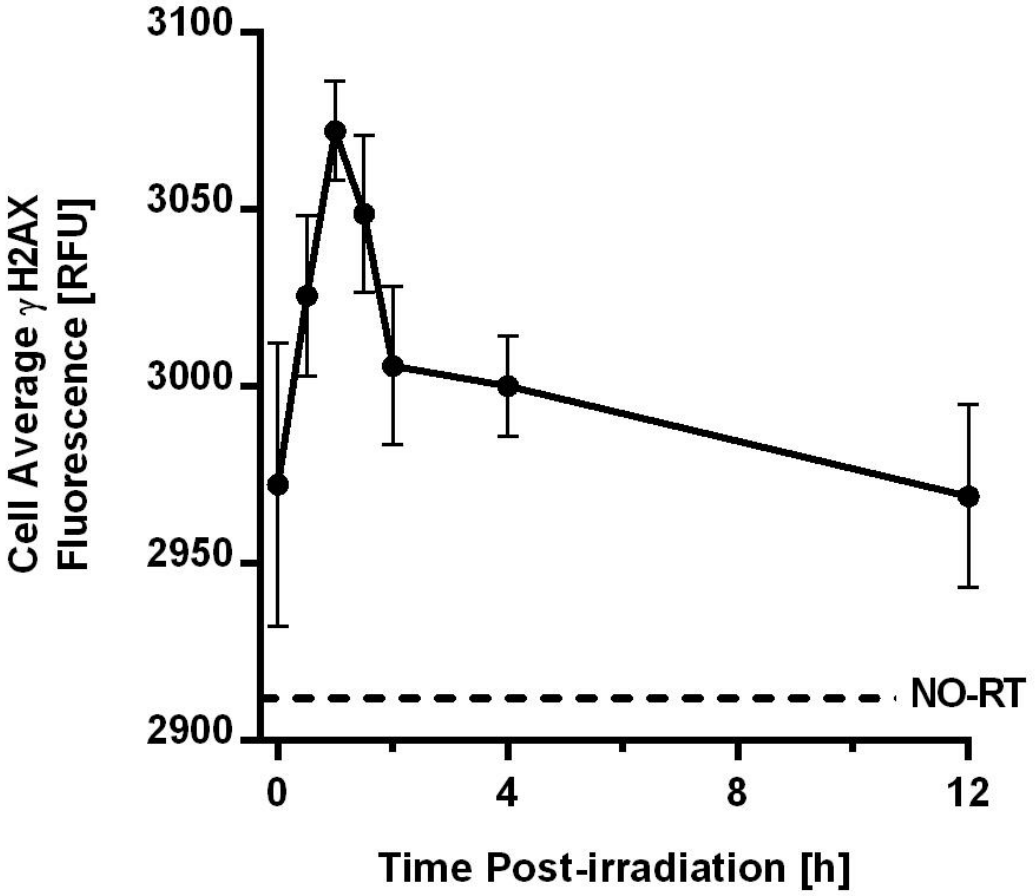

Figure 4.8: To investigate DNA DSB repair kinetics following a 4 Gy irradiation, HeLa cells were fixed at various time points and show an immediate sharp increase in mean cell average γH2AX fluorescence as a response to DNA DSB induction with a gradual decrease correlating with DNA DSB resolution. Mean cell average γH2AX fluorescence of un-irradiated (No-RT) HeLa cells is shown as dashed line.

4.2 Biological validation of irradiator system

One of the initial effects of ionizing radiation is the generation of reactive oxygen species due to photons interacting with molecules inside the cell (e.g. H_2O). We assessed the relative change in production of intracellular ROS using a fluorescent assay well suited to high-throughput screening. To assess the intracellular reactive oxygen species produced during irradiation cells were stained with chloromethyl-H_2DCFDA. Chloromethyl-H_2DCFDA freely permeates through live cell membranes and is retained in the cellular interior. During irradiation ROS will cleave a portion of the dye molecule to form a fluorescent adduct that may be quantified as an indicator of intracellular ROS. The detailed procedure is discussed further in section 4.2.1. With increasing radiation dose, a significant increase in ROS as measured by chloromethyl-H_2DCFDA fluorescence was seen, this increase scaled linearly with radiation dose over the range of 0-8 Gy (R^2= 0.9229) as seen in **Figure 4.9**.

DNA damage from both ROS production near DNA and direct ionization can be evaluated through measurement of physical DNA double strand breaks (DSB). DSBs scale linearly with ionizing radiation dose, with an incidence of approximately 20-40 DSBs per Gy of absorbed dose per nucleus from x-rays [21,22]. The DNA DSBs induced by ionizing radiation were assessed through single cell gel electrophoresis (SCGE), more commonly called the "comet assay". During the process of the comet assay cell are imbedded in an agrose gel promptly after irradiation, the cells are lysed (breaking down of cellular membranes to allow full access to the cellular components), electophoresis is performed to pull the negatively charged DNA through the gel, the DNA is stained with a fluorescent dye, and fluorescent

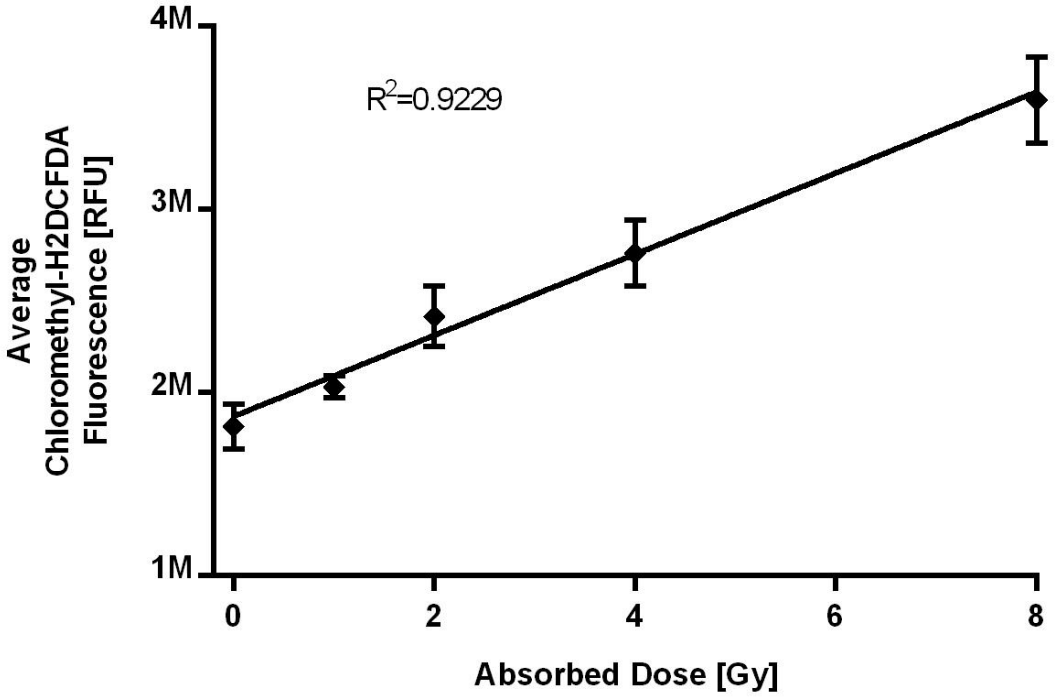

Figure 4.9: Production of reactive oxygen species by ionizing radiation scaling linearly with increasing absorbed dose to the cells (+/- 95% CI).

microscopy is performed. The smaller DNA fragments created by DSBs experience less resistance migrating through the gel and travel farther creating a longer tail. The term comet comes from the resemblance of the DNA migration pattern to a comet tail. The ratio of DNA retained in the "head" of the comet to the "tail" reflects the number of DNA DSBs present in the cell and can be quantified. The detailed procedure is discussed further in section 4.2.2. The measurement of physical DNA DSBs created by ionizing radiation was achieved by performing single cell gel electrophoresis (a.k.a "comet assay") where the DNA fragments will be pulled out of the cell. The small DNA fragments produced via irradiation travel farther through the agrose gel forming a longer comet tail, the comet assay was quantified using the Olive Tail Moment (OTM) [75]. Again, cells were irradiated with a range of radiation doses across a single 96 well plate. In this manner, a large number of comets were analyzed per dose point (**Table 4.2**) improving the statistical power of results. The average OTM of the samples increased linearly with radiation dose (R^2=0.9906) as seen in **Figure 4.10** with representative microscopy images shown in **Figure 4.11**.

Table 4.2: Number of comets assayed per dose-point.

Absorbed Dose [Gy]	# Comets Counted
0	434
1	372
2	177
4	194
8	273

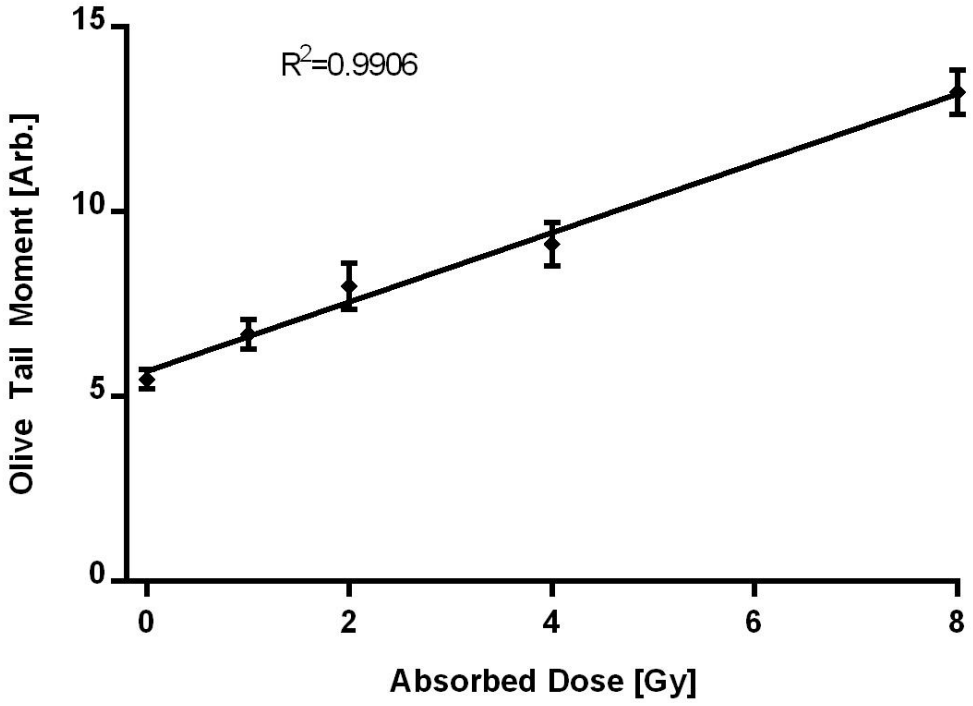

Figure 4.10: Production of physical DNA double strand breaks by ionizing radiation scaling linearly with increasing absorbed dose to the cells (+/- 95% CI).

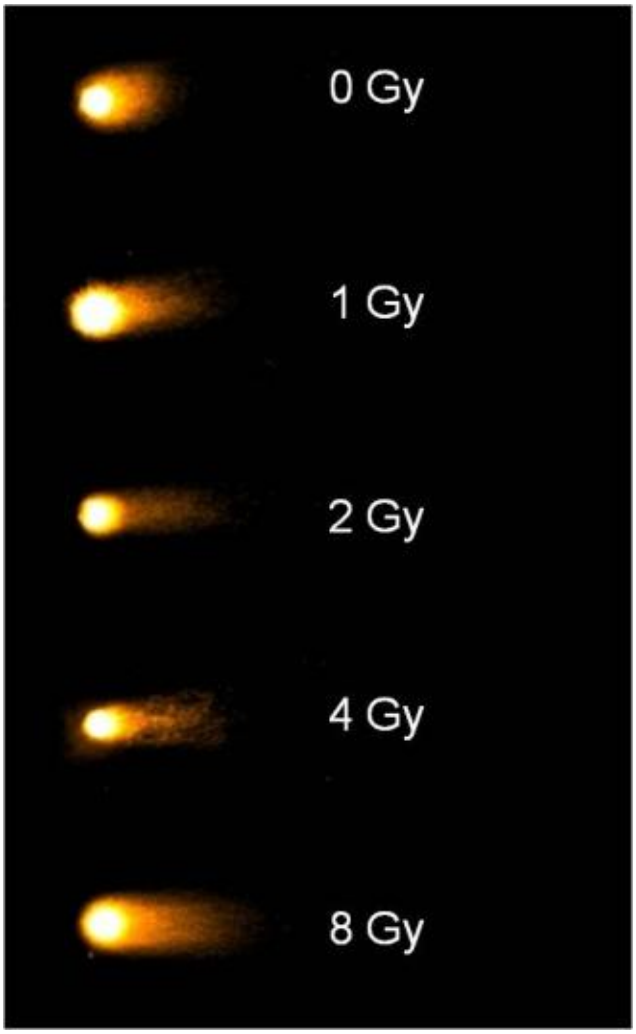

Figure 4.11: Representative microscopy images of comets at doses 0-8 Gy showing increasing tail length with higher doses.

Finally, following the induction of DNA strand breaks, the DNA repair machinery identifies the break sites and activates a complex sequence of events with the goal of repairing the induced DNA damage. One of the early steps in this process is phosphorylation of the histone H2AX at serine 139 (i.e. γH2AX), an event that can be identified using immunofluorescence. DNA DSBs occur naturally as part of normal cell development, are induced by ionizing radiation, or can be generated by chemotherapeutic agents.

DSBs scale linearly with ionizing radiation dose, with an incidence of approximately 20-40 DSBs per Gy of absorbed dose per nucleus from x-rays [21,22]. The creation of a DSB promptly initiates the phosphorylation of histone H2AX at Serine 139 (γH2AX) as a first responder in the cellular DNA DSB repair pathway [22-24]. Resolution of DSBs correlates with dephosphorylation of γH2AX. Typically this process is analyzed by counting foci via immunofluorescence microscopy, by assessing levels of γH2AX by western blot, or by determining the level of γH2AX by flow cytometry [77]. All of these methods are both labor and time intensive and can have significant costs associated with them. Additionally, manual foci counting is susceptible to a subjective foci selection bias. Because of these complications a novel approach was developed that provides an expedient, high-throughput, objective and cost-effective method for γH2AX analysis using image cytometry. After irradiation γH2AX is labeled with a fluorescent marker using antibodies specific to γH2AX , the cell average γH2AX fluorescence can be quantified through automated analysis of microscopy images taken by the image cytometer. The detailed procedure is discussed further in section 4.2.3. As seen in Figure 3, the cell average γH2AX fluorescence increases linearly with increasing absorbed dose (R^2=0.9995) shown in **Figure 4.12** with representative microscopy images shown in **Figure 4.13**.

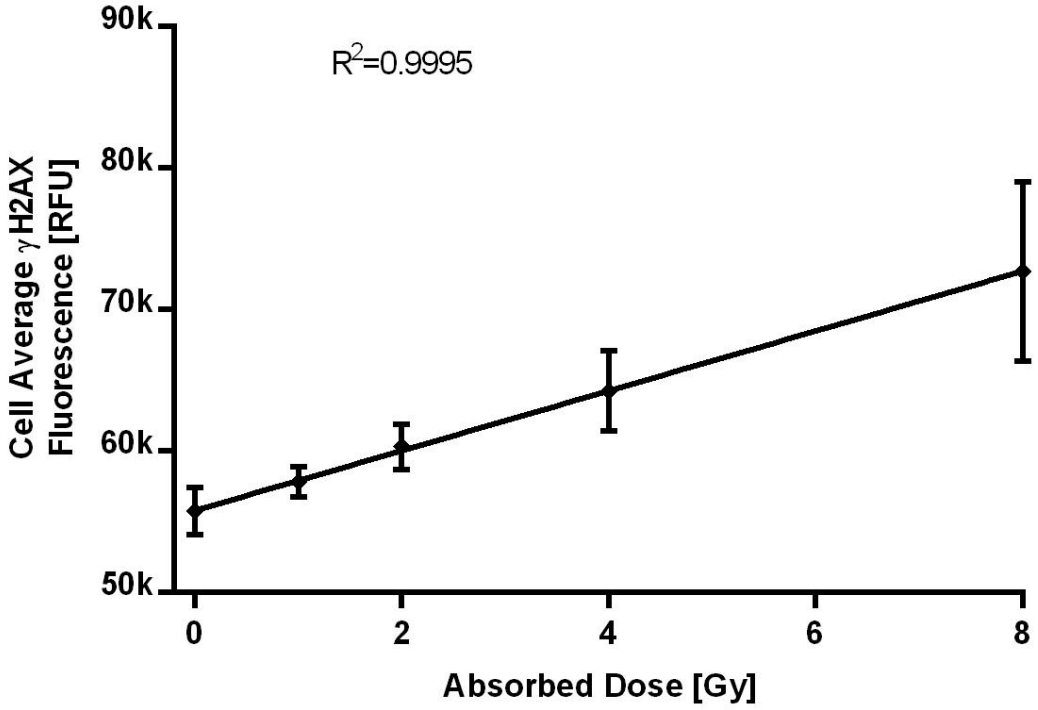

Figure 4.12: Phosphorylation of histone 2AX, activating the DNA double strand break repair pathways, by ionizing radiation scaling linearly with increasing absorbed dose to the cells (+/- 95% CI).

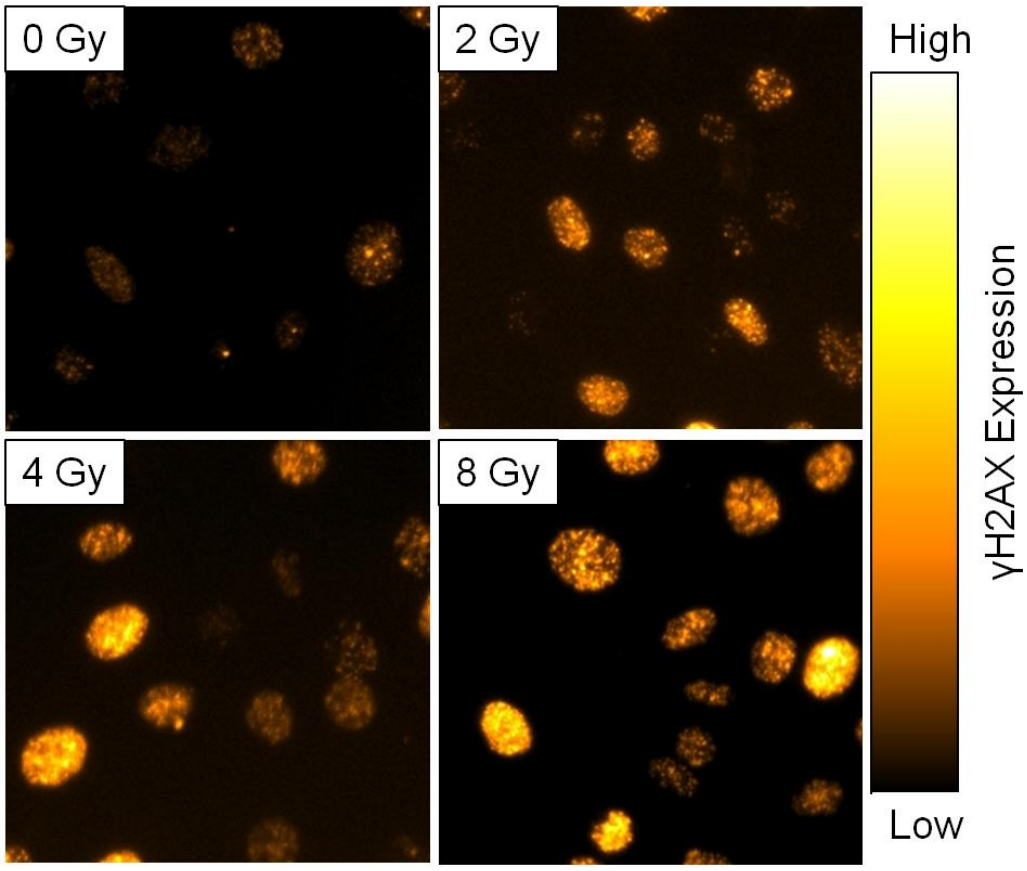

Figure 4.13: Representative immunofluorescent microscopy images of increasing γH2AX foci at several dose points.

4.3 Summary

To ensure accurate and precise bioassay results, the design of any high throughput technology for *in vitro* biology research must limit the impact of mechanical and environmental stresses on the cells being tested. Therefore, in order to evaluate the overall robustness of an irradiator, biological validation should be performed using assays with well-characterized dose-response relationships. In this work, a cascade of three distinct events associated with the early effects of DNA damage that are known to be linearly related to absorbed dose were examined as a validation and demonstration of the robustness of this high throughput irradiator system [21,22]. The production of intracellular reactive oxygen species (chloromethyl-H_2DCFDA dye), the formation of DNA strand breaks (comet assay), and the initiation of DNA repair (γH2AX) all scaled in a highly linear fashion with increasing radiation dose. A similar, less extensive, biological validation of a micro-beam cellular irradiator using only γH2AX dephosphorylation has previously been presented by Bordelon et al. [3].

By evaluation of intracellular reactive oxygen species production, physical DNA double strand breaks, and phosphorylation of histone H2AX we have shown negligible perturbation being introduced by our system during the irradiation cycle. These additional testing metrics provide confidence that not only can the dosimetry be confirmed through standard physics testing such as Monte Carlo simulation and thermo-luminescent dosimeter evaluation but also produce the desired dose effects *in vitro*. It is our belief that this is a critical validation process that should be strongly considered in the commissioning of any biological research irradiator.

Chapter 5

Application in head & neck cancer

5.1 Investigation of the cellular autophagic response to ionizing radiation

The culmination of this investigation was the creation of an irradiator that is dosimetrically superior to traditional cellular irradiation methods that also leverages the recent advances in biological assay techniques and high-throughput instrumentation. The final phase of this project was to implement the irradiator system to study a translational cancer research problem. The cellular process of autophagy has shown promise as a potential novel target in cancer therapy both in the context of radiation and chemotherapy treatment. Meaning "self eating", autophagy is a genetically programmed, evolutionarily conserved process whereby cellular proteins, organelles, and cytoplasm are engulfed, digested, and recycled in response to cellular stress to aid in cell survival [25]. However, autophagy can also promote cell death through excessive self-digestion and degradation of cellular contents [26]. Further understanding of this pro-survival/death balance is needed to exploit this adaptive process for improved patient

therapeutic response [78]. Several groups have shown that autophagic acidic compartments are formed in response to damage initiated by ionizing radiation in a variety of cancer cell types ranging from breast, pharyngeal, cervical, lung, to brain cancers [31-35]. However, the exact mechanism by which ionizing radiation induces autophagy remains unclear. To further elucidate this mechanism it is necessary to first understand the characteristics of the autophagic response in normal cells exposed to ionizing radiation.

5.2 Autophagic flux methodology

Autophagy is a highly dynamic process making it insufficient to examine a single time-point, rather the total flux of the process must be examined for proper interpretation of autophagy. To assess autophagic flux an inhibitor may be used to prevent turnover of the autophagosomes and measure their time-dependant accumulation, by comparison of inhibited and non-inhibited samples total flux was measured. One ATG protein, ATG8 (commonly called LC3B, microtubule-associated protein 1 light chain 3), is used exclusively in the formation of the phagophore and autophagosome. LC3B has two isoforms within the cell, LC3B-I and LC3B-II. When autophagy is induced LC3B-I, found in the cytoplasm of the cell, is lipidated by phosphatidylethanolamine (PE) to become LC3B-II. Because of the exclusivity of this protein in the formation of the autophagic bodies it is the most common target for assessing autophagic flux [30]. In this investigation autophagic flux was assessed by the techniques of western blot, flow cytometry, and fluorescent microscopy. In the technique of western blot cellular protein expression is examined by extracting cellular proteins, performing electrophoresis on the proteins through a gel to separate the proteins by molecular weight, transferring the proteins to a membrane for probing with fluorescently tagged antibodies specific to the proteins of interest.

5.2.1 Cell culture

All experiments in the biological validation were performed using TERT immortalized human tonsillar epithelial (HTE) cells. Cells were cultured in serum free media at 37°C with 5% CO_2 as we have previously described (Kimple et al. [59]). Careful consideration was given to cell feeding schedules prior to bioassay to ensure autophagy was not induced due to cellular nutrient depletion. Nutrient deprived cells were used as a positive control for autophagic flux, this was achieved by withholding bovine pituitary extract (BPE) and epidermal growth factor (EGF) from the media mixture.

5.2.2 Autophagic flux inhibitor

Bafilomycin A1 is a toxic macrolide antibiotic derived from the bacteria *Streptomyces griseus*. Bafilomycin A1 is a commonly used autophagic flux inhibitor that works by preventing fusion of the lysosome to the autophagosome preventing the maturation of the autolysosome, thereby preventing autophagic turnover [79]. For all autophagic flux assay techniques used in this investigation the inhibited cells were treated with 0.1 μM Bafilomycin A1for 8 hours at 37 °C with 5% CO_2 while non-inhibited cells were given a dimethyl sulfoxide (DMSO) vehicle control for the same period.

5.2.3 Western blot

Cells were grown to approximately 90% confluence prior to assay. Whole cell protein lysate was obtained through lysis with RIPA buffer (50 mM HEPES, pH 7.4, 150 mM NaCl,.1% Tween-20, 10% glycerol, 2.5 mM EGTA, 1 mM EDTA, 1 mM DTT, 1 mM Na_3VO_4, 1 mM PMSF, 1 mM BGP, and 10 ug/ml of leupeptin and aprotinin). Cells were scraped, samples sonicated for 10 seconds, and allowed to rotate for 1 hour at 4 °C. Samples were centrifuged at

14000 RPM for 10 minutes and supernatant retained as sample for analysis. Protein levels of the lysates were quantified by Bradford assay (#500-0006, Bio-Rad Laboritories, Hercules, CA, USA). Samples were prepared using equal amounts of protein (~ 75 µg), 2.5 µL Novex NuPAGE LDS sample buffer (#NP0007, Life Technologies, Calsbad, CA, USA), and de-ionized water to a total loading volume of 20 µL.

Protein was separated by molecular weight via polyacrylimide gel electrophoresis (PAGE) in Novex NuPAGE 12% Bis-Tris Gels (#NP0342, Life Technologies, Carlsbad, CA, USA) with SeeBlue Plus2 Prestained Standard (#LC5925, Invitrogen Inc., Carlsbad, CA, USA) molecular weight marker. Electrophoresis was performed in Novex NuPAGE MES SDS running buffer (#NP0002, Life Technologies, Carlsbad, CA, USA) at a constant 200 V for approximately 75 minutes to gain good separation of isoforms LC3B-I and LC3B-II. Following electrophoresis protein was transferred to a polyvinylidene fluoride (PVDF) Immobilon-FL membrane (#IPFL00010, Millipore Corp., Billerica, MA, USA) in transfer buffer (2.5 mM Tris base, 19.2 mM glycine, pH 8.3) at a constant 100 V for 30 minutes at 4 °C. Non-specific binding of antibodies to the PVDF membrane was performed in blocking buffer (5% bovine serum albumin (BSA) and 0.2% sodium azide) for one hour at room temperature under gentle rocking.

The PVDF membrane was submerged in a primary antibody mixture of 1:1,000 LC3A/B anti-rabbit (#4108, Cell Signaling Technology, Inc., Danvers, MA, USA) and 1:2,000 β-actin (8H10D10) anti-mouse (#3700, Cell Signaling Technology, Inc., Danvers, MA, USA) in buffer (5% BSA, 0.1% sodium azide, and 0.2% Tween-20) overnight with gentle rocking at 4 °C [80,81]. Primary antibody was removed from the membranes and washed five times in PBS-T (phosphate buffered saline, pH 7.4, 0.1% Tween-20) with vigorous rocking for five minutes each wash to remove residual primary antibody. The washed membrane was then submerged in a secondary antibody mixture of 1:25,000 IRDye 800CW Goat anti-rabbit IgG (H + L) (#926-

32211, LI-COR, Inc., Lincoln, NE, USA) and 1:25,000 IRDye 680RD Goat anti-mouse IgG (H + L) (#926-68070, LI-COR, Inc., Lincoln, NE, USA) in buffer (5% BSA, 0.1% sodium azide, 0.2% Tween-20, and 0.01% SDS) for one hour at room temperature under gentle rocking while protected from light exposure. Secondary antibody was removed from the membranes and washed five times in PBS-T with vigorous rocking for five minutes each wash to remove residual secondary antibody and a final wash in PBS to remove residual Tween-20 detergent. Membranes were allowed to dry prior to analysis.

Analysis was performed on a LI-COR Odyssey Fc Dual-Mode imager with Image Studio Software (LI-COR, Inc., Lincoln, NE, USA). A 30 second 680 nm color channel integration was used to detect the β-actin protein level loading control while a 2 minute 800 nm color channel integration was used to detect LC3B. LC3B-II protein isoform bands were quantified using a median background signal subtraction with normalization to the corresponding β-actin band. For each experimental condition the autophagic flux was determined by subtraction of a non-inhibited sample from a sample with autophagic inhibition using bafilomycin-A1 [30]. A representative western blot is shown in **Figure 5.1**. Each treatment condition was then normalized to an experimental control (i.e. No-RT) to measure a fold-change in autophagic flux.

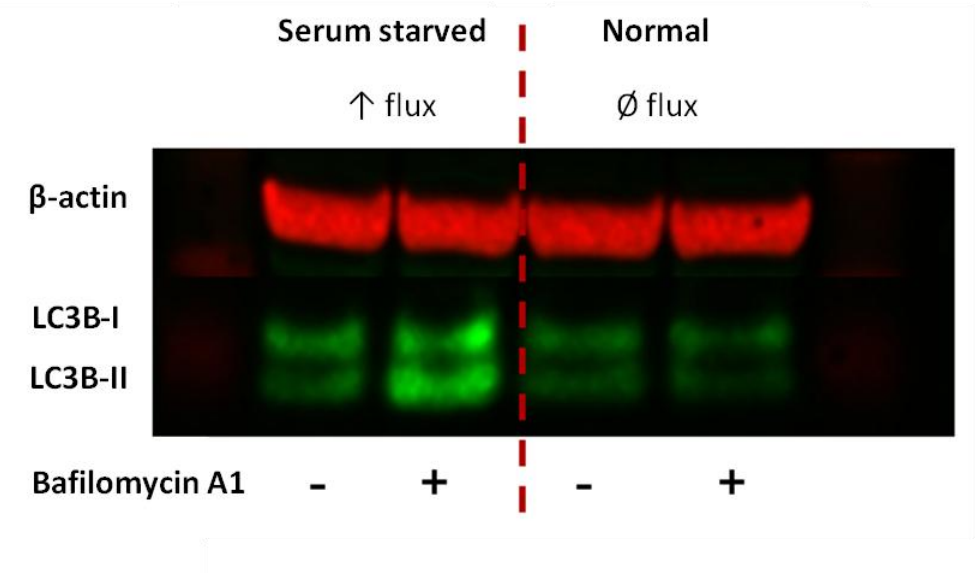

Figure 5.1: Representative western blot showing increased autophagic flux under serum starved conditions while normal cells exhibit negligible flux.

5.2.4 Flow Cytometry

Cells were grown to approximately 90% confluence prior to assay. Trypsin is added to the cells and allowed to incubate at 37 °C for 5 minutes, to release the cells from the cell culture surface, before being transferred to a vial containing PBS and 2% fetal bovine serum to inactivate the trypsin. The samples were centrifuged for 5 minutes at 1,400 RPM and 4 °C to pellet cells, and washed with PBS. Using the FlowCellect Autophagy LC3 Antibody-based kit (#FCCH100171, Millipore Corp., Billerica, MA, USA), 50 μL of reagent B is added to each vial and immediately centrifuged. Reagent B acts to selectively permeabilize the cell so the cytosolic isoform LC3B-I may be washed away whilst leaving the autophagic membrane bound LC3B-II intact within the cell. Reagent B is removed and 50 μL optimized anti-LC3/FITC conjugated antibody from the kit is added, the samples are allowed to incubate for 30 minutes at room temperature while protected from light. Following antibody labeling the samples are centrifuged and washed in an assay buffer included with the kit to remove any residual antibody. Cells are resuspended in 100 μL assay buffer for flow cytometry analysis. Analysis of the sample was performed on a FACSCalibur Flow Cytometer (BD Biosciences, San Jose, CA, USA) where 30,000 cells were assayed per sample using a FITC laser. For each experimental condition the autophagic flux was determined by subtraction of the median fluorescent intensities of non-inhibited samples from samples with autophagic inhibition using bafilomycin-A1 [30]. A representative set of flow cytometry samples is shown in **Figure 5.2**. Each treatment condition was then normalized to the experimental control to measure a fold-change in autophagic flux.

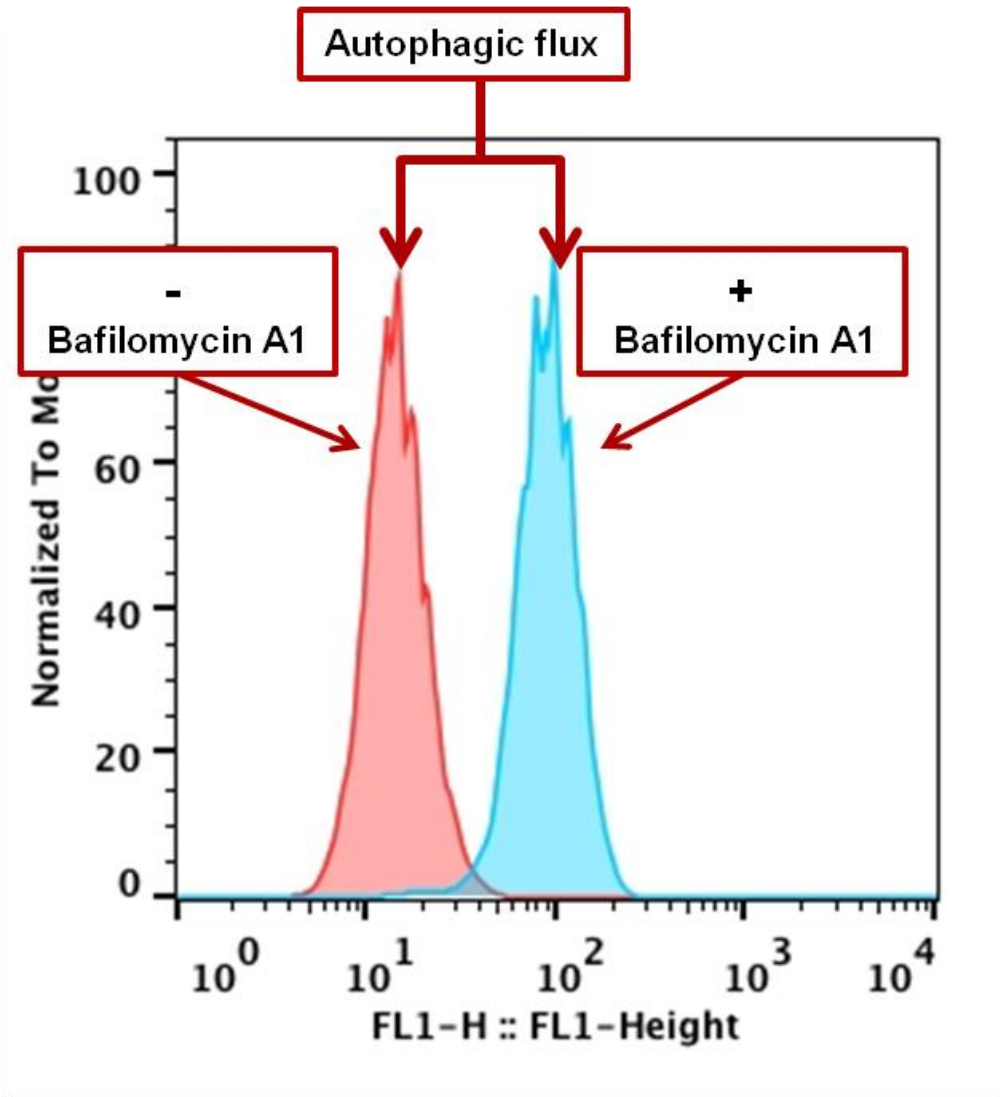

Figure 5.2: Representative flow cytometry samples indicating active autophagic flux.

5.2.5 Fluorescent microscopy

A tandem fluorescent plasmid, mTagRFP-mWasabi-LC3, was used to monitor autophagic maturation through fluorescent microscopy [82]. Reporter plasmids are fragments of circular double-stranded DNA that can replicate independently of chromosomal DNA, when introduced to a cell by transfection the plasmid alters the gene of interest to produce the corresponding protein with a fluorescent tag that can be visualized through microscopy. In this context the plasmid mTagRFP-mWasabi-LC3 instructs the LC3B gene to produce the red fluorophore mTagRFP and green mWasabi. The function of this assay in based on the different acid dissociation constants, pK_a, of these fluorophores as seen in **Table 5.1**.

Table 5.1: Properties of plasmid fluorescent proteins.

Protein	**Excitation [nm]**	**Emission [nm]**	**Relative Brightness**	**Extinction Coefficient [$/10^{-3}M^{-1}cm^{-1}$]**	**Quantum Yield**	**pK_a**
mTagRFP	555	584	134	92[a]	0.48	< 4.0
mWasabi	493	509	167	70[b]	0.8	6.5

[a] Relative brightness, % of DsRed2; [b] Relative brightness, % of EGFP

The significant difference in pK_a means that in low pH the mWasabi fluorophore will be quenched while the mTagRFP will remain active. This can be exploited to examine both the induction and maturation of the autophagic process, as illustrated in **Figure 5.3**, by analysis of merged color channel images of cells.

Cells were grown to approximately 90% confluence prior to transfection with the plasmid. Transfection was performed using the cell penetrating peptide Xfect Protein Transfection Reagent (#631324, Clontech Laboratories, Inc., Mountain View, CA, USA). The transfection agent forms nanoparticle complexes around the plasmid DNA that allows it to enter

the cell and integrate into the cellular DNA. The following protocol volumes listed are per sample in a 6-well cell culture plate. In a microcentrifuge vial 5 µg of the plasmid DNA is mixed with the

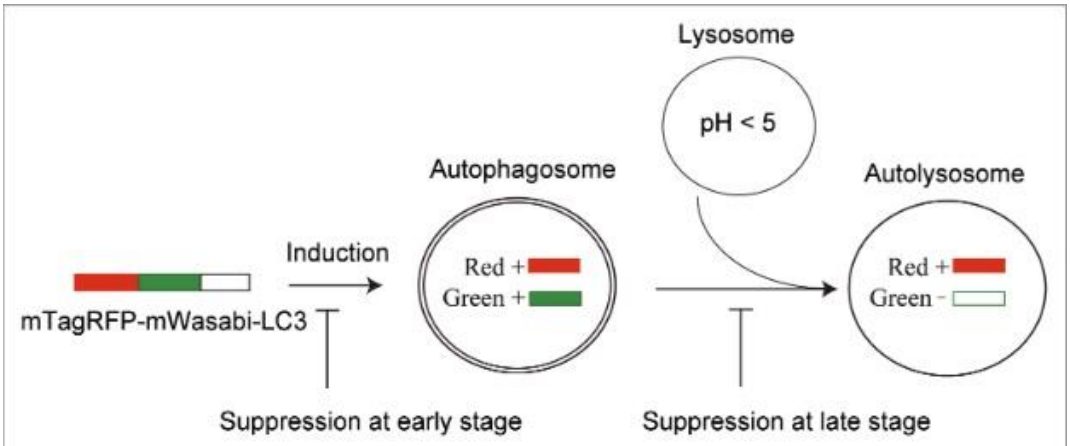

Fluorescent signals of puncta	Typical results of autophagic flux			
	Basal level	Induction	Suppression at early stage	Suppression at late stage
Red+ Green+	—	increase	decrease	increase
Red+ Green−	—	increase	decrease	decrease

Figure 5.3: Rationale of mTagRFP-mWasabi-LC3 reporter for monitoring autophagic flux. Monitoring the tandem fluorescent-tagged LC3 fluorescence allows distinguishing autophagosome, autolysosome and monitoring different stages of autophagic flux. At early stage of autophagosomes biogenesis, puncta of mTagRFP-mWasabi–LC3 accumulate and display both green and red fluorescent signals ($GFP^{+}RFP^{+}$). At late stage of the autophagic process (the fusion of autophagosome and lysosome, autolysosomes), the green signals of mWasabi are quenched in acidic autolysosomes, while the red signals of mTagRFP are retained ($GFP^{-}RFP^{+}$) [82].

Xfect reaction buffer to a final volume of 100 μL and vortexed. A volume of 1.5 μL of the Xfect ploymer in added and vortexed for 10 seconds and allowed to incubate the nanoparticle complexes for 10 minutes at room temperature. The nanoparticle mixture is added to the cells with a volume of 1 mL media. For the transfection penicillin and streptomycin (Pen/Strep) were omitted from the media to increase transfection efficiency. Cells were allowed to transfect for 4 hours at 37 °C and 5% CO_2. After incubation the cells were washed with PBS and media changed (- Pen/Strep), cells were placed back into the incubator and allowed to recover for approximately 24 hours. Typically full plasmid expression is achieved 24-28 hours after transfection and experimental conditions may be applied to the samples.

Images to the samples were performed on an Olympus BX41 fluorescent inverted microscope (Olympus Corp., Shinjuko, Tokyo, Japan) using a 40X objective with FITC and RFP images acquired. Imaged are processed using FIJI (FIJI Is Just ImageJ) (NIH, Bathesda, MD, USA) [62,83]. Images were co-registered using the FIJI plugin StackReg [63]. Colocalization analysis was performed with the FJI plugin Coloc2 developed by Daniel J White, Tom Kazimiers, and Johannes Schindelin. Respresentative images are shown in **Figure 5.4**.

(a)

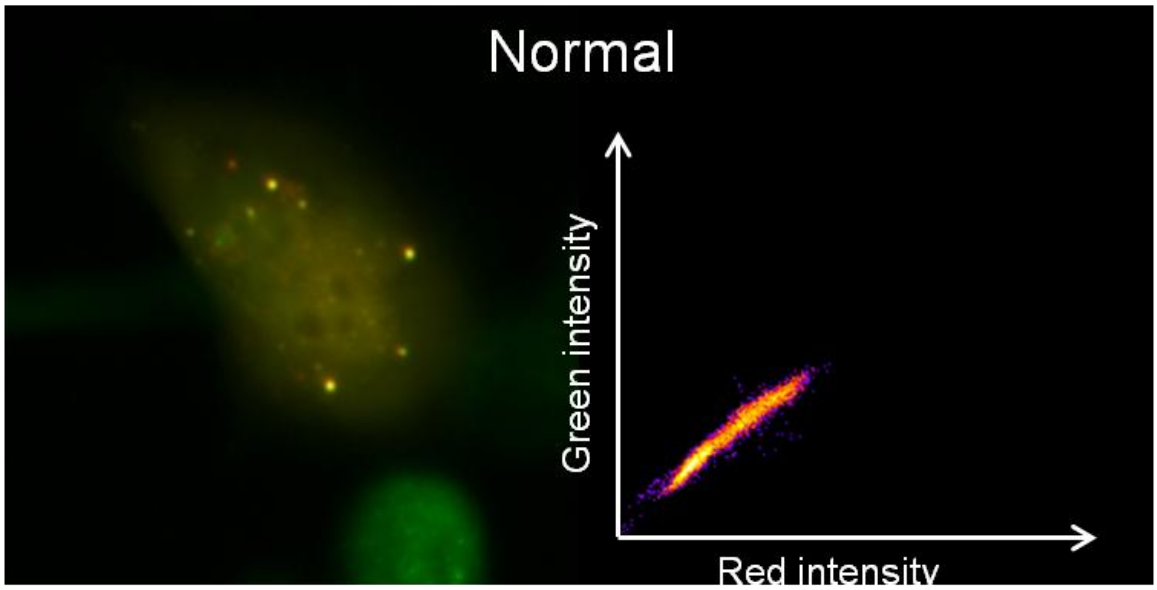

(b)

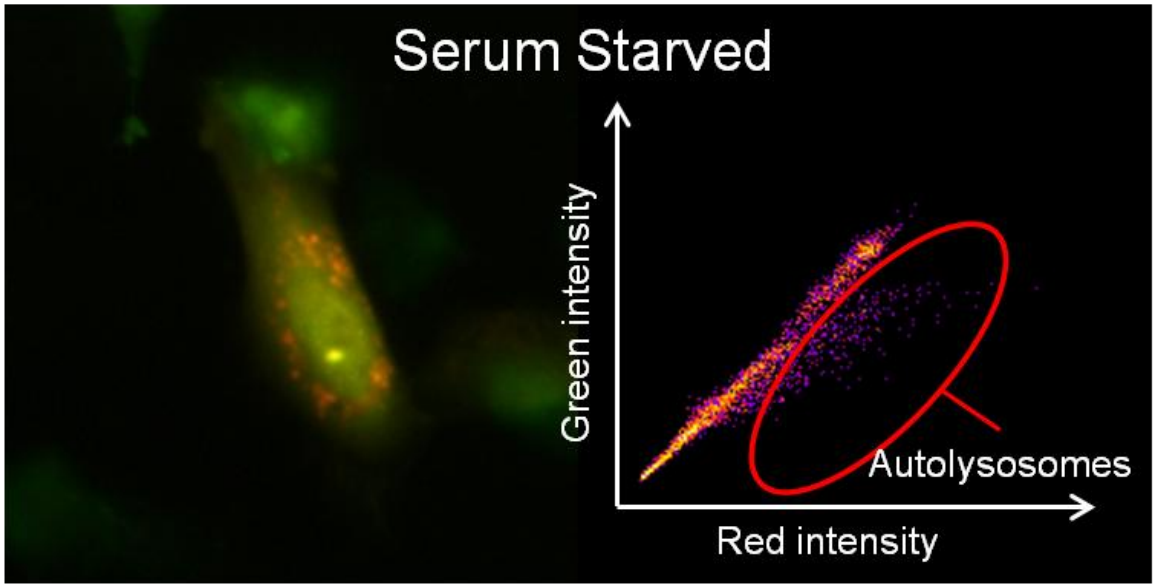

Figure 5.4: (a) Normal cells display high colocalization of red and green channels, while (b) serum starved cells exhibit significant quenching of the green fluorophores indicating the formation of functionally intact autolysosomes (red puncta).

5.3 Characteristics of ionizing radiation induced autophagy

To investigate the response of normal oral kerotinocytes to ionizing radiation the influence of three radiation delivery characteristics were investigated: the time-dependant induction of autophagy following irradiation, the influence of radiation dose escalation to the autophagic adaptive response, and modulation of autophagy by rate of radiation delivery.

5.3.1 Time-dependant induction of autophagic flux following irradiation

Following a dose of 4 Gy HTE cells undergo a gradual sigmoid induction of autophagy starting at approximately 2 hours post-irradiation that approaches a steady-state at approximately 12 hours as seen in **Figure 5.5** by western blot analysis. This finding is further reinforced via flow cytometry analysis that reveals this plateau of autophagic activity remains consistent with a 40% increase over non-irradiated samples that stable to at least 48 hours as seen in **Figure 5.6**. Based on this analysis all further investigation of the autophagic response was performed at 24 hours post-irradiation to ensure steady-state autophagic flux.

5.3.2 Influence of radiation dose escalation to the autophagic adaptive response

The radiation dose delivered to the HTE cells was escalated between 0-8 Gy and autophagic flux assed at 24 hours post-irradiation. As seen in **Figure 5.7** the autophagic response increases with increasing absorbed dose with a general linear-quadratic behavior (R^2 = 0.923). The accumulation of autolysosomes correlates with increased dose as seen in **Figure 5.8**.

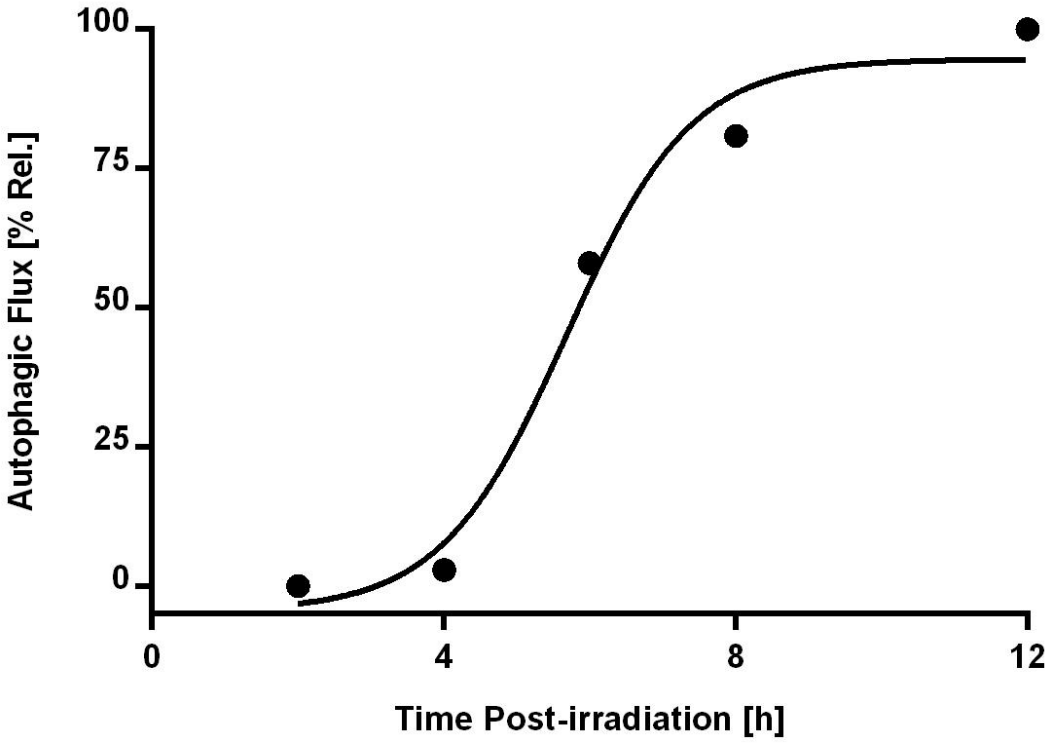

Figure 5.5: Sigmoid induction of autophagic flux following exposure to ionizing radiation (4 Gy) by western blot analysis.

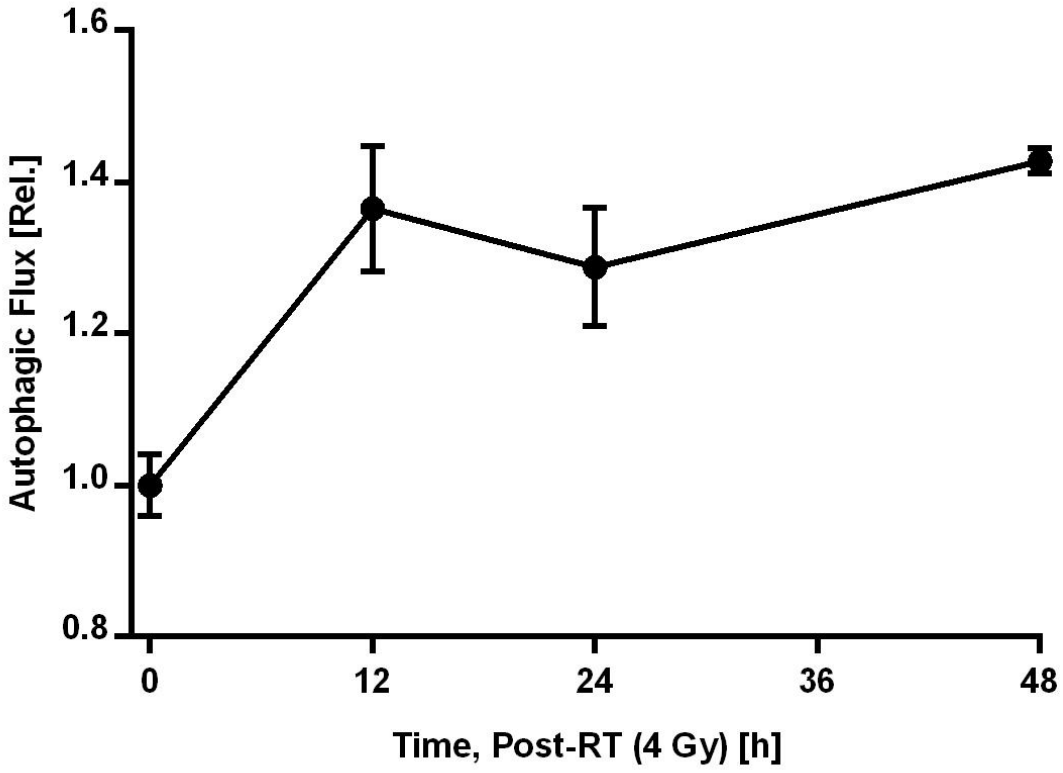

Figure 5.6: A stable steady-state autophagic response is observed 12-48 hours post-irradiation (4 Gy) by flow cytometry analysis.

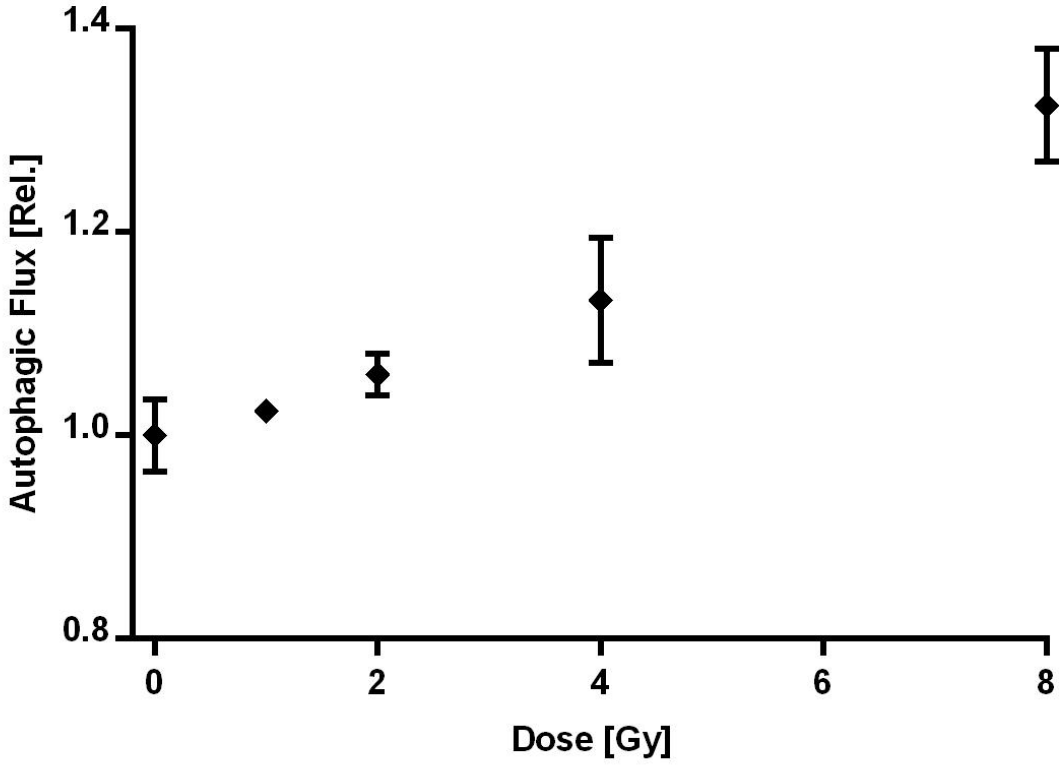

Figure 5.7: Autophagy is increasingly induced with escalating ionizing radiation dose.

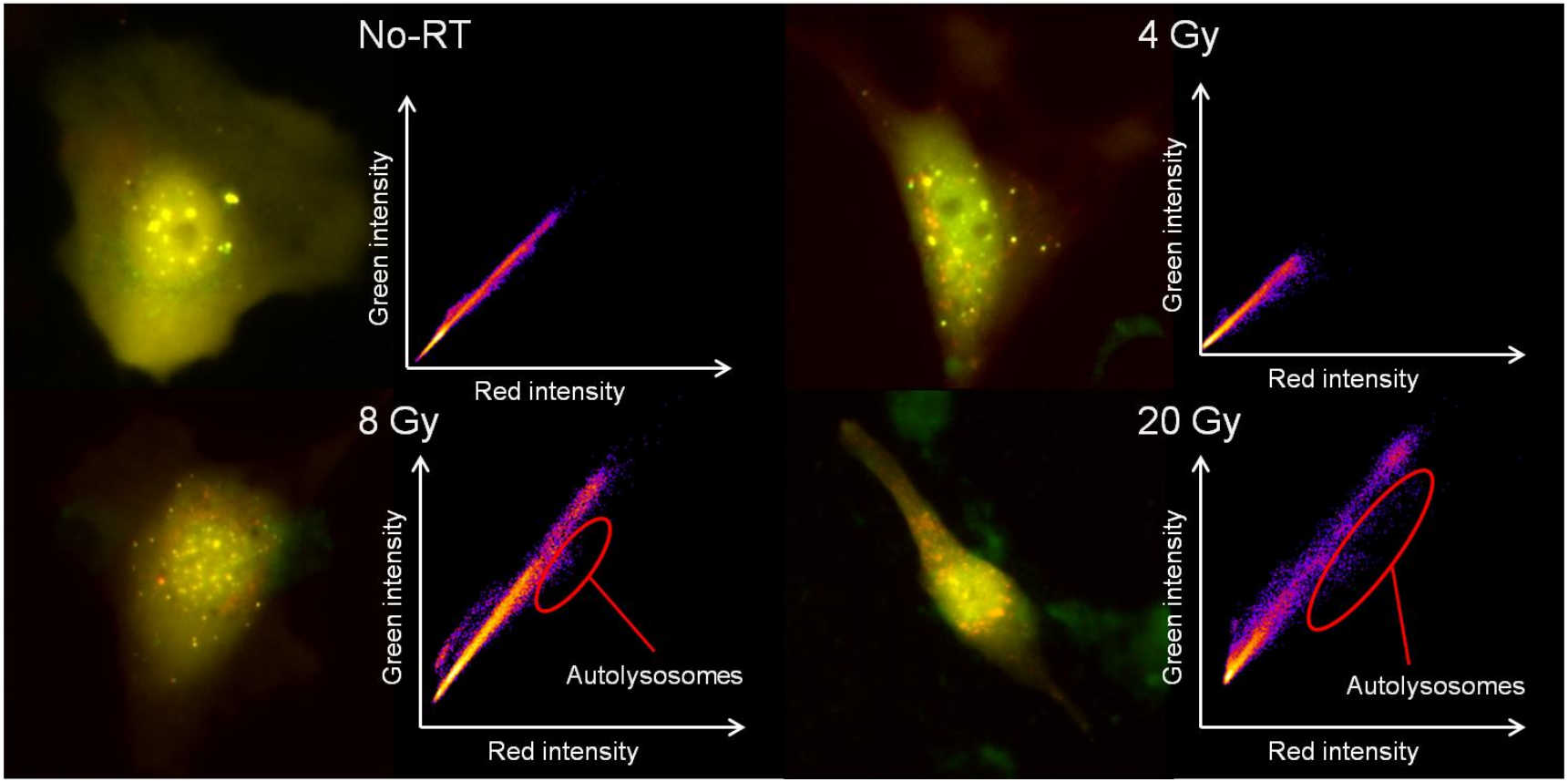

Figure 5.8: Using a tandem labeled LC3 plasmid, autolysosomes are seen to accumulate with escalating ionizing radiation dose.

5.3.3 Dose-rate escalation

Using the irradiator systems ability to modulate dose rate by adjusting the beam current the effect of dose rate of the autophagic process was investigated. Cells were irradiated to a total absorbed dose of 4 Gy using a dose rate of 8.17 cGy/min and 81.7 cGy/min, the dose-rate extremes allowed by the irradiator system. As seen in **Figure 5.9** no statistically significant difference exists across one decade of dose-rate modulation. In an effort to observe a dose-rate effect the cells were irradiated using the UW-MRRC linac with a 6 MV beam quality. Cell culture dishes were irradiated in an inverted geometry with a build-up layer of 5 cm PMMA to place the cellular layer in the flatter region of the beam PDD. Measurements were performed using a 0.6 cc Farmer-type chamber to account for the attenuation of the carbon fiber patient couch, total attenuation was determined to be 2.2%. Shown in **Figure 5.10** a total dose of 4 Gy was delivered to the cells at dose-rates between 100 - 600 cGy/min. Interestingly the largest autophagic response was measured at a dose-rate of 300 cGy/min.

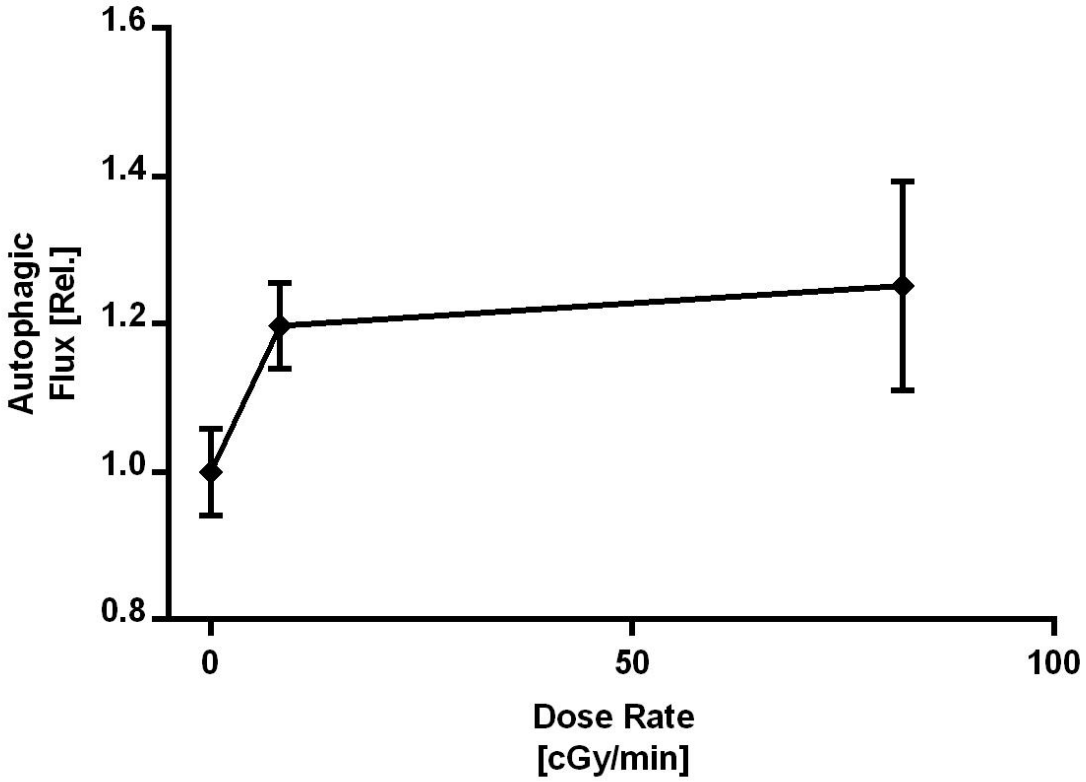

Figure 5.9: Using the irradiator system only minor changes in the autophagic response were observed at 8.17 cGy/min and 81.7 cGy/min.

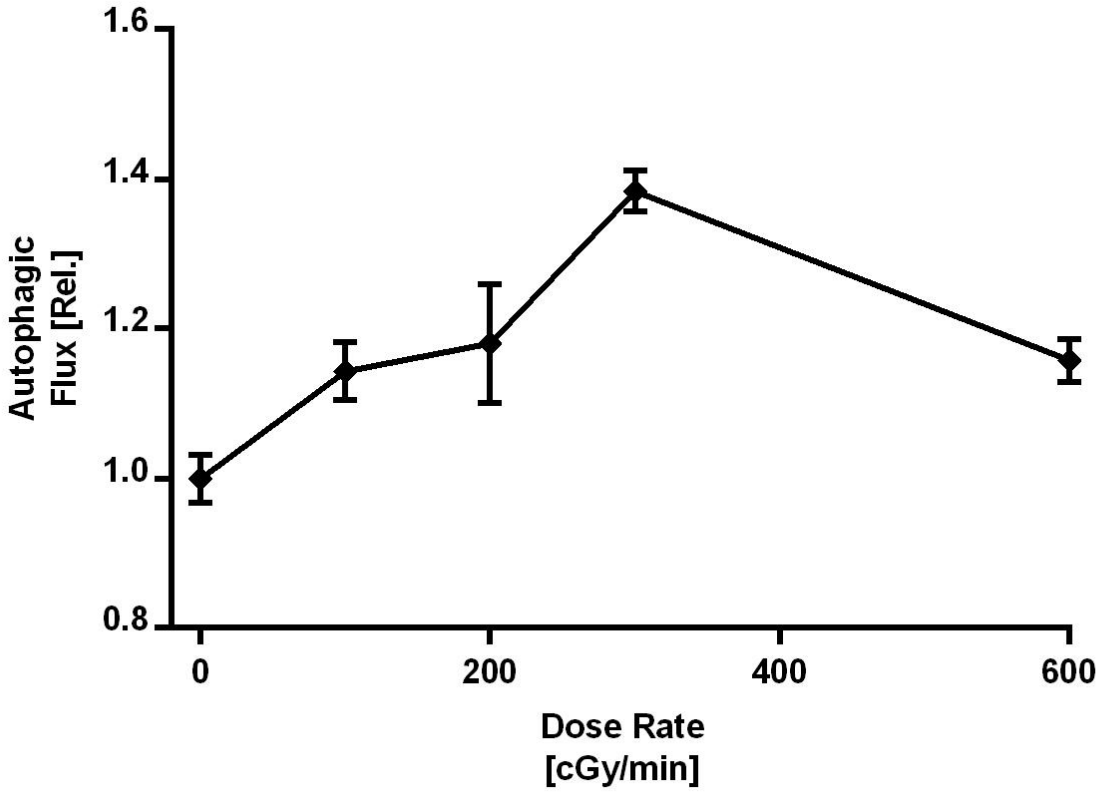

Figure 5.10: Using the dose-rates provided by a linac operating at 6 MV a maximal autophagy response is seen at a dose-rate of 300 cGy/min.

5.4 Interplay of HPV viral oncogenes and autophagy

Human Papillomavirus (HPV) causes HNC in a growing subset of patients, many of whom have no traditional risk factors [39,40]. HPV-positive cancers are now thought to account for 30-65% of all HNC and 50-80% of cancers arising in the oropharynx [40,41]. HPV positive (HPV+) HNC represents a growing public health concern, and is likely to become the predominant cause of HNC over the coming decade [42]. This subset of patients, despite HPV+ HNCs increased metastatic potential, experience improved outcomes compared to HPV- HNC. The HPV viral genome imparts radiation sensitivity to these tumors, having elucidated the normal cellular activation of the autophagic response to ionizing radiation this knowledge was applied to a investigate the interplay of autophagy and HPV viral oncogenes. In mutants of the HTE cell line the vector LXSN introduces and activates the HPV viral oncogenes E6 and E7, significant differences in radiation sensitivity were observed as seen in **Figure 5.11**. Using these mutants autophagic flux flow cytometry was performed 24 hours following irradiation using absorbed doses of 4 and 8 Gy. As shown in **Figure 5.12-13** significant autophagic impairment is imparted by HPV viral oncogene E6.

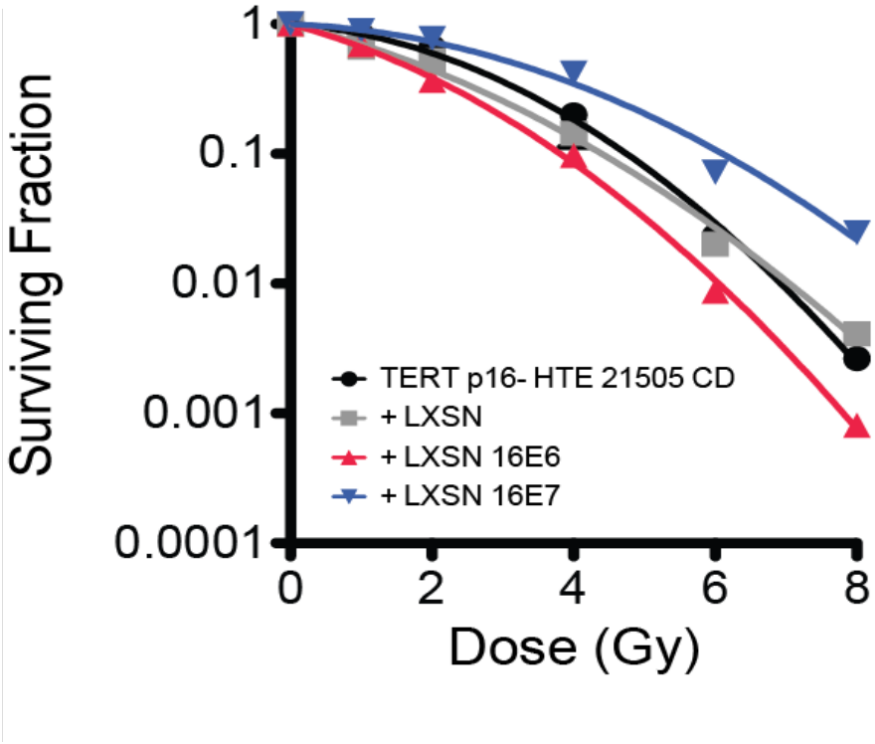

Figure 5.11: HPV-16 viral oncogene E6 imparts radiation sensitivity while viral oncogene E7 mutants exhibit radiation resistance.

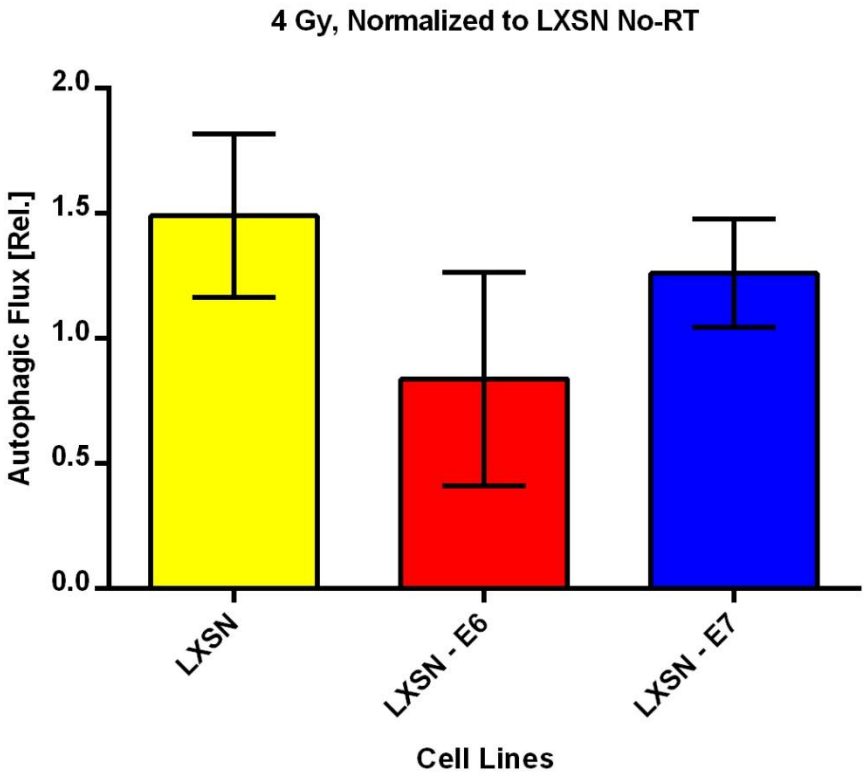

Figure 5.12: HPV-16 viral oncogene E6 reduces the autophagic response to a 4 Gy dose of ionizing radiation.

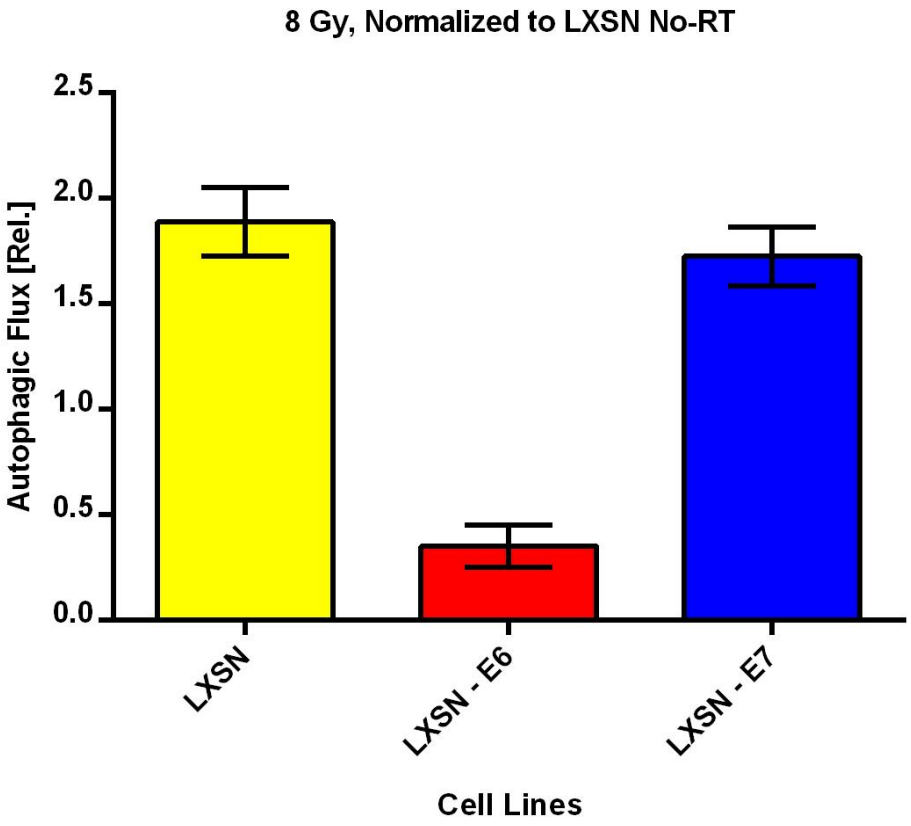

Figure 5.13: HPV-16 viral oncogene E6 significantly reduces the autophagic response to a 8 Gy dose of ionizing radiation.

5.5 Summary

During the investigation of the autophagic response in normal oral kerotinocytes the time dynamics of this process was observed to ensure appropriate bioassay at peak expression. By escalating the delivered dose to cells the autophagic response was seen to correspondingly increase as a pro-survival mechanism. Interestingly the peak autophagic response was observed at a dose-rate of 300 cGy/min. A complimentary finding was observed by Yao et. al. that showed cell survival during the delivery of high-precision radiotherapy was increased when dose-rates were lowered and that this increased survival was attributed to sub-lethal damage repair due to increased autophagy mediated by the ATM/AMPK signaling pathway [84].

These results indicate a rather complex cellular bulk damage sensory mechanism at work leading to activation of the autophagic signaling pathway. The exact process by which ionizing radiation induces autophagy is not known. Clearly many organelles and cellular bulk damage occur during ionizing radiation exposure. It has been suggested that that endoplasmic reticulum (ER, functions to synthesize, fold, and transport proteins) stress, induced by ROS, activates a cytoprotective signaling cascade called the unfolded protein response (UPR). This response involves the ER-localized transmembrane proteins such as protein kinase-like ER kinase (PERK), inositol-requiring enzyme-1 (IRE1), eukaryotic initiation factor 2α (eIF2α), and activating transcription factor-6 (ATF6) [85,86]. In apoptotic deficient (caspase-3/7) cell lines ER stress induces autophagy that is mediated by PERK activation of eIF2α [87,88]. PERK may additionally reduce translation of the inhibitor protein IkBα subsequently activating nuclear factor kappa B (NF-κB) inducing autophagy [89]

Damage to mitochondria and DNA has also been shown to induce autophagy and delay apoptotic programmed death, however this finding remains mechanistically unclear [90]. It is

well know that DNA damage activates p53 as part of a damage repair response and it has recently been observed that p53 can also modulate the autophagic damage response [91-97]. Given that the HPV viral oncogene E6 degrades cellular p53 the reduction of autophagy observed in response to ionizing radiation may possibly be attributed to this interplay. Clearly, the autophagic response to ionizing radiation is quite complex and further investigation is need to elucidate this mechanism for further therapeutic targeting.

Chapter 6

Conclusions and Future Work

6.1 General conclusions

6.1.1 Irradiator system development & characterization

The loss of dosimetric resolution in dose-response experiments is detrimental because new radiation therapy technology and treatment methods generate non-uniform dose distributions that vary widely from patient to patient. Furthermore, important dosimetry and calibration characteristics (i.e. dose build-up region, beam attenuation, and beam scatter) of these irradiators are typically unknown to the end user. This gap in irradiator specificity and user knowledge can result in significant deviation between delivered dose and intended dose that ultimately adversely impacts experimental results.

To that aim during the course of this investigation a novel high-throughput irradiator system was developed. The production of this irradiator system leverages the increased productivity and capability offered by the newest generation of instrumentation used in the radiobiology laboratory while significantly reducing dosimetric uncertainty. Our system was designed from the beginning with the radiobiology researcher in mind to deliver highly uniform, full-well dose to standard cell culture plates. Furthermore, our system incorporates an on-board

ionization chamber for full NIST traceable verification of dosimetry prior to an irradiation cycle capable of both delivering multiple doses and dose-rates within the same cell culture plate.

6.1.2 Biological validation of irradiator system

The design of any high throughput technology for *in vitro* biology research must limit the impact of mechanical and environmental stresses on the cells being tested. Therefore, in order to evaluate the overall robustness of an irradiator, biological validation using assays with well-characterized linear dose-response relationships were performed. To biologically validate this system several assays were used that focused on the early biologic events seen following a dose of ionizing radiation: (1) the production of inter-cellular reactive oxygen species, (2) the production of physical DNA double strand breaks, and (3) early signals of the DNA double-strand break repair pathway.

By evaluation of intracellular reactive oxygen species production, physical DNA double strand breaks, and phosphorylation of histone H2AX we have shown negligible perturbation being introduced by our system during the irradiation cycle. These additional testing metrics provide confidence that not only can the dosimetry be confirmed through standard physics testing such as Monte Carlo simulation and thermo-luminescent dosimeter evaluation but also produce the desired dose effects *in vitro*. It is our belief that this is a critical validation process that should be strongly considered in the commissioning of any biological research irradiator.

6.1.3 Applications in head & neck cancer

The final phase of this project was to implement the irradiator system to study a translational cancer research problem. The cellular process of autophagy has shown promise as a

potential novel target in cancer therapy both in the context of radiation and chemotherapy treatment. Meaning “self eating”, autophagy is a genetically programmed, evolutionarily conserved process whereby cellular proteins, organelles, and cytoplasm are engulfed, digested, and recycled in response to cellular stress to aid in cell survival [25]. However, autophagy can also promote cell death through excessive self-digestion and degradation of cellular contents [26]. Further understanding of this pro-survival/death balance is needed to exploit this adaptive process for improved patient therapeutic response [78]. Several groups have shown that autophagic acidic compartments are formed in response to damage initiated by ionizing radiation in a variety of cancer cell types ranging from breast, pharyngeal, cervical, lung, to brain cancers [31-35]. However, the exact mechanism by which ionizing radiation induces autophagy remains unclear. To further elucidate this mechanism it was necessary to first understand the characteristics of the autophagic response in normal cells exposed to ionizing radiation. Using normal oral kerotinocytes the effect of ionizing radiation was investigated on the time-dependent induction of autophagy, radiation dose effects, and finally dose-rate effects. It is indisputable that the autophagic response to ionizing radiation is quite complex and further investigation is need to elucidate this mechanism for further therapeutic targeting.

6.2 Future work

6.2.1 Irradiator system continued development

To fully implement this irradiator system into radiobiology research it is necessary to reduce the overall size of the system and further development is need to realize a feasible "bench-top" system with expanded capabilities. First and foremost the independent development of a fully characterized inverted geometry source capable of delivering precise homogenous dose with

the capacity of modulating beam spectrum between 20-250 kVp with dose-rates approaching 20 Gy/min would be ideal to broaden the scope of applicability to radiobiology research. By increasing the available energy and dose-rate the irradiator would more faithfully mimic conditions of tumor treatment with a clinical linac. The source should maintain the ability to deliver low dose-rates, on the order of mGy/min, at extended duty cycles to additionally be of use in low dose-rate health physics applications. Collimation of the source to accommodate different cell culture form factors, including round Petri dishes, could be achieved by developing an iris-style tungsten collimator that can precisely target individual cell culture wells. By collimating the radiation field using an iris a round homogenous field could be maintained and allow rapid transition between widely available cell culture form factors. The size of the system may be further reduced by incorporating smaller linear slides in the positioning system while maintaining sub-millimeter spatial precision for individual or multiple well targeting.

The source and positioning system should be housed within a lead shielded cabinet to allow bench-top use while maintaining low operator dose in keeping with the principles of ALARA. The irradiator cabinet shielding must be sufficient to comply with institutional radiation protection policies as well as the International Commission on Radiological Protection (ICRP) occupational worker dose limits. To promote cell health and metabolic integrity the cabinet should be environmentally controlled to maintain proper humidity, temperature, CO_2 concentration, and variable oxygen concentration capability. By integrating environmental controls the temperature may be reduced to lower cellular metabolic activity to aid in studies requiring high temporal accuracy and oxygen concentration modulation may be used to further study the effect of hypoxia on radiation adaptive response.

Additional oversight and recommendations for dosimetrically accurate radiation delivery for radiation biology research are needed. Societies such as the American Association of Physicist

in Medicine (AAPM), American Society for Radiation Oncology (ASTRO), American Association of Cancer Researchers (AACR), and the American Cancer Society (ACS) should form joint commissions to provide recommendations and guidelines for their members to ensure radiobiology research is being conducted with the highest possible degree of scientific rigor.

6.2.2 Autophagy as a therapeutic target

A further mechanistic investigation into how autophagy is induced by ionizing radiation is needed to fully develop this as a pharmaceutical target for therapeutic exploitation. By overcoming cancer cells ability to repair potentially lethal damage through autophagic rescue they may be sensitized to radiation. The Kimple laboratory is currently extending this body of work to investigate cetuximab resistant HNC. Cetuximab targets the epidermal growth factor receptor (EGFR) pathway and in this subset of patients with resistance, frequent mutation is observed in the phosphoinositide 3-kinase/protein kinase B/mamillian target of rapamycin (PI3K/Akt/mTOR) signaling pathways, where mTOR is a central player the activation of the autophagic process [98,99]. Further investigation may reveal a synergistic effect of pan-class PI3K/Akt/mTOR inhibitors in conjunction with radiation therapy by reducing autophagic rescue of cellular damage.

Bibliography

1. Hall EJ, Giaccia AJ (2012) Radiobiology for the radiologist. Philadelphia: Wolters Kluwer Health/Lippincott Williams & Wilkins.

2. Dodd B, Vetter RJ (2009) Replacement of 137Cs irradiators with x-ray irradiators. Health Phys 96: S27-30.

3. Bordelon DE, Zhang J, Graboski S, Cox A, Schreiber E, et al. (2008) A nanotube based electron microbeam cellular irradiator for radiobiology research. Rev Sci Instrum 79: 125102.

4. Folkard M, Schettino G, Vojnovic B, Gilchrist S, Michette AG, et al. (2001) A focused ultrasoft x-ray microbeam for targeting cells individually with submicrometer accuracy. Radiat Res 156: 796-804.

5. Fowler TL, Fulkerson RK, Micka JA, Kimple RJ, Bednarz BP (2014) A novel high-throughput irradiator for in vitro radiation sensitivity bioassays. Phys Med Biol 59: 1459-1470.

6. Brady SL, Toncheva G, Dewhirst MW, Yoshizumi TT (2009) Characterization of a 137Cs irradiator from a new perspective with modern dosimetric tools. Health Phys 97: 195-205.

7. Brady SL, Yoshizumi TT, Anderson-Evans C, Nguyen G (2012) Isodose curve mappings measured while undergoing rotation for quality assurance testing of a 137Cs irradiator. Health Phys 102 Suppl 1: S8-12.

8. RSPSTF (2010) The 2010 Radiation Source Protection and Security Task Force Report. United States Nuclear Regulatory Commission.

9. Precision X-Ray I (2012) X-RAD x-ray irradiators.

10. Fung KK, Gilboy WB (2000) "Anode heel effect" on patient dose in lumbar spine radiography. Br J Radiol 73: 531-536.

11. Bushberg JT, Boone JM (2011) The Essential Physics of Medical Imaging. Philadelphia, PA: Lippincott Williams & Wilkins.

12. Rivard MJ, Davis SD, DeWerd LA, Rusch TW, Axelrod S (2006) Calculated and measured brachytherapy dosimetry parameters in water for the Xoft Axxent X-Ray Source: an electronic brachytherapy source. Med Phys 33: 4020-4032.

13. Fulkerson RK, Micka JA, Dewerd LA (2014) Dosimetric characterization and output verification for conical brachytherapy surface applicators. Part I. Electronic brachytherapy source. Med Phys 41: 022103.

14. Owen JB, Coia LR, Hanks GE (1992) Recent patterns of growth in radiation therapy facilities in the United States: a patterns of care study report. Int J Radiat Oncol Biol Phys 24: 983-986.

15. ICRU (1979) Quantitative Concepts and Dosimetry in Radiobiology. Washington, DC: Report.

16. Kroemer G, Galluzzi L, Vandenabeele P, Abrams J, Alnemri ES, et al. (2009) Classification of cell death: recommendations of the Nomenclature Committee on Cell Death 2009. Cell Death Differ 16: 3-11.

17. Roots R, Okada S (1972) Protection of DNA Molecules of Cultured Mammalian Cells from Radiation-induced Single-strand Scissions by Various Alcohols and SH Compounds. International Journal of Radiation Biology 21: 329-342.

18. Chapman JD, Doern SD, Reuvers AP, Gillespie CJ, Chatterjee A, et al. (1979) Radioprotection by DMSO of mammalian cells exposed to X-rays and to heavy charged-particle beams. Radiat Environ Biophys 16: 29-41.

19. Shinohara K, Nakano H, Ohara H (1996) Detection of Auger enhancement induced in HeLa cells labeled with iododeoxyuridine and irradiated with 150 kV x-rays--Effects of cysteamine and dimethylsulfoxide. Acta Oncol 35: 869-875.

20. Bekker-Jensen S, Mailand N (2010) Assembly and function of DNA double-strand break repair foci in mammalian cells. DNA Repair (Amst) 9: 1219-1228.

21. Rothkamm K, Horn S (2009) gamma-H2AX as protein biomarker for radiation exposure. Ann Ist Super Sanita 45: 265-271.

22. Kuo LJ, Yang LX (2008) Gamma-H2AX - a novel biomarker for DNA double-strand breaks. In Vivo 22: 305-309.

23. Sharma A, Singh K, Almasan A (2012) Histone H2AX phosphorylation: a marker for DNA damage. Methods Mol Biol 920: 613-626.

24. Scully R, Xie A (2013) Double strand break repair functions of histone H2AX. Mutat Res 750: 5-14.

25. Yang Z, Klionsky DJ (2010) Eaten alive: a history of macroautophagy. Nature Cell Biology 12: 814-822.

26. Hippert MM, O'Toole PS, Thorburn A (2006) Autophagy in cancer: good, bad, or both? Cancer Res 66: 9349-9351.

27. Degenhardt K, Mathew R, Beaudoin B, Bray K, Anderson D, et al. (2006) Autophagy promotes tumor cell survival and restricts necrosis, inflammation, and tumorigenesis. Cancer Cell 10: 51-64.

28. Mathew R, Kongara S, Beaudoin B, Karp CM, Bray K, et al. (2007) Autophagy suppresses tumor progression by limiting chromosomal instability. Genes Dev 21: 1367-1381.

29. Mathew R, Karp CM, Beaudoin B, Vuong N, Chen G, et al. (2009) Autophagy suppresses tumorigenesis through elimination of p62. Cell 137: 1062-1075.

30. Klionsky DJ (2012) Guidelines for the use and interpretation of assays for monitoring autophagy. Autophagy 8: 445-544.

31. Paglin S, Hollister T, Delohery T, Hackett N, McMahill M, et al. (2001) A novel response of cancer cells to radiation involves autophagy and formation of acidic vesicles. Cancer Res 61: 439-444.

32. Apel A, Herr I, Schwarz H, Rodemann HP, Mayer A (2008) Blocked autophagy sensitizes resistant carcinoma cells to radiation therapy. Cancer Res 68: 1485-1494.

33. Kim KW, Hwang M, Moretti L, Jaboin JJ, Cha YI, et al. (2008) Autophagy upregulation by inhibitors of caspase-3 and mTOR enhances radiotherapy in a mouse model of lung cancer. Autophagy 4: 659-668.

34. Zeng X, Kinsella TJ (2008) Mammalian target of rapamycin and S6 kinase 1 positively regulate 6-thioguanine-induced autophagy. Cancer Res 68: 2384-2390.

35. Tsuboi Y, Kurimoto M, Nagai S, Hayakawa Y, Kamiyama H, et al. (2009) Induction of autophagic cell death and radiosensitization by the pharmacological inhibition of nuclear factor-kappa B activation in human glioma cell lines. J Neurosurg 110: 594-604.

36. Munoz-Gamez JA, Rodriguez-Vargas JM, Quiles-Perez R, Aguilar-Quesada R, Martin-Oliva D, et al. (2009) PARP-1 is involved in autophagy induced by DNA damage. Autophagy 5: 61-74.

37. Huang Q, Wu YT, Tan HL, Ong CN, Shen HM (2009) A novel function of poly(ADP-ribose) polymerase-1 in modulation of autophagy and necrosis under oxidative stress. Cell Death Differ 16: 264-277.

38. Ferlay J, Shin HR, Bray F, Forman D, Mathers C, et al. (2010) Estimates of worldwide burden of cancer in 2008: GLOBOCAN 2008. Int J Cancer 127: 2893-2917.

39. Gillison ML, Koch WM, Capone RB, Spafford M, Westra WH, et al. (2000) Evidence for a causal association between human papillomavirus and a subset of head and neck cancers. J Natl Cancer Inst 92: 709-720.

40. Chaturvedi AK, Engels EA, Anderson WF, Gillison ML (2008) Incidence trends for human papillomavirus-related and -unrelated oral squamous cell carcinomas in the United States. J Clin Oncol 26: 612-619.

41. Ang KK, Harris J, Wheeler R, Weber R, Rosenthal DI, et al. (2010) Human papillomavirus and survival of patients with oropharyngeal cancer. N Engl J Med 363: 24-35.

42. Chaturvedi AK, Engels EA, Pfeiffer RM, Hernandez BY, Xiao W, et al. (2011) Human papillomavirus and rising oropharyngeal cancer incidence in the United States. J Clin Oncol 29: 4294-4301.

43. (2007) Human papillomaviruses. IARC Monogr Eval Carcinog Risks Hum 90: 1-636.

44. Schache AG, Liloglou T, Risk JM, Filia A, Jones TM, et al. (2011) Evaluation of human papilloma virus diagnostic testing in oropharyngeal squamous cell carcinoma: sensitivity, specificity, and prognostic discrimination. Clin Cancer Res 17: 6262-6271.

45. Scheffner M, Werness BA, Huibregtse JM, Levine AJ, Howley PM (1990) The E6 oncoprotein encoded by human papillomavirus types 16 and 18 promotes the degradation of p53. Cell 63: 1129-1136.

46. Munger K, Werness BA, Dyson N, Phelps WC, Harlow E, et al. (1989) Complex formation of human papillomavirus E7 proteins with the retinoblastoma tumor suppressor gene product. EMBO J 8: 4099-4105.

47. DiMaio D, Mattoon D (2001) Mechanisms of cell transformation by papillomavirus E5 proteins. Oncogene 20: 7866-7873.

48. Genther SM, Sterling S, Duensing S, Munger K, Sattler C, et al. (2003) Quantitative role of the human papillomavirus type 16 E5 gene during the productive stage of the viral life cycle. J Virol 77: 2832-2842.

49. Fakhry C, Westra WH, Li S, Cmelak A, Ridge JA, et al. (2008) Improved Survival of Patients With Human Papillomavirus-Positive Head and Neck Squamous Cell Carcinoma in a Prospective Clinical Trial. J Natl Cancer Inst 100: 261-269.

50. Shah NG, Trivedi TI, Tankshali RA, Goswami JV, Jetly DH, et al. (2009) Prognostic significance of molecular markers in oral squamous cell carcinoma: A multivariate analysis. Head & Neck 31: 1544-1556.

51. Reimers N, Kasper HU, Weissenborn SJ, Stützer H, Preuss SF, et al. (2007) Combined analysis of HPV-DNA, p16 and EGFR expression to predict prognosis in oropharyngeal cancer. Int J Cancer 120: 1731-1738.

52. Rischin D, Young RJ, Fisher R, Fox SB, Le QT, et al. (2010) Prognostic significance of p16INK4A and human papillomavirus in patients with oropharyngeal cancer treated on TROG 02.02 phase III trial. J Clin Oncol 28: 4142-4148.

53. Lindel K, Beer KT, Laissue J, Greiner RH, Aebersold DM (2001) Human papillomavirus positive squamous cell carcinoma of the oropharynx: a radiosensitive subgroup of head and neck carcinoma. Cancer 92: 805-813.

54. Mellin H, Dahlgren L, Munck-Wikland E, Lindholm J, Rabbani H, et al. (2002) Human papillomavirus type 16 is episomal and a high viral load may be correlated to better prognosis in tonsillar cancer. Int J Cancer 102: 152-158.

55. Weinberger PM, Yu Z, Haffty BG, Kowalski D, Harigopal M, et al. (2006) Molecular classification identifies a subset of human papillomavirus--associated oropharyngeal cancers with favorable prognosis. J Clin Oncol 24: 736-747.

56. Licitra L, Perrone F, Bossi P, Suardi S, Mariani L, et al. (2006) High-risk human papillomavirus affects prognosis in patients with surgically treated oropharyngeal squamous cell carcinoma. J Clin Oncol 24: 5630-5636.

57. Posner MR, Lorch JH, Goloubeva O, Tan M, Schumaker LM, et al. (2011) Survival and human papillomavirus in oropharynx cancer in TAX 324: a subset analysis from an international phase III trial. Ann Oncol 22: 1071-1077.

58. Blitzer GC, Smith MA, Harris SL, Kimple RJ (2014) Review of the clinical and biologic aspects of human papillomavirus-positive squamous cell carcinomas of the head and neck. Int J Radiat Oncol Biol Phys 88: 761-770.

59. Kimple RJ, Smith MA, Blitzer GC, Torres AD, Martin JA, et al. (2013) Enhanced radiation sensitivity in HPV-positive head and neck cancer. Cancer Res 73: 4791-4800.

60. Massillon-JL G, Chiu-Tsao S, Domingo-Munoz I, Chan M (2012) Energy Dependence of the New Gafchromic EBT3 Film:Dose Response Curves for 50 KV, 6 and 15 MV X-Ray Beams. International Journal of Medical Physics, Clinical Engineering and Radiation Oncology 1: 60-65.

61. McCaw TJ, Micka JA, Dewerd LA (2011) Characterizing the marker-dye correction for Gafchromic((R)) EBT2 film: a comparison of three analysis methods. Med Phys 38: 5771-5777.

62. Schindelin J, Arganda-Carreras I, Frise E, Kaynig V, Longair M, et al. (2012) Fiji: an open-source platform for biological-image analysis. Nat Methods 9: 676-682.

63. Thévenaz P, Ruttimann UE, Unser M (1998) A Pyramid Approach to Subpixel Registration Based on Intensity. IEEE Transactions on Image Processing 7: 27-41.

64. Kouloulias VE, Poortmans P, Antypas C, Kappas C, Sandilos P (2003) Field flatness and symmetry of photon beams: Review of the current recommendations. Technology & Health Care 11: 283-288.

65. Nath R, Biggs PJ, Bova FJ, Ling CC, Purdy JA, et al. (1994) AAPM code of practice for radiotherapy accelerators: report of AAPM Radiation Therapy Task Group No. 45. Med Phys 21: 1093-1121.

66. Dhar A, DeWerd LA, Stoebe TG (1973) Effects of annealing and cooling processes on thermoluminescence of LiF (TLD100). Health Phys 25: 427-433.

67. Srinivasan M, DeWerd LA (1976) Effect of deformation on the thermoluminescent properties of LiF and TLD 100 dosimeter crystals. Journal of Materials Science 11: 1849.

68. Horowitz Y, Olko P (2004) The effects of ionisation density on the thermoluminescence response (efficiency) of LiF:Mg,Ti and LiF:Mg,Cu,P. Radiat Prot Dosimetry 109: 331-348.

69. Nunn AA, Davis SD, Micka JA, DeWerd LA (2008) LiF:Mg,Ti TLD response as a function of photon energy for moderately filtered x-ray spectra in the range of 20-250 kVp relative to 60Co. Med Phys 35: 1859-1869.

70. Pike TL (2012) A dosimetric Characterization of an Electronic Brachytherapy Source in Terms of Absorbed Dose to Water. Madison, WI: University of Wisconsin.

71. Poudel S, Currier B, Medich DC (2015) Variation in the calibrated response of LiF, Al2O3, and silicon dosimeters when used for in-phantom measurements of source photons with energies between 30 KeV AND 300 KeV. Health Phys 108: 434-442.

72. Mora GM, Maio A, Rogers DW (1999) Monte Carlo simulation of a typical 60Co therapy source. Med Phys 26: 2494-2502.

73. Wan XS, Zhou Z, Kennedy AR (2003) Adaptation of the dichlorofluorescein assay for detection of radiation-induced oxidative stress in cultured cells. Radiat Res 160: 622-630.

74. Konca K, Lankoff A, Banasik A, Lisowska H, Kuszewski T, et al. (2003) A cross-platform public domain PC image-analysis program for the comet assay. Mutat Res 534: 15-20.

75. Olive PL, Banath JP, Durand RE (1990) Heterogeneity in radiation-induced DNA damage and repair in tumor and normal cells measured using the "comet" assay. Radiat Res 122: 86-94.

76. Fowler TL, Bailey AM, Bednarz BP, Kimple RJ (2014) High-throughput detection of DNA double-strand breaks using image cytometry. Biotechniques 58: 37-39.

77. Schuler N, Palm J, Kaiser M, Betten D, Furtwangler R, et al. (2014) DNA-damage foci to detect and characterize DNA repair alterations in children treated for pediatric malignancies. PLoS One 9: e91319.

78. Bristol ML, Di X, Beckman MJ, Wilson EN, Henderson SC, et al. (2012) Dual functions of autophagy in the response of breast tumor cells to radiation: cytoprotective autophagy with radiation alone and cytotoxic autophagy in radiosensitization by vitamin D 3. Autophagy 8: 739-753.

79. Yoshimori T, Yamamoto A, Moriyama Y, Futai M, Tashiro Y (1991) Bafilomycin A1, a specific inhibitor of vacuolar-type H(+)-ATPase, inhibits acidification and protein degradation in lysosomes of cultured cells. J Biol Chem 266: 17707-17712.

80. Moreau K, Ravikumar B, Renna M, Puri C, Rubinsztein DC (2011) Autophagosome precursor maturation requires homotypic fusion. Cell 146: 303-317.

81. Gunning PW, Ghoshdastider U, Whitaker S, Popp D, Robinson RC (2015) The evolution of compositionally and functionally distinct actin filaments. J Cell Sci.

82. Zhou C, Zhong W, Zhou J, Sheng F, Fang Z, et al. (2012) Monitoring autophagic flux by an improved tandem fluorescent-tagged LC3 (mTagRFP-mWasabi-LC3) reveals that high-dose rapamycin impairs autophagic flux in cancer cells. Autophagy 8: 1215-1226.

83. Schneider CA, Rasband WS, Eliceiri KW (2012) NIH Image to ImageJ: 25 years of image analysis. Nat Methods 9: 671-675.

84. Yao Q, Zheng R, Xie G, Liao G, Du S, et al. (2015) Late-responding normal tissue cells benefit from high-precision radiotherapy with prolonged fraction delivery times via enhanced autophagy. Sci Rep 5: 9119.

85. Lai E, Teodoro T, Volchuk A (2007) Endoplasmic reticulum stress: signaling the unfolded protein response. Physiology (Bethesda) 22: 193-201.

86. Kim I, Xu W, Reed JC (2008) Cell death and endoplasmic reticulum stress: disease relevance and therapeutic opportunities. Nat Rev Drug Discov 7: 1013-1030.

87. Kim KW, Moretti L, Mitchell LR, Jung DK, Lu B (2010) Endoplasmic reticulum stress mediates radiation-induced autophagy by perk-eIF2[alpha] in caspase-3/7-deficient cells. Oncogene 29: 3241-3251.

88. Kroemer G, Mariño G, Levine B (2010) Autophagy and the Integrated Stress Response. Molecular Cell 40: 280-293.

89. Deng J, Lu PD, Zhang Y, Scheuner D, Kaufman RJ, et al. (2004) Translational repression mediates activation of nuclear factor kappa B by phosphorylated translation initiation factor 2. Mol Cell Biol 24: 10161-10168.

90. Abedin MJ, Wang D, McDonnell MA, Lehmann U, Kelekar A (2006) Autophagy delays apoptotic death in breast cancer cells following DNA damage. Cell Death Differ 14: 500-510.

91. Kastan MB, Onyekwere O, Sidransky D, Vogelstein B, Craig RW (1991) Participation of p53 protein in the cellular response to DNA damage. Cancer research 51: 6304-6311.

92. Banin S, Moyal L, Shieh S-Y, Taya Y, Anderson C, et al. (1998) Enhanced phosphorylation of p53 by ATM in response to DNA damage. Science 281: 1674-1677.

93. Fritsche M, Haessler C, Brandner G (1993) Induction of nuclear accumulation of the tumor-suppressor protein p53 by DNA-damaging agents. Oncogene 8: 307-318.

94. Lakin ND, Jackson SP (1999) Regulation of p53 in response to DNA damage. Oncogene 18: 7644-7655.

95. Tasdemir E, Maiuri MC, Galluzzi L, Vitale I, Djavaheri-Mergny M, et al. (2008) Regulation of autophagy by cytoplasmic p53. Nature cell biology 10: 676-687.

96. Maiuri MC, Galluzzi L, Morselli E, Kepp O, Malik SA, et al. (2010) Autophagy regulation by p53. Current opinion in cell biology 22: 181-185.

97. Maiuri MC, Malik SA, Morselli E, Kepp O, Criollo A, et al. (2009) Stimulation of autophagy by the p53 target gene Sestrin2. Cell cycle 8: 1571-1576.

98. Lui VW, Hedberg ML, Li H, Vangara BS, Pendleton K, et al. (2013) Frequent mutation of the PI3K pathway in head and neck cancer defines predictive biomarkers. Cancer Discov 3: 761-769.

99. Keysar SB, Astling DP, Anderson RT, Vogler BW, Bowles DW, et al. (2013) A patient tumor transplant model of squamous cell cancer identifies PI3K inhibitors as candidate therapeutics in defined molecular bins. Mol Oncol 7: 776-790.